Nanotribological Properties of van der Waals Heterostructures

Dissertation

zur Erlangung des Grades
des Doktors der Naturwissenschaften
der Naturwissenschaftlich-Technischen Fakultäten
der Universität des Saarlandes

von

M.Sc. Eng. Bartosz Henryk Szczefanowicz

Saarbrücken
2023

Tag des Kolloquiums:	15. Dezember 2023
Dekan:	Prof. Dr. Ludger Santen
Berichterstatter:	Prof. Dr. Roland Bennewitz
	Prof. Dr. Uwe Hartmann
Akad. Mitglied:	Dr.-Ing. Andreas Tschöpe
Vorsitz:	Prof. Dr. Rolf Pelster

This dissertation is dedicated to my beloved parents
Danuta and Henryk Szczefanowicz

Abstract

The 2D materials exhibit excellent tribological properties due to their weak inter-plane interactions, such as the ultra-low friction, which can be further tuned by number of layers, application of electric bias, stacking of different materials into a van der Waals heterostructure, and change of substrate. In this work, the tribological properties of 2D materials were investigated experimentally by means of atomic force microscopy techniques in ultra-high vacuum and theoretically with atomistic simulations.

Friction measurements on epitaxial graphene on SiC(0001) show that the ultra-low friction is limited by a normal load threshold, above which friction increases by one order of magnitude. Simulations suggest that, at contact pressures above 10 GPa, the high-friction regime is a result of an intermittent sp^3 rehybridization of graphene and the formation of covalent bonds. Friction on the MoS_2/graphene heterostructure is dominated by adhesion due to the out-of-plane deformation of the MoS_2 layers. Increasing the number of MoS_2 layers decreases friction as the flexural compliance decreases. Higher friction was recorded on $MoSe_2$/hBN compared to graphene/hBN heterostructure or pristine hBN. Work on exfoliated materials was facilitated by the application of navigational microstructures.

Nanotribologische Eigenschaften von van-der-Waals-Heterostrukturen

Zusammenfassung

2D Materialien zeigen hervorragende tribologischen Eigenschaften, die mit der schwachen Wechselwirkung zwischen den Lagen erklärt werden können. Die extrem niedrige Reibung kann zusätzlich eingestellt werden durch die Anzahl der Lagen, Anlegen einer elektrischen Spannung, das Stapeln verschiedener 2D Materialien in eine Heterostruktur, oder die Wahl des Substrats. In dieser Arbeit wurden die tribologischen Eigenschaften von 2D Materialien experimentell mit Hilfe der Rasterkraftmikroskopie im Ultrahochvakuum untersucht. Die Ergebnisse werden mit atomistischen Simulationen verglichen.

Reibungsmessungen auf epitaktischem Graphen auf SiC(0001) zeigen, dass die extrem niedrige Reibung durch einen Grenzwert in der Auflagekraft begrenzt ist, oberhalb dessen die Reibung um eine Größenordnung ansteigt. Simulationen legen nahe, dass oberhalb eines Kontaktdrucks von 10˜GPa das Auftreten höherer Reibung auf eine zwischenzeitliche sp^3 Rehybridisierung und die Bildung kovalenter Bindungen zurückgeführt werden kann. Reibung auf der MoS_2/Graphen-Heterostruktur wird von Adhäsion bestimmt, die durch eine Verformung der MoS_2-Lagen in Richtung der AFM-Spitze verstärkt wird. Eine Erhöhung der Zahl an MoS_2-Lagen verringert die Reibung da die Verbiegungssteifigkeit steigt. $MoSe_2$/hBN zeigt höhere Reibung als Graphen/hBN Heterostrukturen oder hBN. Die Untersuchung der exfolierten 2D-Materialien im Ultrahochvakuum wird erst möglich durch die Anwendung von Mikrostrukturen zur Positionsbestimmung.

Contributions of co-authors of publications

This dissertation was realized in the Interactive Surfaces group of Professor Roland Bennewitz at the INM - Leibniz Institute for New Materials. However, this dissertation would not have been possible without collaboration with:

- the Tribology Business Unit of Professor Michael Moseler at Fraunhofer Institute for Mechanics of Materials IWM,
- Applied Physical Chemistry & Molecular Nanotechnology group of Professor Andrey Turchanin at Friedrich Schiller University Jena,
- 2^{nd} Institute of Physics A lead by Professor Christoph Stampfer,
- Professor Tobin Filleter from Department of Mechanical & Industrial Engineering at the University of Toronto,
- Dr. Joao Marcelo J. Lopes from Paul-Drude-Institut für Festkörperelektronik.

The author of this work acknowledges the help of other colleagues from the INM - Leibniz Institute for New Materials.

The author of this work acknowledges financial support by Deutsche Forschungsgemeinschaft within the Priority Program SPP 2244 "2DMP".

Material of published work in this thesis

Chapter 4 contains unpublished data and material already published in article [1] :
B. Szczefanowicz, T. Kuwahara, T. Filleter, A. Klemenz , L. Mayrhofer, R. Bennewitz and M. Moseler, Formation of intermittent covalent bonds at high contact pressure limits superlow friction on epitaxial graphene, *Physical Review Research*, 5, 2023, L012049,
DOI: 10.1103/PhysRevResearch.5.L012049. (under the terms of the Creative Commons Attribution 4.0 International License)
Author contributions:
The author of this work and Takuya Kuwahara contributed equally to this publication. Roland Bennewitz and Michael Moseler conceived the original idea and the experiments. The sample was prepared by the research group of Prof. Thomas Seyller. **The author of this work** and Tobin Filleter performed AFM and FFM experiments. All experimental data presented in the main text of the publication was measured by **the author of this work** with additional results measured by Tobin Filleter presented in the supplementary information. The experimental data presented in chapter 4 consists of all data from the publication and unpublished results of **the author of this work**. Takuya Kuwahara, Andreas Klemenz, Leonhard Mayrhofer conducted DFT and DFTB simulations. TEM images were recorded by Marcus Koch. Roland Bennewitz, Michael Moseler, Takuya Kuwahara, and Leonhard Mayrhofer and **the author of this work** wrote the manuscript.

Chapter 5 contains unpublished data and material already published in article [2] :
Z. Liu, **B. Szczefanowicz**, J. M. J. Lopes, Z. Gan, A. George, A. Turchanin and R. Bennewitz, Nanoscale friction on MoS_2/graphene heterostructures, *Nanoscale*, 15, 2023, 5809–5815, DOI: 10.1039/d3nr00138e. (under the terms of the Creative Commons Attribution-Non Commercial 3.0 Unported License)
Author contributions:
The author of this work, Zhao Liu and Roland Bennewitz conceived the original idea and the experiments. Joao Marcelo J. Lopes, Antony George, Ziyang Gan and Andrey Turchanin prepared the MoS_2/graphene/SiC(0001) heterostructure samples. Zhao Liu and **the author of this work** performed the AFM and FFM experiments and analyzed the obtained data. TEM images were recorded by Marcus Koch. Zhao Liu, Roland Bennewitz, and **the author of this work** wrote the manuscript. **All authors** discussed the results and revised the manuscript.

In preparation

Chapter 6 presents unpublished data of a collaborative study:
B. Szczefanowicz, A. Rothstein, B. Nothdurft, C. Stampfer, R. Bennewitz, Tribological properties of graphene/hBN and $MoSe_2$/hBN van der Waals heterostructures.
Author contributions:
The author of this work designed a project of navigational microstructure. Birgit Nothdurft and **author of this work** fabricated navigational microstructures on silicon substrates by means of Focused Ion Beam. Alexander Rothstein prepared van der Waals heterostructures of graphene/hBN/SiO_2 and $MoSe_2$/hBN/SiO_2. **The author of this work** performed the AFM and FFM experiments and analyzed the obtained data. Roland Bennewitz and Christof Stampfer were directing the research.

Contents

List of Figures

List of Tables

Abbreviations and symbols

Abbreviations

AFM	–	atomic force microscopy
BS	–	bias spectroscopy
cAFM	–	conductive atomic force microscopy
C	–	carbon
CPD	–	contact potential difference
CVD	–	chemical vapor deposition
Cu	–	copper
DFT	–	density functional theory
DFTB	–	self-consistent charge-density functional tight-binding molecular dynamics
DMT	–	Derjaguin-Muller-Toporov contact mechanics model
FFM	–	friction force microscopy
FS	–	force spectroscopy
FIB	–	focused ion beam
Ga	–	gallium
hBN	–	hexagonal boron nitride
cBN	–	cubic boron nitride
KPFM	–	Kelvin probe force microscopy
LFM	–	lateral force microscopy
MD	–	molecular dynamics
MEMS	–	microelectromechanical systems
MoO_3	–	molybdenum oxide
MoS_2	–	molybdenum disulphide
$MoSe_2$	–	molybdenum diselenide
MSCU	–	micro slide control unit
$NbSe_2$	–	niobium diselenide
ncAFM	–	dynamic force microscopy
NEMS	–	nanoelectromechanical Systems
Ni	–	nickel
Pt	–	platinum
PtIr	–	platinum–iridium alloy
PES	–	potential energy surface
S	–	sulfur
SEM	–	scanning electron microscope
SPM	–	scanning probe microscope
STM	–	scanning tunneling microscope
SiC	–	silicon carbide
SiO_2	–	silicon dioxide
SiO_x	–	silicon oxide
TEM	–	transmission electron microscope
TMDC	–	transition metal dichalcogenide

TiIr – titanium–iridium alloy
UHV – ultra high vacuum
VT-AFM – varied temperature atomic force microscope
WS_2 – tungsten disulphide
WSe_2 – tungsten diselenide

Symbols

a – contact radius
A – contact area
A_r – real contact area
E – Young modulus
E_{6H-SiC} – silicon carbide Young modulus
E_{eff} – effective elastic modulus of the combined system of tip and sample
E_{Si} – silicon Young modulus
E_{SiO_2} – silicon oxide Young modulus
f_0 – natural frequency
f_I – resonant frequency
F_{atr} – attractive force
F_L – friction force
F_N – normal force / normal load
$gain$ – amplification applied to the lateral signal
G – shear modulus
h – magnitude of the position vector
h_{tip} – tip height
k – spring constant
k_N – normal stiffness
k_T – torsional stiffness
l – length of the cantilever
m – mass
M – molar mass
N_A – Avogadro's number
p – pressure
p_0 – threshold contact pressure
p_m – yield pressure of the asperity
P_Z – normal pressure
r – tip radius
R – gas constant
RMS – surface roughness
S_L – lateral sensitivity of the detector
S_N – normal sensitivity of the detector
t – thickness of the cantilever
t_{KPFM} – period

T – temperature
U_0 – periodic potential
U_{AC} – alternate current voltage
U_{bias} – applied voltage bias
U_{CPD} – compensation voltage bias
U_{DC} – direct current voltage
U_L – friction force signal
U_{Lfwd} – forward lateral signal
U_{Lbwd} – backward lateral signal
U_N – normal load signal
$U_{N\infty}$ – the offset signal from 0 N normal load
U_V – vertical deflection signal
v – sliding velocity
w – mean width of the cantilever
Y – elastic limit
z – distance in Z axis
Z_w – flux of residual gas molecules striking the surface
α – coefficient of the normalized frequency shift
γ – adhesion energy
Δf – normalized frequency shift
μ – friction coefficient
μ_{DMT} – DMT friction coefficient
ν – Poisson's ratio
ν_{6H-SiC} – silicon carbide Poisson's ratio
ν_{Si} – silicon Poisson's ratio
ν_{SiO_2} – silicon oxide Poisson's ratio
ρ – mass density
ρ_{Si} – silicon mass density
σ – simulated shear stress
τ – shear stress
ω – modulation frequency

1 Introduction

1.1 Motivation

Resistance in the sliding movement of two surfaces pressing against each other is described as the friction force. Friction is caused by multiple mechanisms and is a multiscale phenomenon from atomic friction in the nanoscale to earthquakes in the macroscale. The friction force and wear are estimated to contribute annually 23% of global energy consumption, which generates the cost of 2 500 000 million € and the total CO_2 emissions of 8,120 million tons [3]. Reduction of losses related to friction and wear will not only decrease global economical costs but also reduce human impact on climate change, which is becoming a more and more urgent problem at the time of this work. Therefore, it is imperative to further deepen the understanding of mechanisms governing friction in all scales. A branch of science and engineering, which covers problems related to friction, wear and lubrication is called tribology (gr. tribos - "to rub", gr. logos - "to study") [4].

The friction force is decreased by proper lubrication of contacting surfaces. In the macroscale, mineral-based oils are usually employed for hydrodynamic lubrication. However, at the micrometer or nanometer scale, mineral oil liquid lubricants exhibit increased effective viscosity and often layering or solidification [5, 6, 7], which decrease the probability of penetration of nanometer contacts. The nanocontacts can have comparable size to molecules of mineral oils, which may cause additional resistance instead of lubrication [8]. Therefore, conformal coating by solid lubricants is more preferable option of lubrication in micro- and nanoscale. A special group of such lubricants are 2D materials, which due to their thickness exhibit exotic and extreme mechanical, electronic and magnetic properties [9, 10]. Tools are getting smaller, and their production is complicated, time-consuming and expensive. The applicability of micro- and nanoelectromechanical systems (MEMS, NEMS) demands their long-lasting to make them affordable[11]. Properly designed coatings made of 2D materials can increase the lifetime and reliability of nanodevices by reducing friction and wear [12, 13]. To design the most optimal 2D materials-based coatings, it is vital to understand the physical and chemical principles behind such lubrication. Fundamental studies of tribological properties of 2D materials and the phenomena behind them are the motivation of this work.

1.2 The history of tribology from macro- to nanoscale

1.2.1 The early tribological applications and investigations

The friction phenomenon is one of the earliest physical phenomena that were applied by humanity [14]. The first prehistoric example would be the ignition of fire by frictional heat and the development of the first tools, including the wheel. Humanity realized that dry friction can be modified by lubrication. The earliest records of lubrication can be found in ancient times. In ancient Egypt, the transport of large blocks or entire statues was based on sliding them on wooden sledges on sand by workers. To decrease the friction between the wood and the sand, workers poured water on the sand [15]. A similar method was applied in ancient Assyria to transport statues [16]. In 15th-16th century China, huge stones were moved on wooden sledges on water-lubricated ice for the construction of the Forbidden City [17].

It is not exactly known how people from the distant past understood the phenomenon of friction, as the number of surviving documents until this day is limited and some may still be discovered in future. The earliest documented and today known experimental approach to describe friction force was done by Leonardo da Vinci [18, 19, 20]. In his experiment on dry friction, Leonardo da Vinci recorded the area independence of friction force and proportionality of friction force to normal load. Though, these findings were not published at that time and remained unknown to the public for a long time. The first laws of friction were formulated and published two centuries later by Guillaume Amontons [21, 22]. Amontons in his experiments reached the same conclusions as Leonardo da Vinci. Leonhard Euler investigated theoretically the sliding motion of a block on a slope. Based on his study, Euler concluded that it is necessary to distinguish static and kinetic friction and stated that the former is always larger than the latter [14, 23]. According to the documented knowledge, Euler is considered the first person who made the distinction between static and kinetic friction [14]. Another important discoveries of the friction phenomenon were made by Charles-Augustin de Coulomb. Coulomb experimented on dry friction between different materials, the influence of a rest time on static friction and sliding velocity on kinetic friction. He concluded that the static friction increases with rest time and that the kinetic friction is independent of the sliding velocity [24, 25]. This last observation is considered the third law of friction in the macroscale, next to the two laws formulated by da Vinci and Amontons. All three laws of macroscopic dry friction are summarized below:

1. **The first da Vinci-Amontons law** – The force of friction is independent of the apparent area of contact.

2. **The second da Vinci-Amontons law** – The force of friction F_L is directly proportional to the applied normal load F_N according to equation 1.1:

$$F_L = \mu \cdot F_N \tag{1.1}$$

   where μ is the coefficient of friction, which is larger for static friction than kinetic friction.

3. **Coulomb's law of friction** – Kinetic friction is independent of the sliding velocity.

Coulomb was also a proponent of the interpretation that the origin of friction is the microscopic roughness. This however was against experimental observations, where highly polished surfaces exhibit not low, but high friction. John Theophilus Desaguliers explained the increase in friction on highly polished surfaces as a result of adhesion force [22, 26]. This interpretation was in conflict with the first law of da Vinci-Amontons law, because the adhesion is directly proportional to contact area, whereas the friction is independent of the apparent area of contact.

1.2.2 Adhesion theory of friction

This conflict was solved by Frank Philip Bowden and David Tabor. In their work, they explained that the usual surfaces have nonzero roughness and the apparent contact area between two interfaces is supported on numerous micro- and nanoasperities, which press on each other and form a much smaller real contact area A_r [27]. A_r is a sum of areas of all junctions

formed between asperities of both surfaces. In their model, the friction force F_L needed to break all junctions is proportional to the real area of contact A_r according to the equation:

$$F_L = \tau \cdot A_r \tag{1.2}$$

where τ is the shear stress, which is the intrinsic property of the junction. In the past, it was assumed that these asperities deform elastically. However, normal load F_N cause high mean yield pressure of the asperities p_m and leads to plastic deformation until the final real contact area is formed according to equation 1.3:

$$A_r = \frac{F_N}{p_m} \tag{1.3}$$

The deformation depends on normal load and may occur until condition $p_m = 3Y$ is reached, where Y is an elastic limit of the softer material. After combining the equations 1.2 and 1.3, the expression 1.4 is formed:

$$F_L = \tau \frac{F_N}{p_m} \tag{1.4}$$

Because the real contact area depends on the normal load, the friction force also depends on normal load and the coefficient of friction can be described as $\mu = \frac{\tau}{p_m}$. The Bowden and Tabor theory explains that, while friction force is independent of apparent contact area, it is proportional to real contact area.

1.2.3 The friction force in nanoscale

The development of science and technology leads to miniaturization of devices to micro and nanoscale. The miniaturization gave inception of the nanoscience and nanotechnology. It became important to investigate surfaces in more detail at an even smaller scale. Crucial was the invention of atomic force microscopy [AFM] by Binnig, Quate and Gerber in 1986 [28], which marked the beginning of nanotribology. It was soon discovered that the friction phenomenon differs in micro- and nanoscale in comparison to macroscale and the nanoscience opens access to discover new phenomena.

Because of the small scale, the experiments in the nanoscale are challenging, but their results allow analytical approaches to be explained. In theoretical nanotribology, the Prandtl-Tomlinson model is one of the most popular models. It was suggested by Ludwig Prandtl in 1928 to describe plastic deformations in crystals [29, 30]. This simple model considers the one-dimensional movement of a point mass m being dragged in a periodic potential U_0 by means of a spring k with a constant velocity v and damped proportionally to velocity (figure 1.1a)). Prandtl published this model in his native German language. This resulted in limited accessibility to the publication for a long time for the largest part of the international tribological community, which instead was wrongly referring to it as the "Tomlinson model", based on the work of George Arthur Tomlinson on an adhesive contribution to friction [30, 31]. For these historical reasons, this model is now being referred to as the Prandtl-Tomlinson model. Although, the Prandtl-Tomlinson model was designed for plastic deformations in crystals, its simplicity and generality allow it to describe many fundamental properties of dry friction. The Prandtl-Tomlinson model

distinguishes static and kinetic friction and predicts important nanotribological phenomena, such as an atomic stick-slip and a structural superlubricity. In this model, Prandtl was the first to conclude that thermal fluctuations should lead to a logarithmic dependency of the frictional force on velocity [29, 30]. Thanks to its simplicity, the Prandtl-Tomlinson model was later modified into multiple different models to describe various aspects of dry friction in the nanoscale.

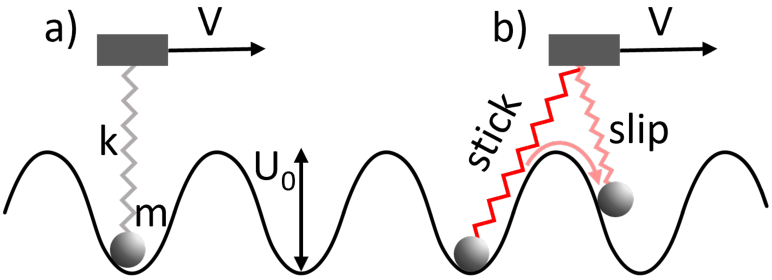

Figure 1.1: The Prandtl-Tomlinson model: a) a point mass m dragged in a sinusoidal periodic potential U_0 by means of a spring k with a constant velocity v; b) a stick and slip motion (figure based on [32])

Depending on the elastic properties of the sliding body, the motion can be continuous or intermittent. The motion of a sufficiently elastic body is characterized by elastic instabilities, where the sliding body alternates between sticking to one position and slipping to another [33]. Such motion is called stick-slip. In the macroscale, the stick-slip motion can be a result of many factors and be either periodic or chaotic. The Prandtl-Tomlinson model also predicts that motion over a corrugated surface potential for sufficiently soft springs exhibits elastic instabilities [29, 30] (figure 1.1b)). This prediction perfectly matches the description of an atomic stick-slip motion, which originates from atomic movement over the periodic potential of the surface lattice. The atomic stick-slip was first observed experimentally by Mate *et al.* [34] in 1987 on a graphite surface by using the AFM. The strongest effect of the atomic stick-slip occurs for the motion of coupled atoms with the lattice commensurate to the periodicity of the surface potential.

The opposite effect occurs when the lattice of coupled atoms is incommensurate with the periodicity of the surface potential. In such an incommensurate situation, the position of each atom within the surface potential is shifted in phase. Because of that, mutual atomic forces cancel each other on average and result in near frictionless motion [30]. This effect is called structural superlubricity. The required incommensurability can be achieved between two crystalline surfaces with mismatching lattices or by rotation of two crystalline lattices with respect to each other. The structural superlubricity was first described by Motohisa Hirano and Kazumasa Shinjo [35, 36], who later demonstrated it experimentally for a clean crystalline W(110) tip sliding in the ultrahigh vacuum on a Si(100) surface [37]. Angular anisotropy of superlubricity was later proved by Dienwiebel *et al.* [38] between graphite and graphene surfaces.

1.2.4 Development of 2D materials

The work of Novoselov *et al.* [39] on the electrical properties of graphene was revolutionary for nanotechnology. Novoselov demonstrated how to easily obtain graphene, the first 2D material,

and also attracted the attention of the scientific community to its exotic properties. It opened the new field of studies on 2D materials. Soon after, various other scientists reported on the novel physical properties of graphene. Later, other 2D materials: hexagonal boron nitride [hBN] and transition metal dichalcogenide monolayers such as molybdenum disulphide [MoS_2], were fabricated and tested. For their work on graphene, Konstantin Novoselov and Andre Geim were awarded The Nobel Prize in Physics in 2010 [40].

The research did not stop on single layers. Already accessible 2D materials started to be combined into van der Waals heterostructures. This new dimension and a growing number of types of 2D materials opened access to a virtually infinite number of combinations and their unique physical properties [41]. Although 2D materials and their heterostructures are being mainly researched in the context of their electric, magnetic or optical properties [42], they have also remarkable mechanical properties. Weak interlayer van der Waals interactions and strong intralayer bonds of 2D materials lead to ultra-low friction and make them excellent materials for tribological applications from nano- to macroscale [43].

1.3 Scope of Thesis

The thesis consists of seven chapters, including the introduction, and covers three projects focusing on various aspects of the nanotribological properties of 2D materials and their van der Waals heterostructures. The aim of this work is to investigate the influence of contact pressure, bias voltage, number of molecular layers, roughness, and composition of the heterostructures on friction force at the atomic scale. This work is based on the AFM experiments in ultra-high vacuum [UHV] and by simulations corresponding to the experimental settings .

Chapter 2 introduces the current state of knowledge about tribological properties of 2D materials and their van der Waals heterostructures. Here, the choice of materials selected in this dissertation is explained.

Chapter 3 contains descriptions of the materials investigated in this thesis and methods of their fabrication including preparation of a navigational microstructure. Experimental and theoretical methods employed in this thesis are described here.

Chapter 4 unravels a limitation of ultra-low nanoscale friction on epitaxial graphene on SiC(0001) at high contact pressure. Both experimental and simulation results demonstrated a significant increase in friction force above critical contact pressure. Furthermore, a contact pressure modulation of conductivity was observed experimentally. Similar AFM results of friction force were observed for both SiO_x and diamond probes. The rehybridization of graphene from sp^2 to sp^3 and the formation of covalent bonds between the graphene and the probe are discussed in this chapter as the causes of these observations.

Chapter 5 elucidates the influence of the number of layers and bias voltage on friction force on the van der Waals heterostructure of MoS_2 on graphene on SiC(0001). Experimental results showing a decrease in friction with the increasing number of layers of MoS_2 were analyzed by fitting the Derjaguin-Muller-Toporov [DMT] contact mechanics model. Manipulations of MoS_2 flakes in a superlubric regime on graphene were demonstrated. The contribution of adhesion, shear stress, bending rigidity of 2D materials and bias voltage in friction force on 2D materials are discussed in this chapter.

Chapter 6 explores frictional properties of van der Waals heterostructures of $MoSe_2$ on hBN and graphene on hBN. Localization and identification of the heterostructures on the SiO_x substrate were facilitated by a navigational microstructure and AFM techniques. Similar tribological properties were observed for graphene/hBN heterostructure and hBN beneath, whereas higher friction was recorded on $MoSe_2$ on hBN than on its hBN base. Substrate selection, surface roughness, preparation method, comparison with the results obtained in Chapters 4 and 5 in relation to the observations made in this chapter, as well as the effects of the application of the navigational microstructure are discussed in this chapter.

Chapter 7 provides the final summary and conclusions of this dissertation.

2 State of field

Atomically thin 2D materials exhibit excellent mechanical properties, next to exotic electric, magnetic and optical properties [42]. The latter are utilized in electronic and optoelectronic devices, while the former are used in tribological applications, which is the topic of this dissertation. On one side, strong intralayer bonds of 2D materials make them stiff and durable. For example, the elastic modulus measured on graphene corresponds to Young's modulus of $\approx$1 TPa [44]. On another side, weak interlayer van der Waals interactions of 2D materials decrease surface interactions and lead to ultra-low friction. Numerous studies were motivated by the tribological properties of 2D materials and their application as coatings. This chapter contains a short review of current knowledge on tribological aspects of 2D materials and their van der Waals heterostructures that are most relevant to this dissertation.

2.1 Tribological properties of 2D materials

Structural superlubricity

The most important tribological aspect of 2D materials is superlubricity. Friction in micro- and macroscale contacts can be reduced by structural superlubricity, realized among other means by the application of 2D materials [45]. Superlubricity and its angular anisotropy on graphite were demonstrated in the pioneering experiments at nanoscale layered material contacts by Dienwiebel *et al.* [38]. They recorded ultra-low friction when the lattices of the graphite and a graphene flake at the scanning tip were not oriented in the same direction. The friction was higher every 60°, which corresponds to the symmetry of the hexagonal graphitic lattice.

Liu *et al.* [46] have reported microscale superlubricity between incommensurate surfaces of graphite mesas and their spontaneous self-retraction to minimize interface energy. The self-retraction exhibits a sixfold symmetry and was observed in ambient and vacuum conditions. In similar experiments and simulations, the microscale structural superlubricity was confirmed between graphite–hBN heterojunction by Song *et al.* [47]. The orientational anisotropy of the sliding friction was found to be orders of magnitude smaller than that of the corresponding homogeneous graphitic contact. Frictional anisotropy in the heterojunction is dominated by an internal degree of freedom of the contacting layers, which is caused by the incommensurability of surfaces and the formation of a moiré pattern in the contact. It is in contrast to the mechanism in homogeneous graphitic junctions, where frictional anisotropy is dominated by dissipation through the center of mass motion.

Another approach to obtain macroscale superlubricity was presented by Berman *et al.* [48]. They showed experimentally and theoretically the formation of graphene nanoscrolls wrapped over diamond nanoparticles. It resulted in the incommensurate state and decreased contact area, which in turn reduced the coefficient of friction to 0.004. However, such a phenomenon occurred only in dry conditions, because humid conditions prevent initially adsorbed graphene from detachment from the SiO_2 substrate.

The range of investigated in this work 2D materials includes TMDC materials, in which case the superlubricity was proved experimentally on MoS_2 in UHV by Martin *et al.* [49]. This dissertation addresses the problem of limits of ultra-low friction with increasing normal load

on 2D materials and their van der Waals heterostructures.

Chemical modifications

Promising tribological properties of graphene and other 2D materials encouraged further study of their chemical properties and chemical modifications to have better control and further enhance their tribological properties. Graphene oxide found its application as an additive to mineral oils. Mungse *et al.* proposed a method how to improve the lubricity of graphene-oxide-containing oil [50]. Graphene oxide modified with stearic/oleic acid improves solubility and dispersion stability, which enhance the tribological efficiency of engine oil. Fluorination causes an increase in hydrophobicity and a decrease in adhesion and friction, for example of self-assembly monolayers [51]. However, in the case of graphene, the fluorination increases friction due to an increased surface potential corrugation [52].

Some chemical modifications are metastable and require maintenance of certain conditions. AFM experiments and ab initio simulations of Barboza *et al.* [53] show that bilayer graphene in the vicinity of water molecules can undergoes diamentization under high contact pressure. As long as the contact pressure is maintained, graphene changes its hybridization from sp^2 to sp^3 and adsorbs hydroxyl functional groups. The formed material is called diamondol and is a ferromagnetic insulator. A similar study was performed on hBN and corresponding results were observed. Compression of hBN in the vicinity of water molecules causes a change in hybridization to sp^3, adsorption of hydroxyl groups and increase in electric conductivity [54]. The formed material is called bonitrol. Depending on the stacking of hBN, bonitrol can form already at around 6.7 GPa for AB stacking and from 8.2 GPa for AA stacking. Further increase in contact pressure leads to rehybridization of deeper layers of hBN. Both diamondol and bonitrol require humidity and high contact pressure to form.

In this work, investigated surfaces were not chemically modified to avoid the increase in friction. The pressure induced rehybridization, the formation of covalent bonds between layers of 2D materials and their influence on friction are important aspects of this dissertation.

The influence of bias voltage on friction

The exotic electric properties of 2D materials are being thoroughly explored. Some of the future nanodevices will be working under changing bias voltage, which in turn will affect their tribological properties. Simulations of Wolloch *et al.* demonstrate a relation between electric and tribological properties [55]. The charges on contacting interfaces undergo charge redistribution, which in turn affects adhesion energy, potential energy surface and finally friction. The application of proper coatings, such as graphene, leads to passivation of the surface and different charge redistribution, which determine friction. Song *et al.* went one step further and, based on their experiments on graphene on Ru(0001) and simulations, proposed an electronic property fluctuations model to describe the effect of electron redistribution and transfer on the sliding barrier under the bias voltage or current [56].

Increases of friction with bias voltage different from 0 V were recorded by Peng *et al.* [57]. Based on their friction experiments with a TiIr tip on $MoSe_2$ flakes on SiO_2, they concluded that the increase in friction is caused by an enhanced electrostatic contribution to adhesion

force. Similar studies were performed with PtIr tips on surfaces of graphene/Au and hBN/SiO_2 [58, 59]. Both conclude enhancement of the potential energy surface and increase in electrostatic adhesion. Under a bias voltage, the graphene may undergo oxidation in a humid environment.

Single layers of MoS_2 are polarized. The polarization is compensated when an additional layer is added. Lavini *et al.* observed that MoS_2 crystals with an odd number of layers are effectively polarized, which increases friction on the crystal surface [60]. For unpolarized MoS_2 crystals with an even number of layers, the friction is lower. The increase in friction is more apparent in the case of polycrystalline structure due to adsorbates on surface defects.

Understanding the influence of the bias voltage is important to help modulate friction and is even necessary for surfaces, which are designed to be permanently under certain voltage. One part of this dissertation is focused on the relation between the bias voltage and friction.

Number of layer dependence of friction

Depending on the method of preparation or on the designed application, 2D materials can have more than one layer, which results in different frictional properties. Based on AFM experiments and simulations, Lee *et al.* [61, 62] described the dependence of friction on the number of layers of 2D materials. They observed that friction force decreases with increasing number of layers of 2D material. The same finding was recorded on four different 2D materials: graphene, hBN, MoS_2 and $NbSe_2$. Scan lines on thinner 2D materials exhibit so-called "strengthening", where friction first increases and then stabilizes around a certain value. This "strengthening" effect decreases with increasing number of layers. Depending on other scan parameters, the "strengthening" may not reach stability until the end of the scan line. The phenomenon was explained by out-of-plane deformations of 2D material, which are caused by stronger interactions of 2D material with the AFM tip than the substrate below. Deformations lead to larger real contact area, increase in adhesion force and ultimately in friction. Increasing the number of layers improves the bending rigidity of 2D material, which in turn decreases out-of-plane deformations. The phenomenon is known as a "puckering effect".

Further evidence supporting this interpretation was presented by molecular dynamics simulations of Li *et al.* [63]. They suggested that the strengthening effect is caused by increasing commensurability of 2D material during sliding, which results in the increase of real contact area. Huang *et al.* [64] explored the friction on supported and suspended MoS_2 layers. The puckering was observed in both cases, and it was stronger on suspended than supported MoS_2 layers. MoS_2 layers which have interactions with the supporting SiO_2 substrate, are less susceptible to out-of-plane deformations. The friction increases with the increasing size of the hole, over which the MoS_2 layers are suspended. The shape of the hole does not have an influence on measured friction.

However, opposite observations, where the friction increases with the number of layers of 2D material, were reported by Ye *et al.* [65]. They measure friction between the golden tip and graphene on the SiO_2 substrate. They explained their findings as an influence of substrate roughness on layer-dependent friction.

The contradiction in observations was resolved by D. Andersson and A. S. de Wijn [66]. They introduced a theoretical model based on the Prandl-Tomlinson model explaining the

frictional strengthening and layer number dependence of friction. The model considers the influence of local deformation, tip-surface sheet interactions and tip-substrate interactions. They demonstrated that the addition of the extra degree of freedom can describe any deformation, whether it is in-plane or out-of-plane, as well as the quality of the contact. They explained that previous experiments and simulations observed different cases, where different mechanisms of friction dominate.

In this dissertation, the influence of the number of layers on friction is considered for van der Waals heterostructures of MoS_2 on graphene.

Substrate dependence of friction

Tribological properties of 2D materials depend on the substrates they are coating, and in the case of transfer methods of preparation also on the substrates they were grown on. The performance of transferred graphene, grown via the chemical vapor deposition method [CVD], as a solid lubricant depends on the growth substrate [67]. Graphene exhibits lower friction on a SiO_2 substrate if it was grown and transferred from Ni than Cu. Kim *et al.* explained that carbon grown on Ni did not fully form graphene and remained amorphous [67]. Because of adhesion, both graphene and amorphous layers are transferred to the SiO_2 substrate. In the case of Cu-grown graphene, the amorphous carbon layer is not formed. During friction experiments, the graphene is worn off and adsorbs on the probe, but Ni-grown amorphous carbon remains on the SiO_2 substrate. This results in low friction between amorphous carbon on the SiO_2 and graphene adsorbed on the tip.

Klemenz *et al.* [68] studied the friction and wear of graphene on Pt(111). Their molecular statics simulations of sliding and AFM experiments demonstrated that three phases can be distinguished depending on normal load during indentation or sliding. At low normal load, only elastic deformations occur and the friction force remains low with a possible stick-slip movement and observation of the moiré superlattice of graphene on Pt(111). At a higher normal load, Pt is plastically deformed and the friction force increases. The graphene increases the bearing properties of Pt(111) until the critical normal load when the internal strain ruptures the graphene layer. At this point, the surface is being indented and in case of sliding movement, the plowing starts, and the friction force and deformations increase drastically up to the rate typical for the bare Pt surface. Graphene coating smooths the Pt(111) surface in a so-called "carpet effect" [69], which mitigates the effects of the tip roughness.

At lower normal loads the friction force is modulated by moiré superlattice formed due to a mismatch between graphene and Pt(111) lattices [70]. At a certain normal load threshold, the friction increases due to the transition from a superlubric to a dissipative regime. The graphene layer undergoes in-plane deformation to maintain commensurability beneath the tip, which leads to stretching of the moiré pattern until release in major slip. The normal load threshold is related to the size of the moiré tile, which depends on the orientation of the graphene lattice with respect to the Pt(111) lattice. It might be related to the amount of strain that can be accumulated in the moiré tile of each size.

SiC found an application as a low-friction antiwear coating for MEMS [71]. The growth of

epitaxial graphene on 6H-SiC(0001) is further improving its tribological properties. Thermal decomposition of 6H-SiC(0001) allows the fabrication of large areas of graphene monolayers [72], which completely cover the entire surface. Ab initio study conducted by Mattausch and Pankratov [73] have shown that the electronic properties of this system are different for each layer and depend on whether SiC is Si or C faced. SiC is a semiconductor [74], while the first carbon layer (buffer layer) can be either metallic (Si-terminated surface) or semiconducting (C-terminated surface). The second carbon layer possesses an electronic structure similar to freestanding graphene. In this work, the 6H-SiC(0001) substrate has a C-terminated surface.

Marchetto *et al.* performed macroscale friction force measurements with a tribometer in different humidity on the epitaxial graphene on the 6H-SiC(0001) sample [75]. They measured sliding friction between a ruby sphere and the sample with an applied normal load from 0.1 to 1 mN. The rupture of graphene and formation of the wear track was recorded. The tribological performance of epitaxial graphene on 6H-SiC(0001) was 5 times better than pristine SiC and better than that of graphite in the same conditions. It is suggested that the friction is a result of the tribological properties of the carbon buffer layer and the small patches of graphene remaining in contact. This study was also extended experimentally to the UHV [76]. The epitaxial graphene on 6H-SiC(0001) exhibits even better lubricity in the UHV than in ambient conditions. It was suggested that the reason, behind the improved lubricity is the lower amount of water and contaminants. It was also observed that the friction anisotropy of SiC, caused by steps of terraces, is eliminated by the graphene layer, due to the "carpet effect".

The epitaxial graphene on 6H-SiC(0001) can have more layers, which might be hidden in complex and confusing topography. Filleter *et al.* described a method to identify a number of graphene layers by combining information about topography and work function measured with Kelvin Probe Force Microscopy [KPFM] [77]. It is important because the number of epitaxial graphene layers on 6H-SiC(0001) also influences friction [78]. A monolayer of graphene exhibits ultra-low friction, but its coefficient of friction is around two times larger than that of a bilayer, whose coefficient of friction is similar to that of graphite. The graphene lattice starts to vibrate due to stick-slip sliding motion. This difference in friction is caused by the scale of the creation of electronic excitations through electron-phonon coupling, which dampens these lattice vibrations and causes energy dissipation.

Graphite has higher friction than graphene at lower normal loads due to a more compliant surface, which increases contact area and adhesion. The friction force measured on the carbon buffer layer (first carbon layer) is an order of magnitude higher in comparison to graphene layers.

Further extension of this research was published in the work of Filleter and Bennewitz [79], where other aspects of friction on epitaxial graphene on 6H-SiC(0001) were tested. A moiré superlattice was observed with periodicity 6x6 of the underlying SiC lattice in topography and lateral force images, which allows distinguishing in atomic scale between this system and graphite. Friction on mono- and bilayer graphene is independent of an applied electric bias or this dependence is insignificant. The linear ultra-low friction regime is limited to some normal load threshold from which the friction force increases significantly. This change in friction regime does not leave any changes in topography afterwards.

In this work, investigated 2D materials were stacked on SiC and SiO_x substrates. The SiC

substrate was selected instead of Pt, due to higher hardness and lack of plastic deformation before the rupture of the graphene layer. The SiO_x substrate was selected for being a standard substrate for the exfoliation technique.

Friction on van der Waals heterostructures

Stacking different 2D materials into van der Waals heterostructures opens a new large amount of options in tuning the properties of materials [42]. Vazirisereshk *et al.* [80] studied friction on heterostructures of graphene and MoS_2 layers on SiO_2. They observed that MoS_2 causes higher friction than graphene. The friction measured on MoS_2/graphene heterostructure was comparable to but occasionally lower than that for monolayer MoS_2. Quasi-static simulations with an empirical potential and with DFT showed that the cause behind this friction contrast is the difference in energy barriers to sliding on the two surfaces. The lower friction on the MoS_2/graphene heterostructure is a result of the dispersion contribution of the graphene to the energy barrier.

Graphene and hBN have almost identical lattices with only ≈1.8% mismatch. It leads to the formation of a large superlattice periodicity of ≈14 nm on graphene/hBN heterostructure. Depending on size, the moiré pattern can modulate the friction. The small mismatch of lattices makes the perfect alignment very favorable energetically. The graphene self-reorientates itself to align with the hBN orientation to decrease the strain [81]. On graphene/hBN heterostructure, Zhang *et al.* observed stick-slip motion with periodicity of the moiré pattern, next to atomic stick-slip [82]. Experiments and simulation based on the modified Prandt-Tomlinson model demonstrated that moiré pattern stick-slip causes an increase in the friction force with increasing normal load. Based on the modified Prandt-Tomlinson model, they attributed the moiré-scale stick-slip to the accumulation and sudden release of strain of the graphene layer. Huang *et al.* performed a very similar investigation on moiré pattern on graphene/hBN heterostructure. They also conducted simulations based on the modified Prandt-Tomlinson model and demonstrated that the cause of moiré pattern stick-slip is not only in-plane but also out-of-plane deformations. The formation of the moiré pattern depends only on the commensurability of immediate contact layers [82]. If the first layer of graphene is aligned with hBN, the moiré pattern is formed and is observable even if the following graphene layers are rotated. If the first layer of graphene is in misalignment with hBN, the moiré pattern is not formed, even if the following graphene layers are aligned with hBN.

Nanomanipulation of 2D materials

In van der Waals heterostructures, the lattice mismatch between 2D heterolayers or the relative rotation between 2D layers results in structural superlubricity between them. The onsequence of this structural superlubricity is an easy manipulation of flakes' positions and orientations with respect to each other. The first direct experimental evidence for superlubricity between two MoS_2 flakes was demonstrated by Li *et al.* [83].

A study of Büch *et al.* shows the manipulation of small flakes of WS_2 on epitaxial graphene on 6H-SiC(0001) in a superlubric regime by a scanning tip [84]. WS_2 triangular flakes with edge lengths around 600 nm were grown via CVD directly on epitaxial graphene on 6H-SiC(0001).

The initial orientation of WS_2 flakes is in the same direction as graphene lattice which is energetically most beneficial and stable. Atomistic force field-based molecular dynamics simulations demonstrated that the scanning tip may give enough energy via physical deformation of the WS_2 flake to initiate the superlubric movement of this flake. Such moving flake may ascend topographical steps and stops with rotation $n\pi/3$ with respect to graphene orientation. Liao *et al.* demonstrated that the nanomanipulation is not limited only to small flakes and that large flakes with a few μm of edge length can be rotated by means of the AFM tip [85].

Determination of coefficients of friction between two different 2D materials was attempted by Liao *et al.* [86]. Ultra-low coefficients of friction, $\mu \approx 10^{-6}$, without any twist-angle dependence, were reported for pairs of materials with large lattice mismatch: MoS_2/graphite and MoS_2/hBN. Experiments and simulations indicate that the friction between these two pairs is dominated by the so-called "edge-pinning effect" and interface steps. The edge-pinning effect is a result of the higher susceptibility of edge atoms to be trapped in the energy minima of the substrate. In the case of graphene on hBN, the small lattice mismatch results in friction significantly influenced by the interface friction.

2.2 The choice of investigated materials

As it was mentioned above, the linear ultra-low friction on epitaxial graphene on 6H-SiC(0001) is limited to some normal load threshold from which the friction force increases significantly. This problem of superlinear load dependence of friction force on epitaxial graphene on 6H-SiC(0001) is further explored in this dissertation in chapter 4. The change in friction regime does not leave any signs in topography and is explained by a change in hybridization in monolayer graphene from sp^2 to sp^3 at a high normal load.

Evidence for this hypothesis is described in the work of Gao *et al.* [87] where the monolayer of graphene on 6H-SiC(0001) under high normal load transforms into material harder than SiC. Such transformation occurs only for the double layer of carbon (carbon buffer layer and one layer of graphene) and prevents indentation through the surface. Contact current is reduced at some normal load, which indicates a drop in conductivity. DFT simulations have shown that the graphene layer undergoes structural sp^2 to sp^3 transformation and forms hexagonal diamond - Lonsdaleite. This material is metastable and turns back to the initial graphene phase when pressure is released. This 2D hexagonal diamond is called diamene [88]. The transition in hybridization was also tested with the utilization of the qPlus force sensor by Hofmann *et al.* [89]. The process of diamondization is not only limited to graphene on 6H-SiC(0001) and was also observed for multilayer hBN on SiO_2 [90].

The topic of pressure-induced chemical bonding is valid also for interlayer interactions between layers of van der Waals heterostructures. It was the initial motivation why the heterostructure of MoS_2 on epitaxial graphene on SiC(0001) was selected for investigation in this work. However, no experimental evidence was found for the formation of chemical bonds between MoS_2 and graphene, and its impact on friction. Therefore, the focus of the study on MoS_2/graphene heterostructure on SiC(0001) was shifted towards the investigation of bias voltage and layer number dependence of the friction. The details of this study are presented in chapter 5.

The selection of graphene/hBN and $MoSe_2$/hBN heterostructures was motivated by the extension of the above-mentioned studies to explore new combinations of heterostructures and their tribological properties. Barboza *et al.* [91] indicated in their study that simultaneous rehybridization and covalent binding of both graphene and hBN within graphene/hBN heterostructures is possible. Graphene and hBN have almost identical lattices, are isoelectronic and for both the pressure-induced diamondization process was observed [87, 90]. TMDC materials such as MoS_2 and $MoSe_2$ have similar properties, which makes it attractive to compare their frictional properties as a part of heterostructures with different materials: graphene and hBN.

The exfoliation method was used to prepare graphene/hBN and $MoSe_2$/hBN heterostructures. The method itself has disadvantages that cause problems in surface science studies. The size of exfoliated flakes and their distribution on the substrate makes it difficult to work without sufficient optical monitoring. The surface of exfoliated 2D materials is also very often not atomically flat, but folded, locally defective and contaminated. To improve the application of the exfoliation method for this thesis and future studies, a navigational microstructure was designed and prepared. Silicon dices with 90 nm oxide were used as a substrate due to its long and well-developed implementation with the exfoliation method. The results of this study is described in more detail in chapter 6.

3 Experimental methods

3.1 Materials

The 2D materials and their heterostructures are the subject of this work. Four different samples with various combinations of heterostructures were examined in this work. All of them were fabricated in collaboration with other research groups from Chemnitz, Berlin, Jena and Aachen.

3.1.1 Epitaxial graphene on silicon carbide

Epitaxial graphene on silicon carbide was prepared by the research group Prof. Thomas Seyller from the Institute of Physics at the University of Technology Chemnitz by the thermal decomposition method [72]. After previous preparation, 6H-SiC(0001) sample was annealed in an Ar atmosphere with a pressure of 900 mbar and at a temperature of around 1600°C. Photoelectron spectroscopy confirmed an average graphene coverage of 0.9 monolayers on atomically flat terraces of SiC(0001). Kelvin Probe Force Microscopy and an analysis of measured step heights identified small areas of bilayer graphene around step edges [77]. Small areas of bare SiC(0001) surface were located by a significantly higher friction contrast [78] with a layer of graphitic carbon connected directly to SiC and monolayers of graphene on it. The scheme of the epitaxial graphene on 6H-SiC(0001) is in figure 3.1a).

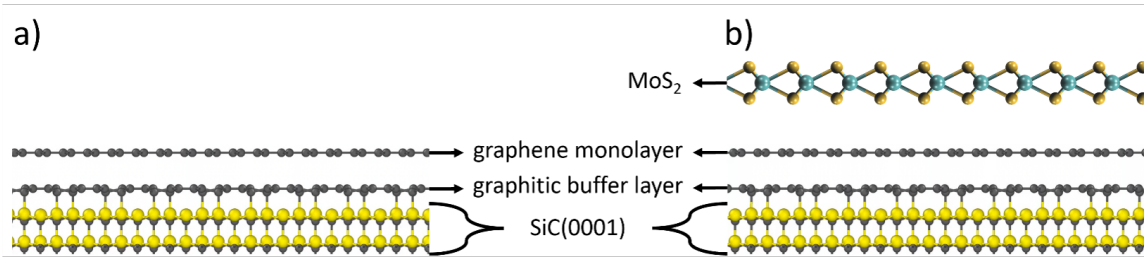

Figure 3.1: Schemes of 2D materials on 6H-SiC(0001): a) epitaxial graphene and b) heterostructure of MoS_2 and epitaxial graphene

3.1.2 Van der Waals heterostructures of MoS_2 on epitaxial graphene on silicon carbide

Van der Waals heterostructures of MoS_2 on epitaxial graphene on silicon carbide samples were prepared in two steps by Dr. Joao Marcelo J. Lopes from Paul-Drude-Institute for Solid State Electronics in Berlin and Dr. Antony George, Mr. Ziyang Gan from The Turchanin Research Group of Applied Physical Chemistry & Molecular Nanotechnology in the Friedrich-Schiller-University in Jena. The first step in the preparation of these samples was the growth of epitaxial graphene on 6H-SiC(0001) in Berlin [92]. The method of how it was done is described above. In the second step, MoS_2 was grown in Jena on the prepared graphene with the method described by George *et al.* [93, 94]. It is a chemical vapour deposition technique [CVD] that utilizes a Knudsen-type effusion cell to have better control over the flow rate of the chalcogen precursors and a two-zone split tube furnace to heat the precursors individually. MoO_3 powder and sulfur powder were used as precursors to prepare MoS_2 monolayers for this work. The scheme of the MoS_2 on epitaxial graphene heterostructure is on 6H-SiC(0001) in figure 3.1b).

3.1.3 Van der Waals heterostructures of $MoSe_2$ on hexagonal boron nitride and graphene on hexagonal boron nitride

Van der Waals heterostructures of $MoSe_2$ on hexagonal boron nitride and graphene on hexagonal boron nitride were prepared by the author of this work and Ms. Birgit Nothdurft from INM - Leibniz Institute for New Materials with Alexander Rothstein from the group of Prof. Christof Stampfer from 2^{nd} Physic Institute in RWTH in Aachen. The Si wafer with a defined SiO_x thickness of 90 nm was selected as a substrate to allow easy recognition of the number of graphene layers in an optical microscope [95]. The wafer was cut into dice with size 10mm $\times$ 5mm. Three navigational microstructures were fabricated on the dice by Focused Ion Beam in INM - Leibniz Institute for New Materials. Two heterostructures were assembled in steps by mechanical exfoliation and stamping on the separate navigational microstructure in RWTH in Aachen. Figure 3.2 illustrates the order of layers on both assembled heterostructures.

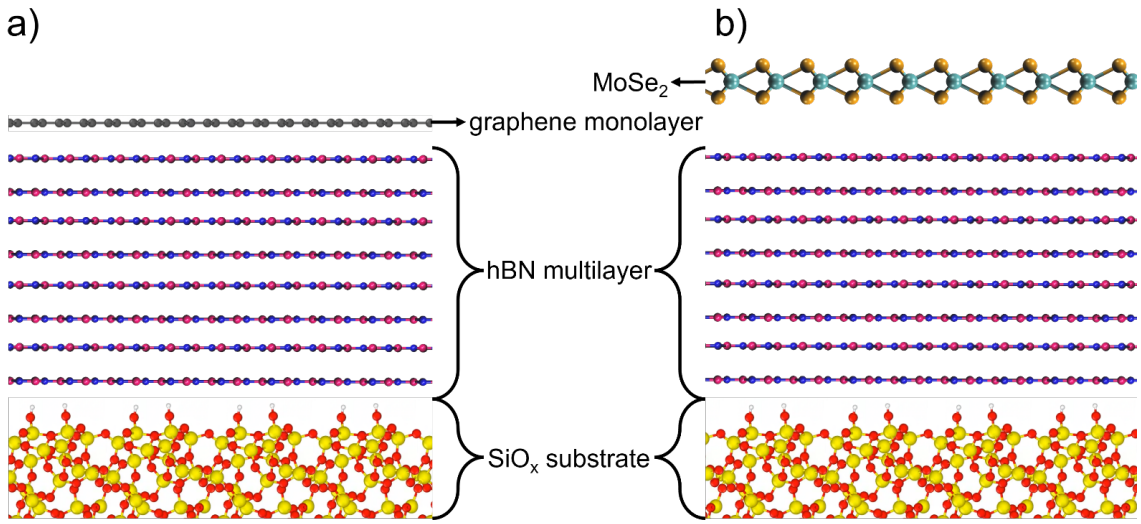

Figure 3.2: Schemes of 2D heterostructures on SiO_x: graphene on hBN and B) $MoSe_2$ on hBN

3.2 Navigational microstructure

The optical camera installed in the UHV-AFM system is limited to low resolution and is not sufficient to properly navigate over the sample. It is difficult to determine the exact position of the contact area between the probe and the sample surface based only on an image from the camera. It is impossible to locate the position of the area covered with 2D materials unless the sample substrate is properly fabricated. One method to enhance the visibility of 2D materials is growing the SiO_2 layer on a Si wafer substrate [95]. It allows optical observation of even single atomic layers due to the interference between the reflection paths that originate from the two air-to-SiO_2 and SiO_2-to-Si interfaces. In the system used in this work, it proved to be useful for the localization of large flakes of 2D materials, but not sufficient to determine which material is where on the sample. A navigational microstructure was designed to mitigate this disadvantage. Microlithography with the Focused Ion Beam [FIB] technique allows to fabricate precise groves, which can be located and recognized in different types of microscopes. All tests and fabrications were conducted with gallium ions on Versa 3D™ DualBeam™ from FEI™ and

with the help of Ms. Birgit Nothdurft. Silicon dices with size 10 mm× 5 mm and defined 90 nm of oxide layer on top were selected as a substrate for van der Waals heterostructures prepared by exfoliation.

The navigational microstructure consisting of three types of elements was designed by the author of this work. The first element is a target grid for the navigation with the UHV-AFM. The range of the AFM scanner is 4 μm× 4 μm, therefore large overview scans on the samples are impossible. The grid was designed to help navigate over an area of interest. The grid has the shape of a square with an edge of 200 μm and is divided into 4 μm× 4 μm squares (figure 3.3a)). Each square has easy for user to read, symbol-based coordinates: one number and two letters (figure 3.3b)). Numbers from 1 to 4 describe a quarter of the grid. Two letters are from the ISO basic Latin alphabet without "V" and describe the square's position within the quarter of the grid. The first letter describes a row, while the second describes a column. Additionally, the position where coordinates are drawn in each square depends on the quarter. This helps in locating the center of the target grid. A color bitmap template was prepared to upload and draw the grid via FIB microlithography. The template is black and white because the colors are scaling the depth of milling. The target grid is made with 30 kV of voltage, 100 pA of current, 500 passes and 2 μs of dwell time.

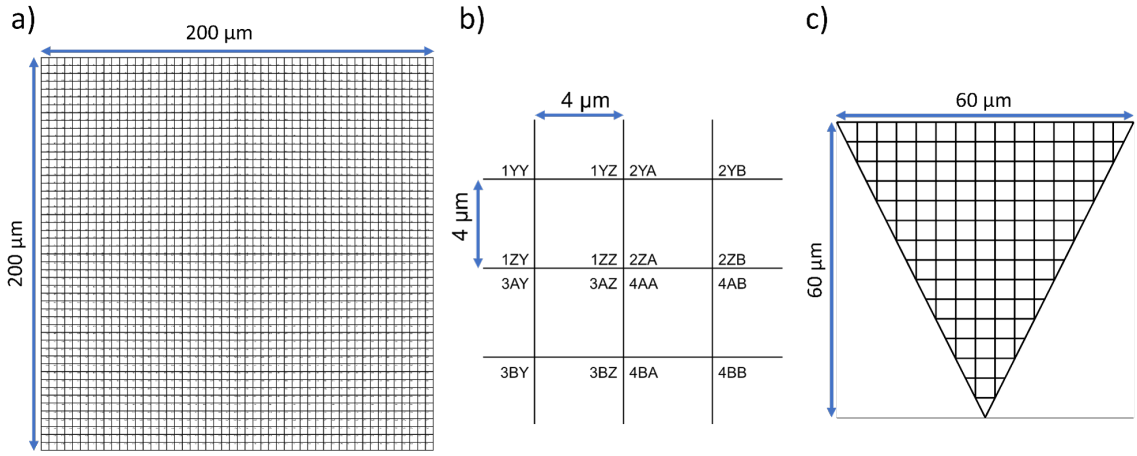

Figure 3.3: Design of the navigational grids: a) the target grid; b) squares with coordinates; c) triangular marker grid

The second element of the navigational microstructure is a crosshair for localization of the target grid in an optical microscope and assistance during the preparation of van der Waals heterostructures. The crosshair consists of six 100 μm long lines milled with 500 pA, 30 kV and a programmed depth of 50 nm. The number and position of lines are to make the structure asymmetrical and allow recognition of the orientation of the grid. The crosshair is being made first to avoid contamination of the target grid.

The third element of the navigational microstructure are markers. The role of markers is to help in navigation with the optical camera in the UHV-AFM system. They can be prepared as a grid or as a hole. Markers are made in the end at a distance of 500 μm from the grid to minimize contamination. There are two variants of markers. The first one is a simple hole, which can be drawn as a rectangle 60 μm×20 μm in FIB software and milled with 30 nA, 30 kV and with a programmed depth of 4.8 μm. The second variant is to use smaller grids in the shape of the

same rectangle or triangle 60 μm×60 μm (figure 3.3c)), which are milled with: 30 nA, 30 kV and with a programmed depth of 0.1 nm. Because the grid marker works as diffraction grating it is visible to the naked eye.

The scheme of the whole navigational microstructure is illustrated in figure 3.4a). The optical image of the finished navigational microstructure taken in an optical stereomicroscope (Olympus SZX16) is in figure 3.4b). In this work, prepared target grids were fabricated without contours of the squares and only with coordinates to minimize contamination.

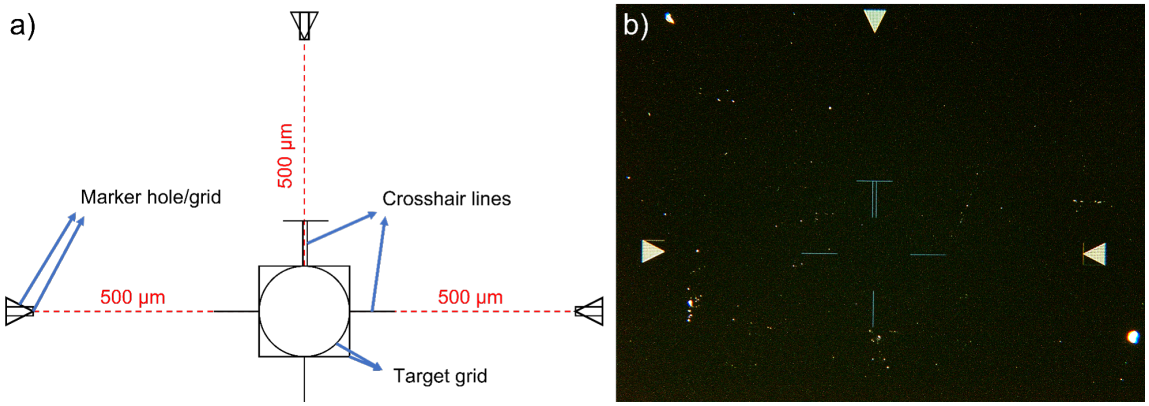

Figure 3.4: The navigational microstructure: a) scheme of the whole microstructure; b) optical image of the microstructure after preparation

In this work, two van der Waals heterostructures of graphene/hBN and $MoSe_2$/hBN were assembled on the navigational microstructures. Optical images of these heterostructures on the target grid (figure 3.5) work as a map for navigation over the sample. The strategy of navigation is based on three steps. In the first step, the cantilever is positioned between the markers and approached to distance for non-contact imaging. The second step is the imaging of the surface and readout of coordinates. Imaging is conducted in non-contact mode AFM to avoid modifications of the tip. In the third step position of the scanner is changed based on the location of currently observable and desired coordinates with a Micro Slide Control Unit [MSCU] in steps for better control of the distance. If no coordinates are visible in the maximum scanning range then the first step has to be repeated. Second and third steps have to be repeated until the desired area is reached.

3.3 Ultra high vacuum system

Most accurate experiments in surface science require well-defined, atomically flat, clean, and chemically stable surface. To achieve these requirements, the ultra-high vacuum [UHV] is needed. Based on the kinetic theory of gases and the Hertz-Knudsen equation [96], the flux Z of residual gas molecules striking the surface is described as 3.1:

$$Z_w = \frac{N_A p}{\sqrt{2\pi MRT}}, \tag{3.1}$$

where, N_A is the Avogadro's number [-], p is the pressure [Pa], M is the molar mass [$\frac{kg}{mol}$], R is the gas constant [$\frac{J}{K \cdot mol}$], and T is the absolute temperature [K]. This means that the probability of interaction between residual gas molecules or atoms with the surface is decreasing linearly

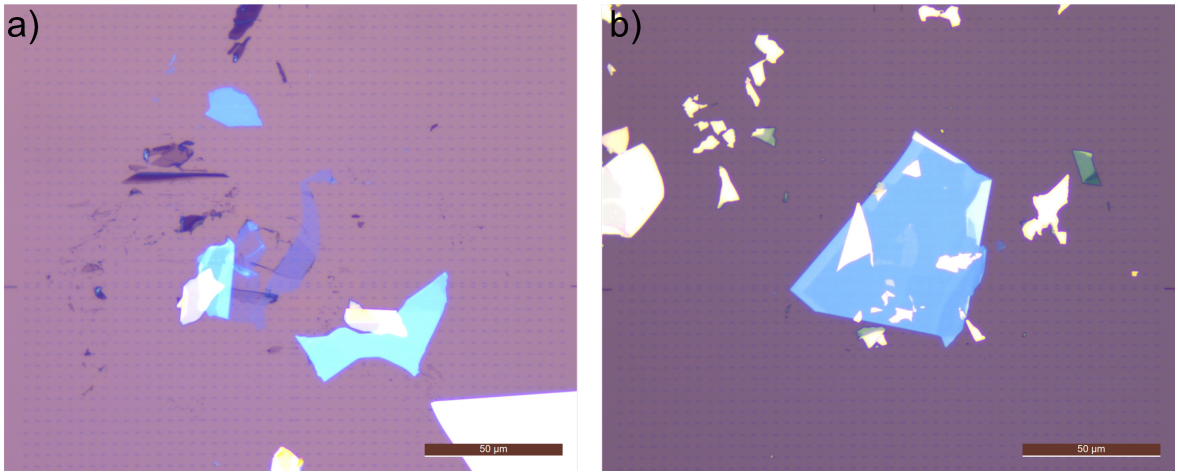

Figure 3.5: Optical microscope images of exfoliated heterostructures: a) graphene on hBN; b) $MoSe_2$ on hBN; scale bar 50 μm

with decreasing pressure. This probability is also influenced by the reactivity of the surface and molecules.

The UHV is usually defined as pressure between 10^{-8} mbar and 10^{-12} mbar. To artificially achieve these low values, the UHV system is required. The scheme of the UHV system used in this work is in figure 3.6 [97]. The UHV system consists of two connected chambers which can be isolated from each other with a valve. The first one, a Preparation Chamber, is designed to prepare samples and probes for experiments, while the second one, an Analysis Chamber, is designed to conduct experiments in the Varied Temperature Atomic Force Microscope [VT-AFM] from Scienta Omicron.

The UHV system has two groups of pumps with one for each chamber. The group of pumps consists of two suction pumps (Rotary Vane Pump for rough to medium vacuum and Turbomolecular pump for high to ultra-high vacuum) and two sorption pumps (Ion Getter pump and Titanium Sublimation pump for high to ultra-high vacuum). The pressure inside chambers is being monitored via ion gauges and electric current indicators of Ion getter pumps. Their values are registered on a daily basis or more often when quick changes in pressure are expected e.g: during the transfer of materials between both chambers, introduction to or recovery from the UHV system or during heating.

Introduction and operation in the UHV system require special preparation of samples and probes. Each element has to be fixed mechanically or by means of a low-degassing glue to the special holder and/or transfer plate. Probes are attached to holders designed for VT-AFM. Epoxy glue containing silver particles used for attachment allows to perform electric current measurements. Transfer plates for probes and samples have to comply with the Omicron standard allowing for transfer and storage within the UHV system. Fixed elements are being introduced to the UHV system via Fast Entry Lock to the Preparation Chamber, where they can be degassed from water and other adsorbents by heating for at least 2 hours at a certain temperature. All probes were degassed after introduction to the UHV system and before experiments by resistive heating an a temperature of at least 120°C. Samples with SiC as a substrate were heated to a temperature around 600°C by direct current put through the sample. At this temperature, SiC starts to glow slightly. Samples based on Si substrate were degassed by

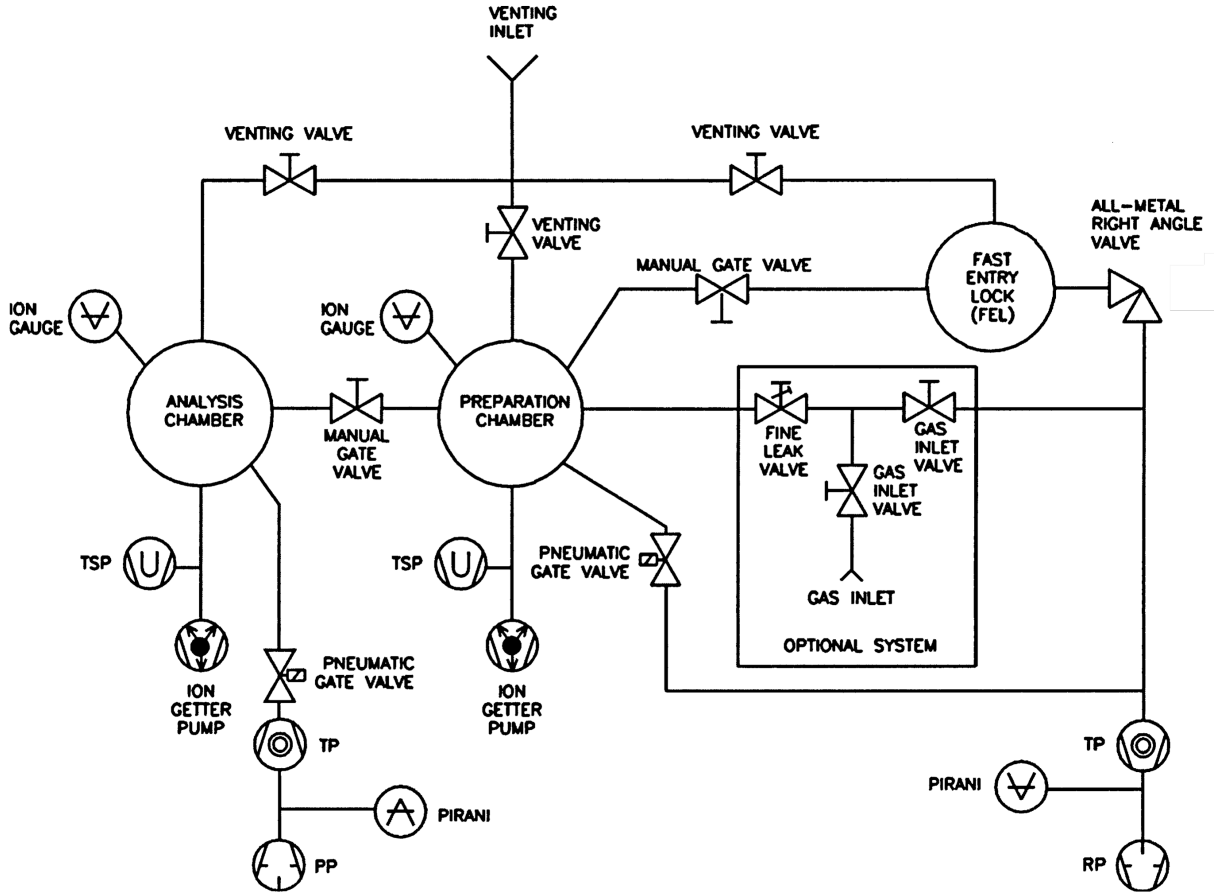

Figure 3.6: Diagram of the UHV System [97]

resistive heating at a temperature of at least 120°C. Some samples were degassed only between or after experiments.

After the preparation, samples and probes were transferred and stored in the Analysis Chamber in a carousel designed for the storage of up to 12 samples/probes. The procedures described above allowed to perform all friction experiments in the UHV with pressure around 1×10^{-10} mbar and at room temperature.

3.4 Atomic force microscopy

Atomic force microscopy is a basic experimental method used in this work. The development of this method started with the invention of the scanning tunneling microscope [STM] in 1981 by Binnig and Rohrer [98, 99, 100]. Their work was awarded with the Nobel Prize in Physics in 1986 [101] and began a new family of microscopy, the scanning probe microscopy [SPM]. STM allows imaging of the density of electron states in atomic resolution through measurement of tunneling current between the probe and conductive sample. The atomic force microscope was invented in 1986, by Binnig, Quate, and Gerber [28] and allowed the imaging of non-conductive samples, because of the different working principles of the AFM. After that, many variations and methods were developed for SPM techniques and enabled experiments with many different forces and phenomena in the nanoscale, accelerating the development of nanotechnology and nanoscience.

3.4.1 Structure of microscope

The working principles of the AFM are illustrated in figure 3.7. Interactions between the probe and the sample bend and twist the cantilever. The laser beam directed on the reflective side of the cantilever deflects and hits the four-segmented photodiode. The bent or twisted cantilever changes the deflection of the laser beam, which in turn changes the position where the laser beam hits the photodiode. Vertical and horizontal deflection signals are calculated and recorded based on the position where the laser beam hits the photodiode. Upon calibration, normal and lateral forces can be calculated from vertical and horizontal deflection signals respectively. AFM can work with an open or closed feedback loop. In the open feedback loop, the scanner maintains a constant position in Z. In the closed feedback loop, the vertical deflection signal is then used for feedback to control position Z of the piezoscanner and maintain constant applied force. The position Z and other signals are being recorded by computer as a function of positions X and Y of the piezoscanner.

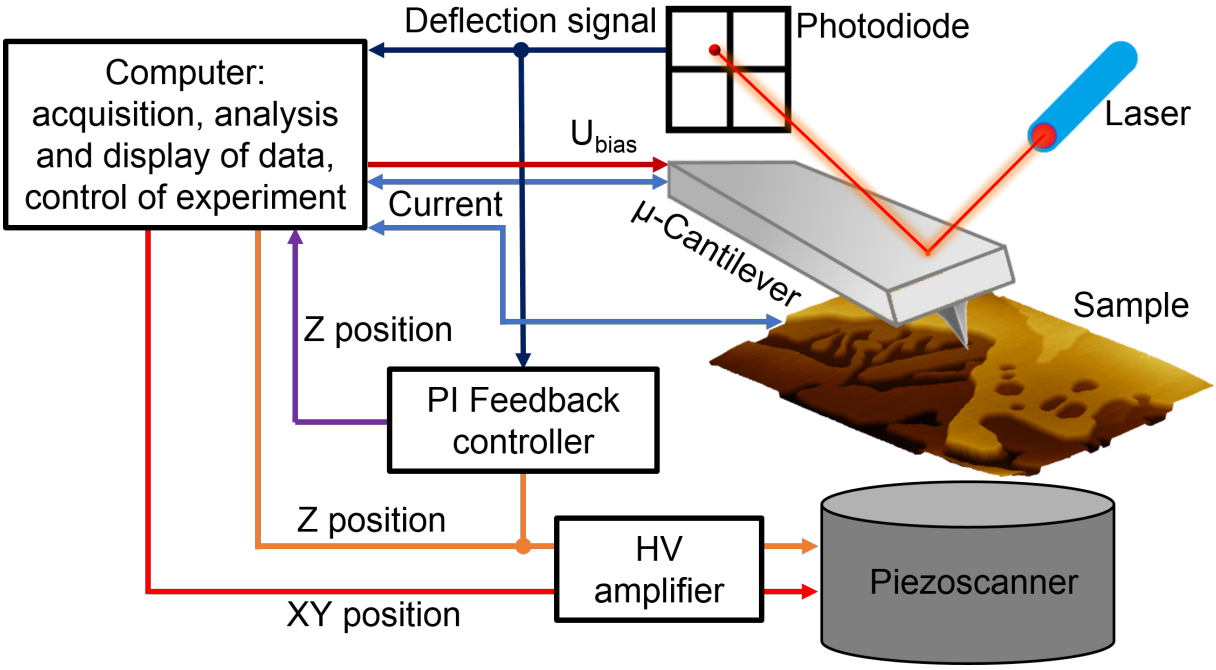

Figure 3.7: Scheme of atomic force microscopy

All AFM measurements were conducted in VT-AFM. It is a scanning cantilever microscope, where the sample is static, and the high voltage piezoelectric tube scanner controls the position of the cantilever. The range of the scanner in XY axis is 4.2 μm $\times$ 4.2 μm and in Z axis 1.18 μm. A small range in XY axis prevents from conducting large overview scans. Both the sample and the scanner are integrated into a metal stage.

The anti-vibrational system is based on springs and magnets. The metal stage can be locked in an elevated or lowered position with the usage of a push-pull motion drive. In the elevated position, the stage stays on the motion drive and receives vibrations from the chamber. In the lowered position, the whole stage is suspended on springs to reduce vibration. Magnets are implemented to induce the Eddy current to damp the vibrations.

The optical detection system is integrated with the scanner and consists of mirrors, four-

segmented photodiode and an infrared laser. A position of mirrors can be adjusted externally by MSCU to properly aim the laser beam onto the cantilever and the photodiode. The sample and the cantilever can be monitored in real time via a camera integrated with the optical system. It supports optical adjustment, approach and retraction of the cantilever as well as positioning of the scanning area on the sample. However, a black&white image, an angle of the camera and limited optical magnification hamper the approach to well-defined positions on the samples.

The software and most of the electronic hardware for the experiment control, as well as gathering and analyzing of data was acquired from Nanonis™. The application of normal load results in the bending of the cantilever, which additionally changes the tilt of the tip with respect to the sample and its contact position with the sample [102]. To compensate for the normal load-related change in the contact position, a homemade electric device was connected.

3.4.2 AFM measurements techniques

To ensure reliable and reproducible data, different AFM modes and techniques were combined in every single experiment. In this work, the AFM techniques can be divided into two modes of measurements. The first, contact mode keeps the tip in contact with the surface and allows to measure short range interactions such as: lateral forces, electrostatic and van der Waals interactions. The second, non-contact mode keeps the tip out of contact and allows to measure long range interactions such as: magnetic, electrostatic and van der Waals interactions.

Contact mode techniques:

– **Lateral Force Microscopy [LFM]** – (known also as Friction Force Microscopy [FFM]) – Scanning is done forward and backward in a direction perpendicular to the cantilever's axis, which twists the cantilever due to lateral forces. Twist changes the deflection of the laser beam, which is then registered by the four-segmented photodiode. The idealized scheme of the working principles of the lateral force microscopy is in figure 3.8. The friction force signal has to be extracted from the lateral signal because changes in topography also twist the cantilever. The friction force signal U_L [V] is calculated according to equation 3.2 from forward U_{Lfwd} and backward U_{Lbwd} lateral signals [V]:

$$U_L = \frac{U_{Lbwd} - U_{Lfwd}}{2} \tag{3.2}$$

Materials with different coefficient of friction can be distinguished with this technique. Forward and backward lateral signals in one line create a characteristic hysteresis called friction loop. It is caused by different direction of the lateral force and results in a run in period when the cantilever twists from one direction to another. With proper conditions, an atomic stick-slip motion with crystallographic lattice periodicity of the sample can be observed. In this work, all friction force measurements were based on lateral signal maps with size 8 nm $\times$ 2 nm, registered in 128 lines divided into 512 points per line and open feedback loop. Each friction force experiment consists of a series of measurements with increasing and decreasing normal load or as a function of another parameter.

– **Force Spectroscopy [FS]** – a point test, where the cantilever is moved only in a Z axis in both directions. This test has two phases. In the first phase, the cantilever is approaching the sample.

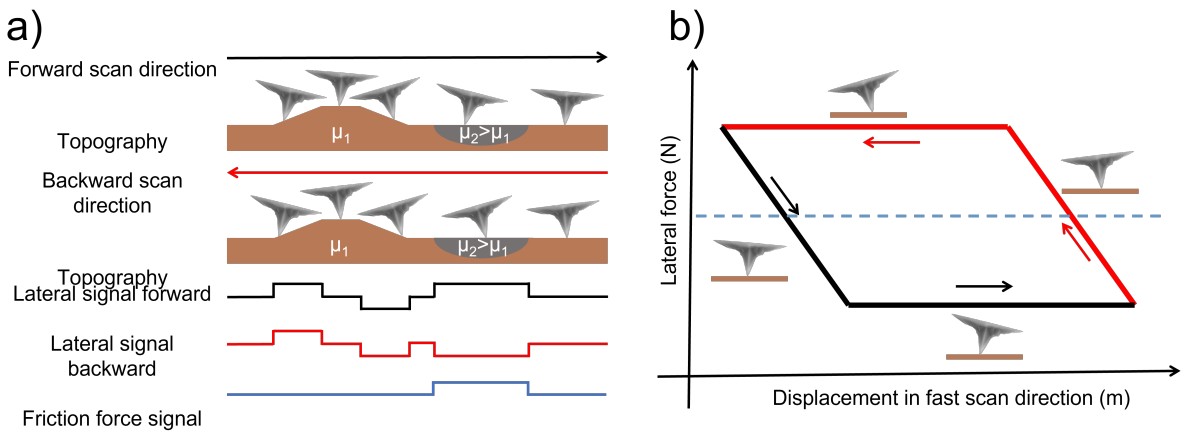

Figure 3.8: Principles of operation of the lateral force microscopy: a) an idealized extraction of friction force signal from lateral signal; b) a friction loop

When $\frac{dF_{atr}}{dz} > k$, attractive forces are no longer fully compensated and the instability causes the tip to jump into contact with the surface of the sample. After the tip connects to the surface the further approach of the cantilever causes an increase in normal load between the tip and the sample. In the second phase, the cantilever is being retracted, which causes a decrease in the normal load between the tip and the sample to the moment of loss of the contact. Depending on the setting, the range of this test is manually limited within the range of the extension of the Z axis piezoelement or the range of the measured signal. From this test, it is possible to measure: the force of adhesion, the offset of the vertical signal from 0 N normal load and the sensitivity of the cantilever. From the shape of the curve and the measured adhesion force it is possible to also get information about the status of the tip. The adhesion force is proportional to the contact area. If measured adhesion is low ($\approx$ 8 nN), the tip is sharp, and if adhesion is high ($\geq$ 30 nN), the tip is already flattened. Single detachment event means single asperity contact, whereas multiple detachment events or irregular shape of the curve may indicate multiple tip effect or adsorption of some contaminants. In this work, the normal load applied during FS measurements was usually below 20 nN.

– **Conductive AFM [cAFM]** – In this technique, the voltage bias U_{bias} is applied to the sample and causes flow and measurements of electric current. Lack of the current could mean that at least one of the elements in a circuit (tip, cantilever, sample, holders, etc.) is not conductive. This technique allows to locate materials with different conductivity or determine changes in the conductivity of the sample based on other variables. In this work, this technique was used simultaneously with LFM in experiments on samples based on SiC.

Non-contact mode techniques:

– **Dynamic Force Microscopy [ncAFM]** – In this technique, the cantilever is excited to oscillate at resonant frequency or higher harmonics. It is done by application to the piezoactuator an amplified, phase shifted electric signal, which oscillations are proportional to that of the cantilever. The tip-sample interactions cause the frequency of the oscillation to shift. This frequency shift signal is used to control position Z of the piezoscanner. The constant amplitude of oscillation is maintained by an additional feedback circuit. This technique allows for scanning the topography without wear of the tip. Different materials can be distinguished by different

frequency shift and excitation. It is especially useful for 2D materials to determine the number of layers because the tip-sample interactions are strongly dependent on thickness for atomically thin films.

– **Bias spectroscopy [BS]** – a point test, where frequency shift is measured as a function of voltage bias U_{bias}. It allows to determine the value of contact potential difference [CPD] as compensation voltage bias U_{CPD}. If applied U_{bias} is equal to U_{CPD}, the frequency shift has minimized the absolute value, due to a decrease of electrostatic forces. U_{CPD} is characteristic for each material.

– **Kelvin Probe Force Microscopy [KPFM]** – is an assisting technique to ncAFM, which allows a continuous mapping of U_{CPD}. The bias voltage U_{bias} is additionally modulated by a small AC voltage: $U_{bias} = U_{DC} + U_{AC}sin(\omega t_{KPFM})$, where ω is a modulation frequency [Hz] and t_{KPFM} is a period [s]. A lock-in amplifier records frequency shift and an additional feedback circuit maintains it's value at zero by adjustment of U_{DC}. This allows to map local U_{CPD} and identify different materials as well as determine the number of layers of 2D materials.

Experiments were based on the following strategy: 1) Experiments start with non-contact mode techniques. The area is being scanned with ncAFM to locate a suitable place for friction experiments; 2) KPFM image checks the suitability of the place by identification of materials and the number of their layers; 3) CPD is measured on selected materials; 4) Experiments shifts to contact mode techniques. Single FS measurement is done to measure adhesion, estimate the quality of the tip and check the value of vertical offset; 5) LFM experiment series is conducted to measure friction with increasing and then decreasing normal load. Depending on the experiment the cAFM can be used for electric current measurements; 6) Friction measurements series is being closed with a single measurement out of contact to acquire background signal and FS test to check changes in adhesion and vertical offset.

3.4.3 Probes and cantilevers

In this work, different types of rectangular cantilevers were used for experiments. The selection of cantilevers was balanced between soft (k≈0.2 N/m) and medium stiff (k≈2.8 N/m) cantilevers due to the limited range of the piezoscanner in the Z axis (limits soft cantilevers), the limited range of photodiode in the vertical direction (limits medium stiff and stiff cantilevers), the importance of high contact pressure and lateral sensitivity in this work. Interactions between samples and silicon/silicon oxide or diamond tips were explored. Silicon based tips were selected to match simulations conducted in parallel to the experiment, whereas diamond based tips were selected due to their hardness and low wear.

- **PPP-CONTR**: soft cantilevers with a silicon tip limited to low normal loads (up to 500 nN). It has high lateral sensitivity, which allows more accurate measurements of friction. In this work, the PPP-CONTR was used for experiments on all samples. Acquired from NANOSENSORS™;

- **PPP-FMR**: medium stiff cantilevers with a silicon tip limited to medium normal loads (up to 1500 nN). It has lower lateral sensitivity than PPP-CONTR, which may result in inaccurate measurements of friction. In critical cases, no twist of the cantilever is being

recorded and all lateral forces cause additional bending of the cantilever. In this work, the PPP-FMR was used for experiments on all samples. Acquired from NANOSENSORS™;

- **DT-FMR**: a stiff cantilever with a tip made of a polycrystalline approximately 100 nm thick diamond coating allows to achieve normal loads up to 3000 nN. In this work only one such cantilever was used and only for experiments on epitaxial graphene on SiC. Acquired from NANOSENSORS™;
- **ADAMA**: model AD-2.8-AS, medium stiff cantilevers with a sharp monocrystalline diamond tip grown on the silicon cantilever tip allows to reach up to 1000 nN of normal load. The tip is boron doped (7000 - 8000 ppm), which results in high conductivity and allows more sensitive electric current measurements than silicon tips. In this work, this cantilever was used on epitaxial graphene on SiC and MoS_2/graphene heterostructures on SiC. Acquired from Adama Innovations.

Table 3.1 contains nominal values provided by the manufacturer of parameters of cantilevers utilized in this work. These nominal values of length, mean width and tip height were used for calibration and data analysis in situations when the cantilever sizes were not measured.

Table 3.1: Nominal parameters of utilized cantilevers

	length	mean width	tickness	tip height	stiffness	resonant frequency
name	[μm]	[μm]	[μm]	[μm]	[N/m]	[kHz]
PPP-CONTR	450	50	2	12.5 ± 2.5	0.2	13
PPP-FMR	225	28	3	12.5 ± 2.5	2.8	75
DT-FMR	225	27.5	3	12.5 ± 2.5	6.2	105
ADAMA	225	50	1.5	12.7 ± 2.6	2.8	75

Post-experimental analysis of cantilevers

To ensure full understanding of obtained experimental results, part of the cantilevers was additionally analyzed outside of the UHV system. After the experiments, cantilevers were examined in transmission electron microscope [TEM] to determine structure, material, and curvature of the tip apex or in scanning electron microscope [SEM] to measure exact sizes of the cantilever (figure 3.9). TEM imaging was conducted with help of Dr. Marcus Koch on JEOL JEM-2100 LaB6 TEM at 200 kV. SEM measurements were done by Dr. Marcus Koch and Ms. Aude Haettich on FEI ESEM Quanta 400 FEG at 10 kV. Images taken in TEM and SEM were further analyzed in microscopes software and ImageJ.

3.4.4 Cantilever calibration and data analysis

Calibration of the cantilever occurs mostly after the experiments, partially during automatized analysis of measured data. Calibration is based on the beam geometry method [103]. It is an analytical method [104] where the normal stiffness k_N and torsional stiffness k_T of the cantilever are calculated based on a simplified geometry of the cantilever. It is assumed that the cantilever is homogeneous, isotropic, exhibits linear elastic behavior and has a shape of a perfect cuboid with the tip at its end.

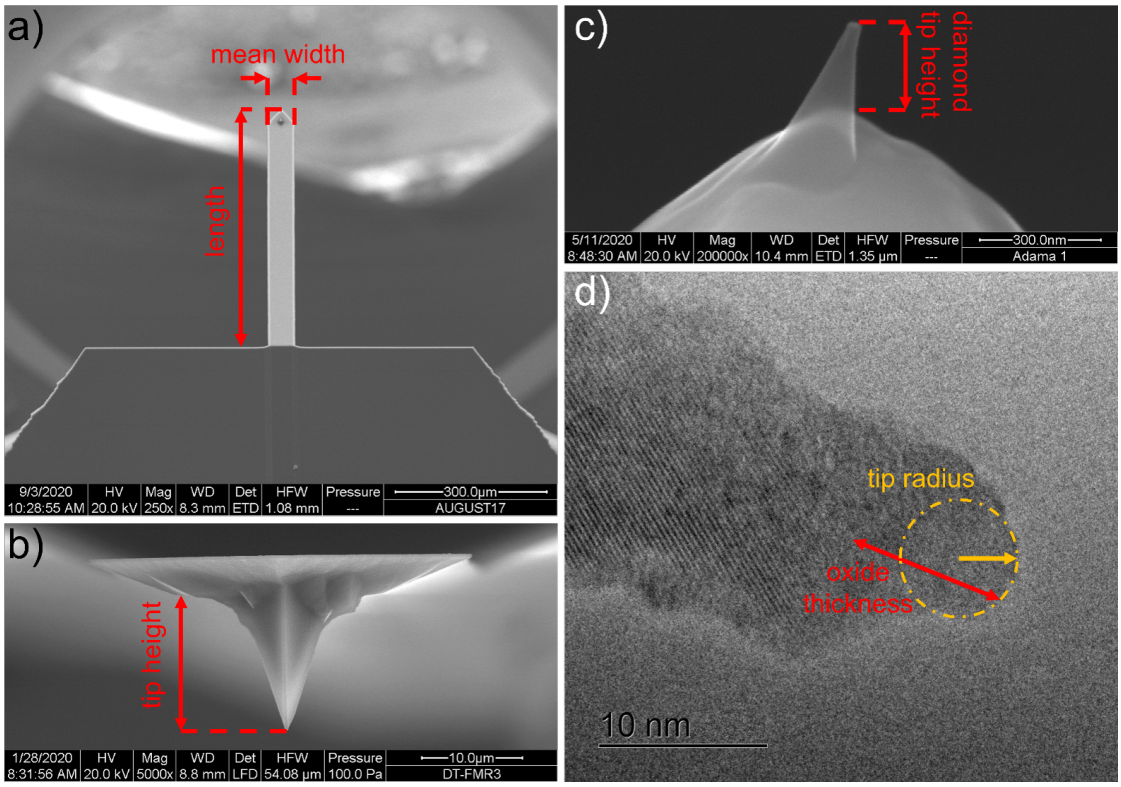

Figure 3.9: SEM and TEM images of cantilevers after experiments: a) SEM image of the PPP-CONTR cantilever from the top; b) SEM image of the DT-FMR cantilever from the front; c) SEM image of the diamond tip of the ADAMA cantilever; d) TEM image of the PPP-CONTR cantilever tip

Normal stiffness k_N $[\frac{N}{m}]$ is calculated from the equation 3.3:

$$k_N = \frac{Ewt^3}{4l^3}, \tag{3.3}$$

where, E is the Young modulus $[\frac{N}{m^2}]$, which for silicon has value $E_{Si} = 1.69 \times 10^{11}$ $\frac{N}{m^2}$, w is the mean width of the cantilever [m], t is the thickness of the cantilever [m] and l is the length of the cantilever [m]. Values of l and w were taken either from SEM images or from nominal values, which due to the method of manufacturing are very close to real values. Thickness t of the cantilever was always determined based on the resonant frequency f_I [Hz] of the cantilever and equation 3.4:

$$t = \frac{2\sqrt{12}\pi}{1.875^2}\sqrt{\frac{\rho}{E}}f_I l^2, \tag{3.4}$$

where, ρ is a mass density $\frac{kg}{m^3}$, which for silicon is $\rho_{Si} = 2330$ $\frac{kg}{m^3}$.

Every measurement in contact mode is done with a certain setpoint of vertical deflection signal U_V [V]. The exact value of normal load F_N [N] is calculated from equation 3.5:

$$F_N = U_N k_N S_N, \tag{3.5}$$

where, U_N is the normal load signal [V] calculated from equation 3.6:

$$U_N = U_V - U_{N\infty} \tag{3.6}$$

where, $U_{N\infty}$ is the offset [V] from 0 N normal load. S_N is a normal sensitivity of the detector $[\frac{m}{V}]$. A raw signal U_V is measured directly, while S_N and $U_{N\infty}$ can be acquired from the FS test. The value of $U_{N\infty}$ may change over time during the experiment due to drift. The value of $U_{N\infty}$ is measured before and after each whole series of friction measurements. Correction to the normal load of each measurement is applied based on the number of measurements done between both FS tests and values of $U_{N\infty}$ before and after every series of friction measurements.

Torsional stiffness k_N $[\frac{N}{m}]$ is calculated from the equation 3.7:

$$k_T = \frac{Gwt^3}{3h^3l}, \tag{3.7}$$

where, h is the magnitude of the position vector [m] and is calculated from $h = h_{tip} + \frac{t}{2}$, where h_{tip} is the tip height [m]. G is a shear modulus $[\frac{N}{m}]$ and is calculated from the equation 3.8:

$$G = \frac{E}{2(1+\nu)} \tag{3.8}$$

where, ν is the Poisson's ratio [-], which for silicon has value $\nu_{Si} = 0.278$. Friction force F_L $[N]$ is determined by equation 3.9:

$$F_L = \frac{U_L k_T S_L}{gain} \tag{3.9}$$

where, U_L is the friction force signal [V] calculated with the equation 3.2, S_L is a lateral sensitivity $[\frac{nm}{V}]$ and $gain$ is an amplification applied to the lateral signal during the experiment [-]. The lateral sensitivity S_L is calculated from the normal sensitivity through equation 3.10:

$$S_L = S_N \frac{3h}{2l} \tag{3.10}$$

At the last step average value of friction force and electric current are calculated from entire maps and collected in a table of results from the whole friction measurements series. All these calculations are performed by means of MATLAB script, which code is in Appendix I.

3.5 Simulation methods

All simulations in this work were performed by Dr. Takuya Kuwahara, Dr. Leonhard Mayrhofer and Dr. Andreas Klemenz from the group of Prof. Michael Moseler from the Fraunhofer Institute for Mechanics of Materials IWM in Freiburg.

Atomistic details on the friction dynamics between a graphene/SiC(0001) and Si tip were investigated using the self-consistent charge-density functional tight-binding molecular dynamics [DFTB] method [105] as implemented in the ATOMISTICA software suite [106]. Since the topmost surface of the Si tip is covered with an amorphous SiO_2 (a-SiO_2) layer (figure 3.9d)), a contact between a graphene/SiC(0001) and an a-SiO_2 surface was modeled. The graphene/SiC(0001) surface was constructed from a monolayer graphene, a carbon interface layer, and a C-face SiC(0001) surface with six layers in a periodic cell with dimensions of $9.2 \times 10.7 \times 50.0$ Å^3. The a-SiO_2 samples, containing 50 Si and 100 O atoms, with the same XY dimensions and a density of 2.2 g cm^{-3} were prepared by quenching SiO_2 melts under periodic boundary conditions along the three Cartesian directions while keeping the cell size

constant. A slab geometry was created by cutting the a-SiO_2 bulk perpendicular to the Z axis and introducing a vacuum layer. Undercoordinated Si and O atoms on both surfaces were terminated with OH groups and H atoms, respectively.

Sliding DFTB simulations were performed for 0.3 ns with the Pastewka-Moser-Moseler pressure-coupling algorithm [107]. Top and bottom layers of the SiO_2 and graphene-SiC slab were kept rigid, respectively. A normal pressure P_Z ($1 \leq P_Z \leq 40$ GPa) and sliding speed v of 100 ms^{-1} were imposed on the rigid layer of a-SiO_2 along the X axis, whereas the positions of the rigid layers of the graphene-SiC(0001) surface remained unchanged. The sliding speed of 100 m/s is 10 orders of magnitude larger than that in the experiments. The use of such a high sliding speed is essential to simulate a long sliding distance and sufficiently sample phase space, and typical in atomistic simulations. In principle, the sliding speed has to be much smaller than the speed of sound in solids so that the heat generated at the sliding interface can be dissipated to surrounding bodies (which is modeled by coupling the thermostat to the system in this study). Considering that the speeds of sound in SiC ($\approx$ 11 km/s) and silica ($\approx$ 6 km/s) are much higher than the sliding speed of 100 m/s in the simulations, It is expected that this value allows to properly model interfacial dynamics of graphene with SiC and SiO_2 under shear.

The system temperature T was kept constant at 300, 500, and 1000 K using a Langevin thermostat [108] acting only along the perpendicular to the sliding direction. The equations of motion were integrated with a time step of 0.5 fs using the velocity Verlet algorithm [108]. The shear stress τ was calculated from the forces along the X axis acting on the rigid layers of SiO_2 and averaged over the last 0.1 ns. To investigate the effect of the sliding speed, another set of simulations with a lower sliding speed of 10 ms^{-1} was performed at $T = 300$ K for 3 ns (corresponding to the sliding distance of 30 nm) while keeping the other parameters unchanged. The shear stress is calculated by summing the force component along the sliding direction on all atoms in the top rigid layer and then dividing by the lateral area of the simulation cell.

4 Friction force on epitaxial graphene under high contact pressure

This chapter reports nanotribological investigations on monolayer epitaxial graphene on SiC(0001). Experiments and simulations on the friction force as a function of increasing normal load conducted with SiO_x probes as well as TEM images are incorporated from the article of Szczefanowicz et al. [1]. Material related to electric conductivity under high contact pressure is exclusive only to this work. Measurements with diamond tips are planned for publication and at the moment are exclusive only to this work. The influence of normal load and electric bias on friction force and electric current were studied between the surface of epitaxial graphene on SiC(0001) and SiO_x (PPP-ContR) or diamond (ADAMA AD-2.8-AS, DT-FMR) probes. The DFTB simulations for SiO_x probes were conducted by the group of Prof. Michael Moseler from the Fraunhofer Institute for Mechanics of Materials IWM in Freiburg. It will be presented and discussed in this chapter how high contact pressure is changing the nanotribological and conductive properties of monolayer epitaxial graphene on SiC(0001).

4.1 Experimental results

4.1.1 Transition between nanoscale friction regimes

Typical results for friction versus normal load are presented in figure 4.1 together with the TEM image of one of the tips recorded after the friction experiments. For the first contact of an oxidation-sharpened silicon tip (figure 4.1a)), friction is ultra-low with a linear load dependence and a corresponding friction coefficient of 0.000 94 for normal forces up to 50 nN. For a load of 60 nN, friction suddenly increases by almost one order of magnitude. Friction forces vary around 0.6 nN with significant scatter until 170 nN of normal load, above which friction increases rapidly reaching the value above 2.2 nN at 300 nN of normal load. Friction sometimes drops like in the data recorded at 130 nN load compared to the data recorded at 120 nN or at 280 nN in comparison to the data recorded at 270 nN of normal load.

When the experiment was repeated with the same tip starting again at a low normal load, the same linear ultra-low friction regime and the steep increase at 60 nN of normal load were found. Friction force forms a plateau and remains constant from 70 nN to 150 nN of normal load. The friction force transits to the high-friction regime at higher normal loads and reaches the value of around 2.2 nN. The scatter of data is much smaller in this second series. In the third series of measurements with the same tip, the linear ultra-low friction regime is recorded until 100 nN of normal load. After the increase, the friction force reaches the plateau between 130 nN to 200 nN of normal load, above which transition to the high friction regime occurs.

Results for a different AFM tip are shown in figures 4.1b) and 4.1c). In the first series of measurements, the linear ultra-low friction regime with a coefficient of 0.0016 was recorded for normal forces up to 80 nN. For a load of 100 nN, friction suddenly increases to a value around 15 times higher. For higher normal loads, the friction values tend to even higher values, however with significant scatter in the data. In the second series of measurements with this tip starting again at a low normal load, the same linear ultra-low friction regime and the transition to the high-friction regime were found. The transition to the high-friction regime is more gradual than in the first run. High-friction values above 2 nN are reached only at a load above 340 nN,

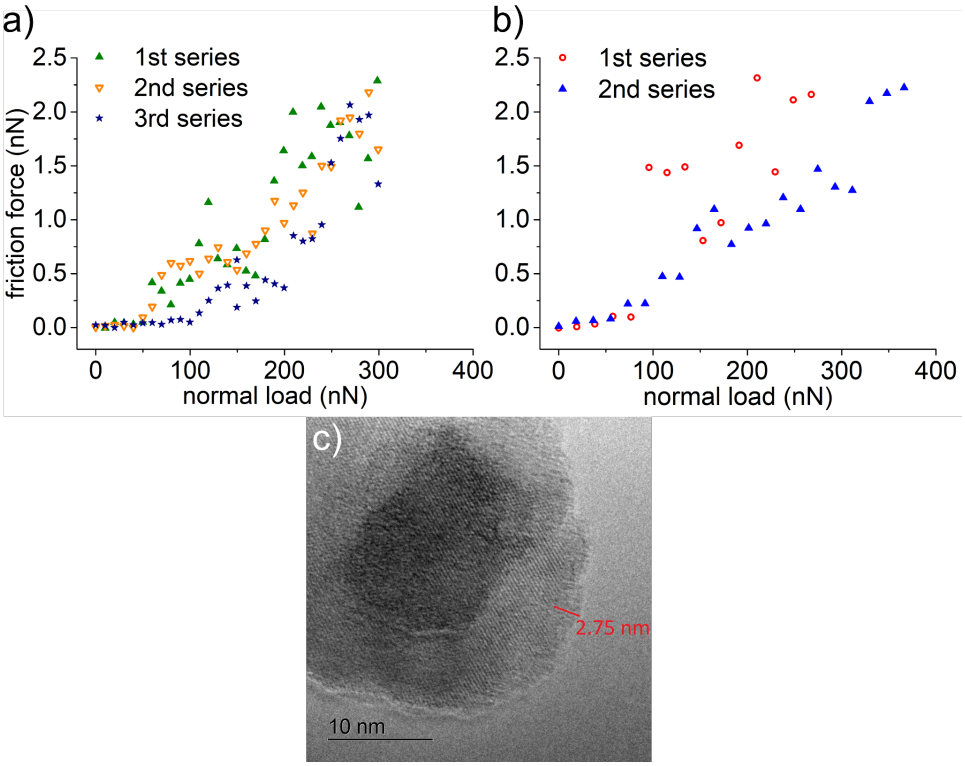

Figure 4.1: Friction force as a function of increasing normal load between an oxidized silicon tip and epitaxial graphene on SiC(0001): a) and b) are the friction results of experiments with two different cantilevers; c) TEM image of the tip from b), where atomic planes of the single-crystal structure of the silicon tips appear as lines and the surface oxide at the top apex as amorphous layers.

compared to 200 nN in the first run.

After these two series, this tip was removed from the vacuum system and immediately imaged by TEM. The image in figure 4.1c) confirms the crystalline structure of the silicon tip and an amorphous silicon oxide surface layer on the tip apex of about 2.75- nm thickness. The overall radius of the oxidized apex can be estimated to be 5–10 nm.

Entering the high-friction regime does not damage the graphene or the underlying substrate, as it was confirmed by topographic imaging of the area before and after each friction experiment. The author of this work recorded topography after each friction experiment in only low-resolution images. One high-resolution example was recorded by Prof. Tobin Filleter and is shown in figure 4.2 [1]. No change in topography was recorded in images before (figure 4.2a)) and after (figure 4.2b)) the experiment, even though the high-friction regime was reached at around 280 nN of normal load (figure 4.2d)). During the experiment, a stick-slip and a moiré pattern of the epitaxial graphene on SiC(0001) were recorded in lateral signal (figure 4.2c)). The stick-slip has a periodicity of 260 pm, which is comparable to the theoretical graphene lattice constant of 246 pm. The theoretical 6H-SiC(0001) lattice constant is 307 pm [109]. The incommensurability of graphene and 6H-SiC(0001) causes the formation of the moiré superstructure with symmetry $(6\sqrt{3} \times 6\sqrt{3}) - R30^\circ$ [110].

The experiments demonstrate an ultra-low friction regime and its transition to a regime of higher friction above a threshold load, which leaves the graphene layer intact. This high-friction regime is characterized by a superlinear increase in friction as a function of load and irregular jumps between friction levels. Threshold load and friction increase are shifted to higher normal

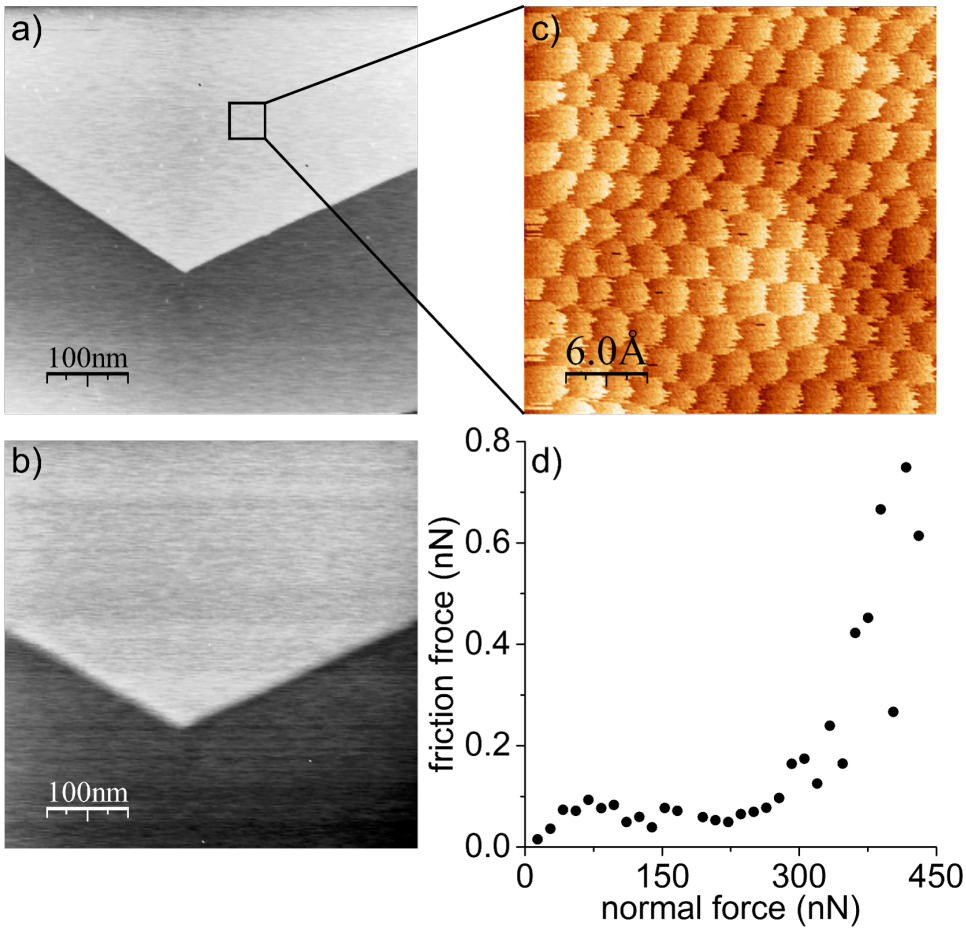

Figure 4.2: Topography of epitaxial graphene on SiC(0001): a) and b) are AFM images recorded in non-contact mode before and after the experiment; c) is a lateral signal image of the superstructure of epitaxial graphene on SiC(0001) recorded during experiment in square area marked in a); d) is a plot of results from experiment in a) with oxidized silicon tip; Data and images were prepared by Prof. Tobin Filleter and are part of publication, which is the basis of this chapter [1]

forces in repeated experiments with the same tip, suggesting that the sharpness of the tip and thus the effective contact pressure is reduced in experiments at high load. Atomistic simulations were performed to reveal the friction and deformation mechanisms underlying these observations (section 4.2). Based on the results of simulations, it will be discussed (section 4.3) that the graphene layer under high contact pressure transits from a sp^2 to sp^3 hybridization and forms covalent bonds with the SiO_x tip, which causes the increase in friction. At such high contact pressure, the oxide layer is plastically deformed, which leads to flattening of the tip.

4.1.2 Electric conductivity under high contact pressure

An electric conductivity of 2D materials is usually considered in the lateral in-plane direction. However, in this work, the normal-to-plane electric conductivity is investigated during the friction measurements. The experiments described above were additionally modified by the application of voltage bias. Friction force and electric current were recorded between oxidized silicon tip and epitaxial graphene on SiC(0001). Five series of measurements were conducted with 60 nm/s of sliding speed but with a different range of normal load and various values of voltage bias. These parameters were chosen to include the normal load range in which the

threshold load and transition to the high-friction regime can be observed. Differences in voltage bias were applied to ensure registration of all changes in electric current as a function of normal load. Parameter ranges are limited by the hardware, which can record electric current up to 50 nA. The results of the first and the fourth series are presented in figure 4.3 and illustrate general observations.

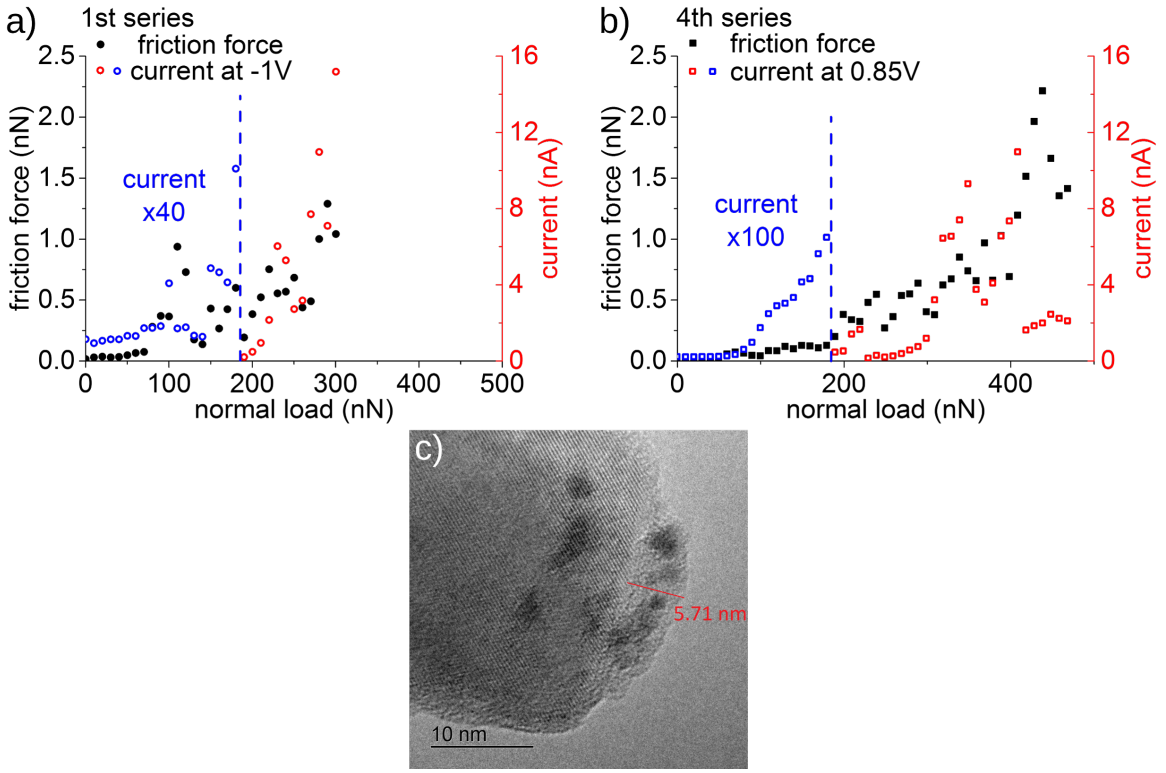

Figure 4.3: Friction force and electric current as a function of increasing applied normal load recorded between an oxidized silicon tip and epitaxial graphene on SiC(0001): results of a) 1st and b) 4th series of friction measurements with single tip; Slow increase in the electric current at low normal loads is highlighted with a multiplication factor; c) TEM image of the tip from experiments in a) and b).

For friction, previous observations are reproduced in both the first and the fourth series. In the first series (figure 4.3a)), the transition from ultra-low (μ= 0.000 037) to high friction regime occurs at 80 nN of normal load. Friction then increases with a large scatter and reaches a maximum of around 1.3 nN at 290 nN of normal load. In the fourth series (figure 4.3b)), the threshold load is at 200 nN, below which friction was increasing with coefficient μ = 0.000 75. The increase in friction is more significant above 200 nN of normal load and with a smaller scatter than in the first series. From 410 nN of normal load, the friction force increases even quicker and reaches the maximum of around 2.2 nN at 440 nN of normal load.

The value of the electric current in the first series (figure 4.3a)) remained around 0.03 nA until the normal load reached 150 nN when the current jumped to 0.1 nA and started slowly increasing. Electric current increases faster above 200 nN of the normal load. Two significant drops in current were recorded at 250 nN and 290 nN of normal load before it reached the maximum of around 15 nA at 300 nN of normal load. Similarly to friction, the conductivity is affected by the atomic configuration of the tip. The measured friction has a much larger scatter, than the electric current. Not overlapping scatter in friction and current suggests that the atomic reconfiguration of the tip may not always be attributed to both friction and current concurrently.

In the fourth series (figure 4.3b)), the voltage bias was lower and the current started to slowly increase from 70 nN of normal load. In a small range, the current increases faster from 190 nN, which overlaps with the transition threshold load at 200 nN, until it drops at 220 nN of normal load. The current increases faster again from 280 nN of normal load. Two significant drops in the current were recorded at 360 nN and just after reaching the maximum of 11 nA at 410 nN of load. Above 410 nN of normal load, the current varies around 2 nA until the end of the series without any significant increase. This final drop in the current occurs before the maximum and the final drop in the friction. This order of events and significant permanent decrease in current suggests that mechanism other than only atomic reconfiguration starts to dominate the conductivity.

These experiments demonstrate the increase in the electric current with increasing normal load and the drops in the conductivity related to high contact pressure applied to the SiO_x tip. Figure 4.3c) shows the TEM image recorded after this fourth run and reveals an apex oxide layer of 5.7- nm thickness and an estimated radius of 5–10 nm. The influence of graphene transition from the sp^2 to sp^3 hybridization and deformation of SiO_x will be considered in the discussion (section 4.3) as the main factors changing the conductivity.

4.1.3 Nanoscale friction between the diamond and the graphene on SiC

Friction on epitaxial graphene was also tested with diamond tips. The choice of the tip was motivated by the hardness of the diamond, its resistance to wear and the comparison of experimental results obtained with diamond tips and presented above SiO_x tips. Two different types of cantilevers were used: ADAMA AD-2.8-AS with a monocrystalline diamond tip and DT-FMR with a polycrystalline diamond coating on the tip.

The analysis of the evolution of the stick-slip pattern gives access to a more detailed understanding of the friction phenomenon. Figure 4.4 includes lateral signal maps with the most distinct stick-slip motion pattern respectively for the SiO_x and the monocrystalline diamond tip. The profiles of images with distinct stick-slip motion are characterized by periodic almost perfect saw-tooth pattern with high amplitude-to-noise ratio. Friction maps measured with SiO_x tips have a low amplitude-to-noise ratio, which may prevent the identification of the stick-slip pattern at low normal loads. The amplitude-to-noise ratio increases with increasing normal load, due to an increase of the amplitude of the lateral signal. Graphene can be identified by the periodicity of the stick-slip, which should be identical or almost identical to that of the graphene lattice. Friction maps measured with SiO_x tips rarely have such distinct stick-slip pattern as in figure 4.4a), which often require increased normal load. Therefore, an analysis of the evolution of the stick-slip is difficult for SiO_x tips. figure 4.4b)

Friction maps measured with monocrystalline diamond tips have a much higher amplitude-to-noise ratio (figure 4.4b)), than those measured with SiO_x tips. For the SiO_x tip, the lateral signal amplitude varies from 10 to 15 mV with slight noise (figure 4.4a)), whereas this for the monocrystalline diamond tip varies from 20 to 38 mV with almost no noise (figure 4.4b)). This difference in amplitude-to-noise ratio between SiO_x and diamond tips might be the result of the amorphous structure of SiO_x, which causes more noise in the lateral signal. For the monocrystalline diamond tip, the stick-slip pattern can be identified already at 0 nN normal

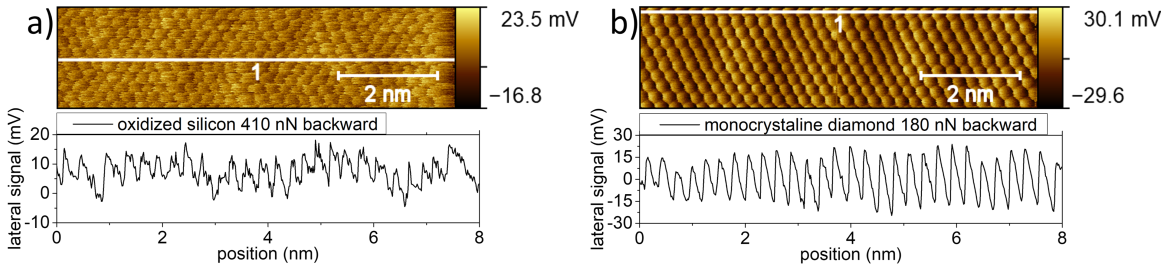

Figure 4.4: High-resolution friction maps recorded with a) SiO_x and b) diamond tip on epitaxial graphene on SiC(0001).

load and becomes more distinct with increasing normal load. The graphene lattice can be identified in most of the recorded friction maps. This allows to analyze the evolution of the stick-slip pattern as a function of normal load for monocrystalline diamond tips.

The results of the first experiment with the diamond tip show similarities and differences to those obtained with SiO_x tips. The friction force is initially ultra-low and increases linearly with increasing normal load and the friction coefficient $\mu = 0.000\,29$ (figure 4.5a)). From 230 nN of normal load, the increase of friction is much faster as friction transits to the high-friction regime. However, at 350 nN of load, the friction jumps to a value 21 times higher. This jump in the friction force is exceptional as no such jump was recorded with SiO_x tips, for which the measured friction does not exceeded 3 nN. As the normal load increases further, the friction force varies between 5 and 10 nN (figure 4.5b)).

The evolution of the stick-slip pattern in the function of the normal load was analyzed only for the first experiment when the tip was the sharpest. To immediately profit from the sharpness of the monocrystalline diamond tip the first experiment was performed without a period of waiting for the thermal equilibrium of the experimental setup, which resulted in the presence of a significant thermal drift. The hexagonal graphene lattice recorded in this experiment is distorted into stripes by thermal drift and can be identified only by the stick-slip periodicity in a profile. The stick-slip pattern appears at 0 nN normal load (figure 4.5c)). Increasing the normal load improves the amplitude-to-noise ratio of the stick-slip and causes changes into different patterns. The observed patterns can be assigned to five ranges of normal load at which they occur continuously. The transition between each range is most probably caused by the change in the atomic configuration of the tip due to increasing contact pressure. Only in the range V the forward and backward signals do not overlap and form a clear friction loop. Therefore, for better readability, all profiles of friction maps except for the range V have only a backward signal.

In the range I up to 144 nN of normal load, the pattern consists of stripes formed as a result of the distinct stick-slip and the drift. The amplitude of the stick-slip increases with increasing normal load (figures 4.5c-e)). Between 144 nN and 163 nN of normal load in range II, the stick-slip pattern is distorted and the amplitude is lower (figure 4.5f)). In the range III from 163 nN to 284 nN of normal load, the stick-slip is distinct again and has increased amplitude. The drift and/or a constant reconfiguration of the tip is so strong that every line of the scan is shifted with respect to the previous line (figure 4.5g)). Figure 4.5h) presents a typical pattern for the range IV from 284 nN to 342 nN of normal load. Two stick-slip patterns with different periodicity are observed interfering with each other, which additionally increases the amplitude.

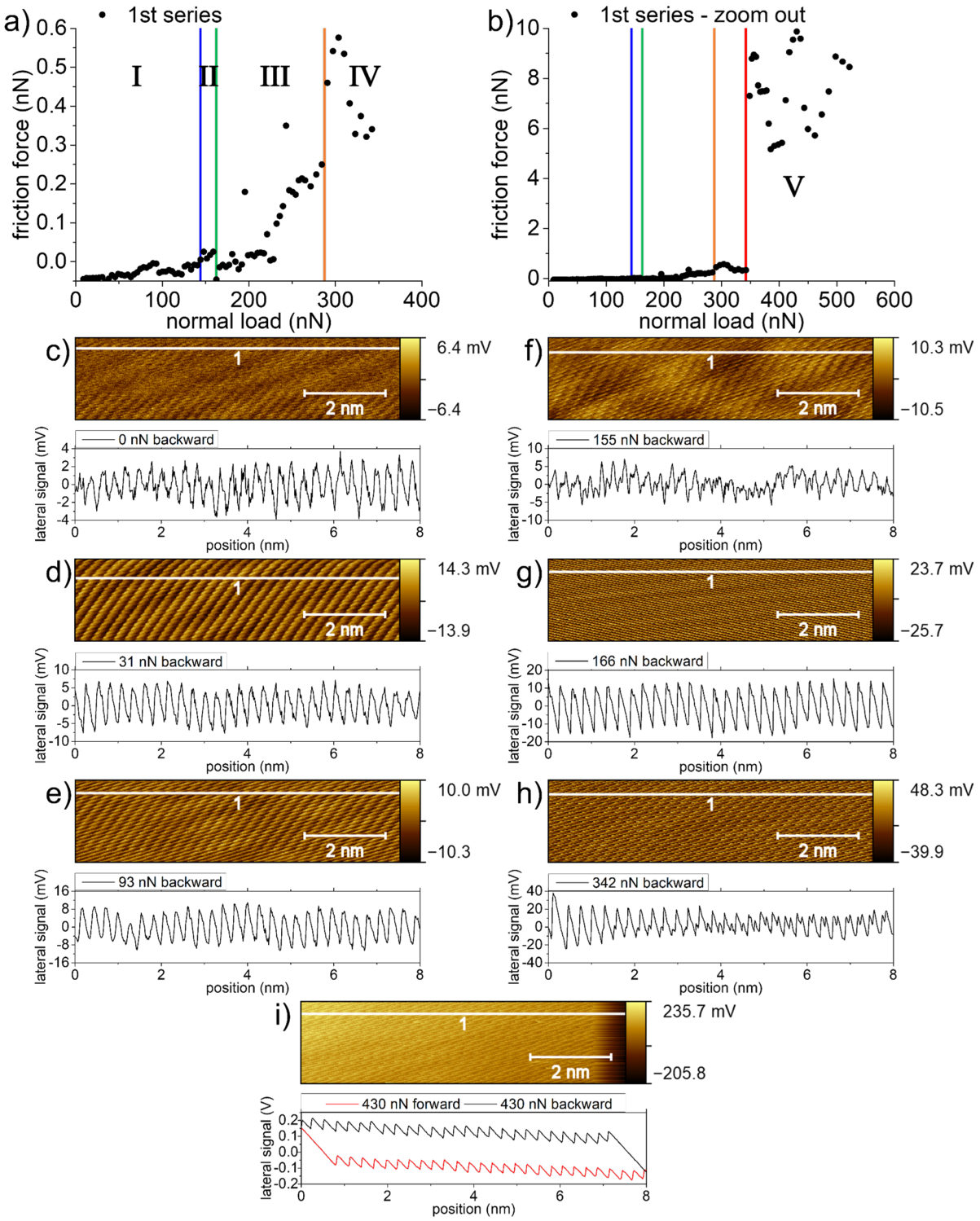

Figure 4.5: The first friction experiment with a monocrystalline diamond tip on epitaxial graphene on SiC(0001): a) friction force as a function of increasing normal load; b) zoom out of a); evolution of stick-slip patterns: c) to e) from range I; f) from range II; g) from range III; h) from range IV; i) from range V.

From 350 nN of normal load in the range V, the friction loop is clearly observable with the highest amplitude (1 slip is ≈60 mV) of the stick-slip pattern (figure 4.5i)).

Subsequent experiments with the same monocrystalline diamond tip and various sliding speeds demonstrate different evolutions of the friction vs. normal load curves (figure 4.6a)).

Each series begins with a linear increase in friction force with ultra-low coefficients of friction, which are listed in table 4.1. From the second to fourth series, the transition normal load threshold to the higher friction regime for each series is recorded for different normal loads (table 4.1). For the second and fourth series, the plateau of elevated friction was observed, before the rapid increase in friction at higher normal loads. With each subsequent experiment, the highest recorded friction force is decreasing. After reaching the maximum value, the friction drops significantly both in the third and the fourth series. In the fifth series, the transition

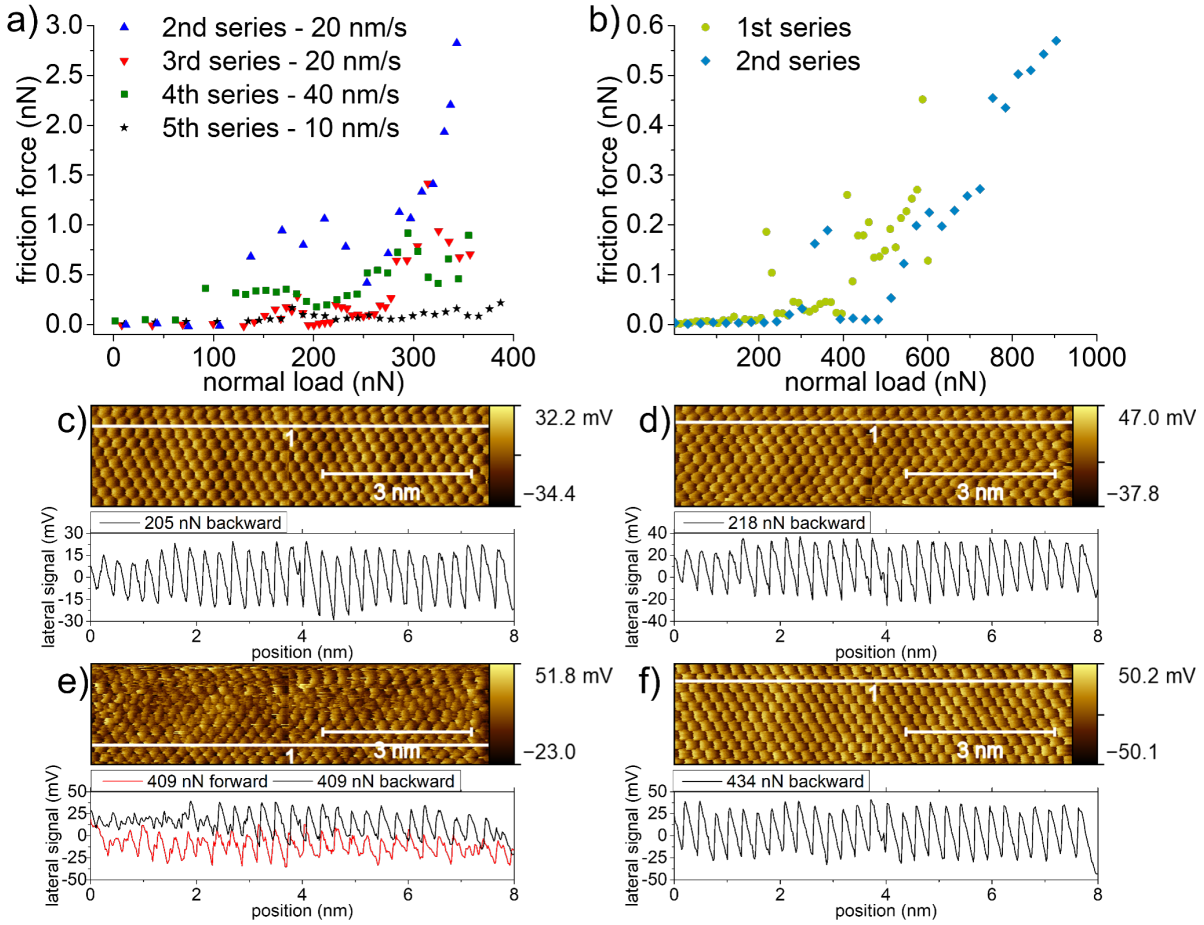

Figure 4.6: Friction force as a function of increasing normal load between a monocrystalline diamond tip and epitaxial graphene on SiC(0001): a) series of measurements with the tip from figure 4.5 and different sliding speeds; b) two experimental series with another monocrystalline diamond tip; c) to f) stick-slip patterns recorded during first series from b).

normal load threshold to the high friction regime is not reached and linear ultra-low friction remains without significant changes until the end of the series. After these experiments, SEM images of the tip were taken (figure 3.9c)).

Two series of experiments with a second cantilever of the same type with the monocrystalline diamond tip were conducted to confirm previous observations (figure 4.6b)). Both series were recorded with the constant sliding speed of 60 nm/s. The linear increase of ultra-low friction with the lowest coefficients of friction in this work was measured at low normal loads in both series (table 4.1). At some normal loads in both series, sudden jumps or rapid increases in the friction force were recorded, followed by drops to lower or even initial ultra-low friction. The transition normal load threshold is higher than for the most of experiments with SiO_x and

Table 4.1: Transition normal load thresholds and coefficients of friction for silicon oxide (PPP-ContR) and diamond tips (ADAMA, DT-FMR); Smooth transition with difficult to determine normal load threshold is marked by an asterisk.

cantilever	PPP-ContR			ADAMA AD-2.8-AS		DT-FMR
tip's number	1^{st}	2^{nd}	3^{rd}	1^{st}	2^{nd}	1^{st}
	transition normal load threshold [nN]					
series 1	60	100	80	230	409	310
series 2	50	110*	110$*$	140	510	570
series 3	110		170	260		
series 4	80*		200	90		
series 5	100		130*	not reached		
	ultra-low friction regime coefficient of friction μ [10^{-3}]					
series 1	0.94 ± 0.65	1.6 ± 0.4	0.75 ± 0.13	0.29 ± 0.03	0.046 ± 0.012	1.5 ± 0.3
series 2	-0.06 ± 0.38	2.4 ± 0.5	0.79 ± 0.14	-0.17 ± 0.17	0.013 ± 0.005	0.74 ± 0.11
series 3	0.49 ± 0.16		0.34 ± 0.08	0.13 ± 0.14		
series 4	2.0 ± 0.5		0.75 ± 0.07	0.14 ± 0.16		
series 5	0.34 ± 0.19		0.85 ± 0.1	0.36 ± 0.07		

diamond tips and is increasing with the consecutive series (table 4.1). Maximum friction forces recorded in both series with the second monocrystalline diamond tip are lower than 0.6 nN and are the lowest among all experiments where the transition to higher friction occurred.

The first series with the second monocrystalline diamond tip exhibited a more stable state of the tip and only incidental changes in the stick-slip pattern. Most of the friction maps in the first series were similar to figure 4.6c) where clear hexagonal graphene lattice is modulated by a moiré pattern and distinct stick-slip were recorded. The increased friction at 218 nN of normal load does not affect the stick-slip pattern (figure 4.6d)). Another friction increase at 409 nN is accompanied by distortion of stick-slip and image of graphene lattice (figure 4.6e)). At 434 nN of normal load, the friction map of the hexagonal lattice turned into a map of squares ordered hexagonally (figure 4.6f)). This pattern was observed more often in the second series of measurements.

While no damage to the graphene surface was observed for SiO_x and monocrystalline diamond tips, the graphene layer was ruptured on two occasions with the DT-FMR polycrystalline diamond tip. Results of the experiment with the observation of the first rupture of graphene are collected in figure 4.7. Initially, the friction increases linearly with coefficient μ_{before} = 0.001 5 (figure 4.7a)). The transition to the high friction regime occurs at 315 nN of normal load and the rapidly increasing friction reaches the maximum of 2.8 nN just before the rupture at 400 nN of normal load.

The rupture of graphene occurred during the same scan at 400 nN of normal load and the friction jumped to 45.8 nN (figure 4.7b)). This 16.4 times higher friction value is from a completely different range than any friction value described so far. During the decrease of normal load, the friction decreases linearly with almost 40 times higher coefficient μ_{after} = 0.06. Until the rupture, the graphene/SiC superlattice can be observed. However, the friction loop

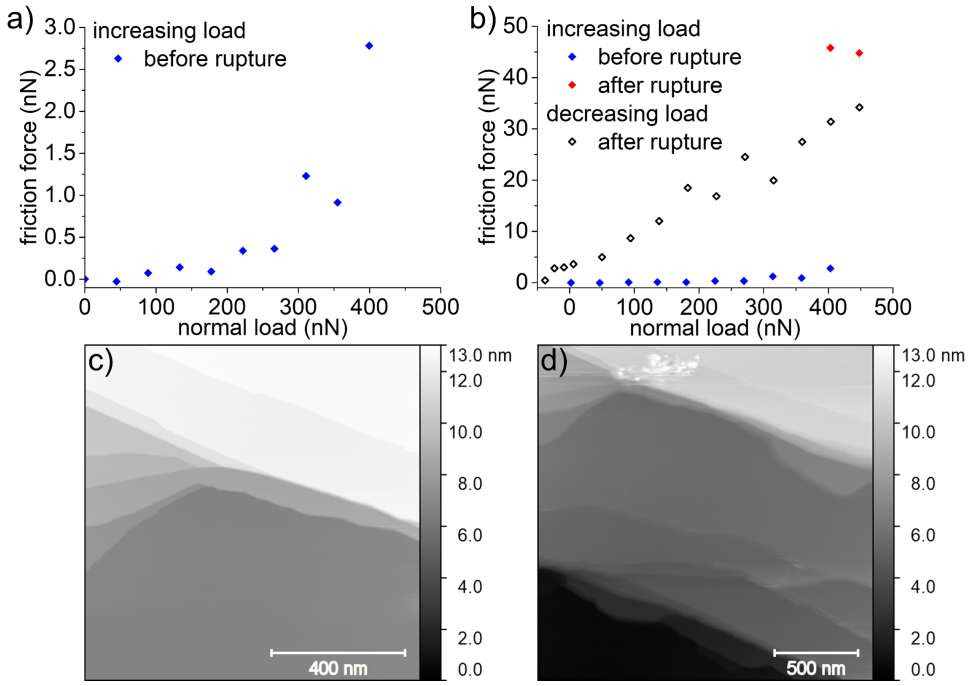

Figure 4.7: The first rupture of epitaxial graphene on SiC(0001) with a polycrystalline diamond tip: friction force as a function of increasing normal load a) before rupture of graphene layer; b) before and after rupture of graphene layer; topography c) before and d) after the experiment in a) and b).

changes completely after the rupture (see figure A1 in Appendix II). The rupture of graphene changed topography, which is illustrated in images before (figure 4.7c)) and after (figure 4.7d)) the experiment.

The same tip was used to repeat this experiment in another place on this sample (figure 4.8). The normal load was increased until the point when the rupture of graphene was registered. From the beginning, the friction is slightly higher in this initial stage than this during the first experiment (figure 4.8a)), but increases linearly with a lower coefficient (table 4.1). After the transition to the high friction regime, the friction force was increasing rapidly with some jumps and drops until 1060 nN of normal load when the graphene was ruptured. The friction force before rupture reached 6.46 nN at this normal load. After rupture the friction force jumps to 53.8 nN (figure 4.8b)), the value almost 10 times higher than before rupture and the highest recorded in this work. Change in the friction loop is recorded similarly as in the first experiments (see figure A1 in Appendix II). Although the graphene after rupture was recorded only in the last scan, the topography has changed (figures 4.8c) and 4.8d)).

The experiments on the epitaxial graphene on SiC(0001) with diamond tips demonstrate ultra-low friction, even lower than that measured with SiO_x tips. However, this ultra-low friction is limited to a certain load threshold, where the transition to the high friction regime occurs, similarly to the SiO_x tips. Only with polycrystalline diamond tips, it was possible to rupture the monolayer graphene and register a concurrent jump to 16 times higher friction. Similarly to SiO_x tips, the threshold load and friction increase are shifted to higher normal forces in repeated experiments with the same diamond tip. The stick-slip pattern changes into multiple different patterns depending on the normal load and effects of the drift. It indicates that plastic deformations occur also on the surface of the diamond tips. This makes experiments

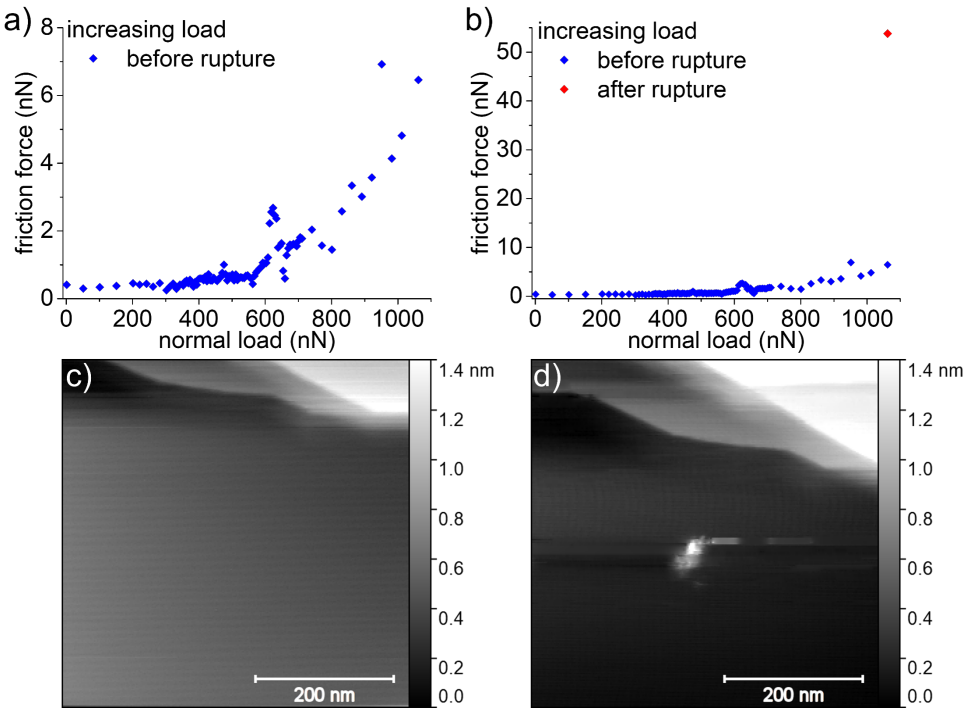

Figure 4.8: The first rupture of epitaxial graphene on SiC(0001) with a polycrystalline diamond tip: friction force as a function of increasing normal load a) before rupture of graphene layer; b) before and after rupture of graphene layer; topography c) before and d) after the experiment in a) and b)

difficult to reproduce and to design studies for varying parameters such as sliding speed.

4.2 Simulation results

The sliding contact between silicon oxide and the epitaxial graphene layer on SiC(0001) was modeled in a quantum-mechanical molecular dynamics simulation based on a self-consistent charge density-functional tight-binding [DFTB] method [105]. The simulation allows to describe pressure- and shear-induced plastic events and resulting structural changes at the tribological interface. The two surfaces were approached to a preset normal pressure and the shear stress across the interface was evaluated during sliding. The simulation setup and a summary of results are provided in figure 4.9. To account for variability in the amorphous structure of the silicon oxide, five different structural configurations were implemented for comparison and averaging. Surface dangling bonds on silicon and oxygen atoms were passivated by adding hydroxyl groups and hydrogen atoms, respectively. The reliability of DFTB was tested by simulating selected trajectories with first-principles density-functional theory. The results are the same in terms of transition pressure and numbers for shear stress (see figure A2 in Appendix II).

Figure 4.9a) presents snapshots for one configuration sliding at contact pressures of 1, 10, and 15 GPa. With increasing pressure, the silicon oxide and the graphene-SiC(0001) are compressed. Chemical bonds form between carbon atoms of the graphene layer and the underlying carbon interface layer on the SiC(0001) surface, but also between carbon atoms of the graphene layer and oxygen or silicon atoms of the oxide surface. Analysis of the bond formation reveals a preferred local tetragonal sp^3 hybridization, i.e., that nearest-neighbor carbons in the graphene

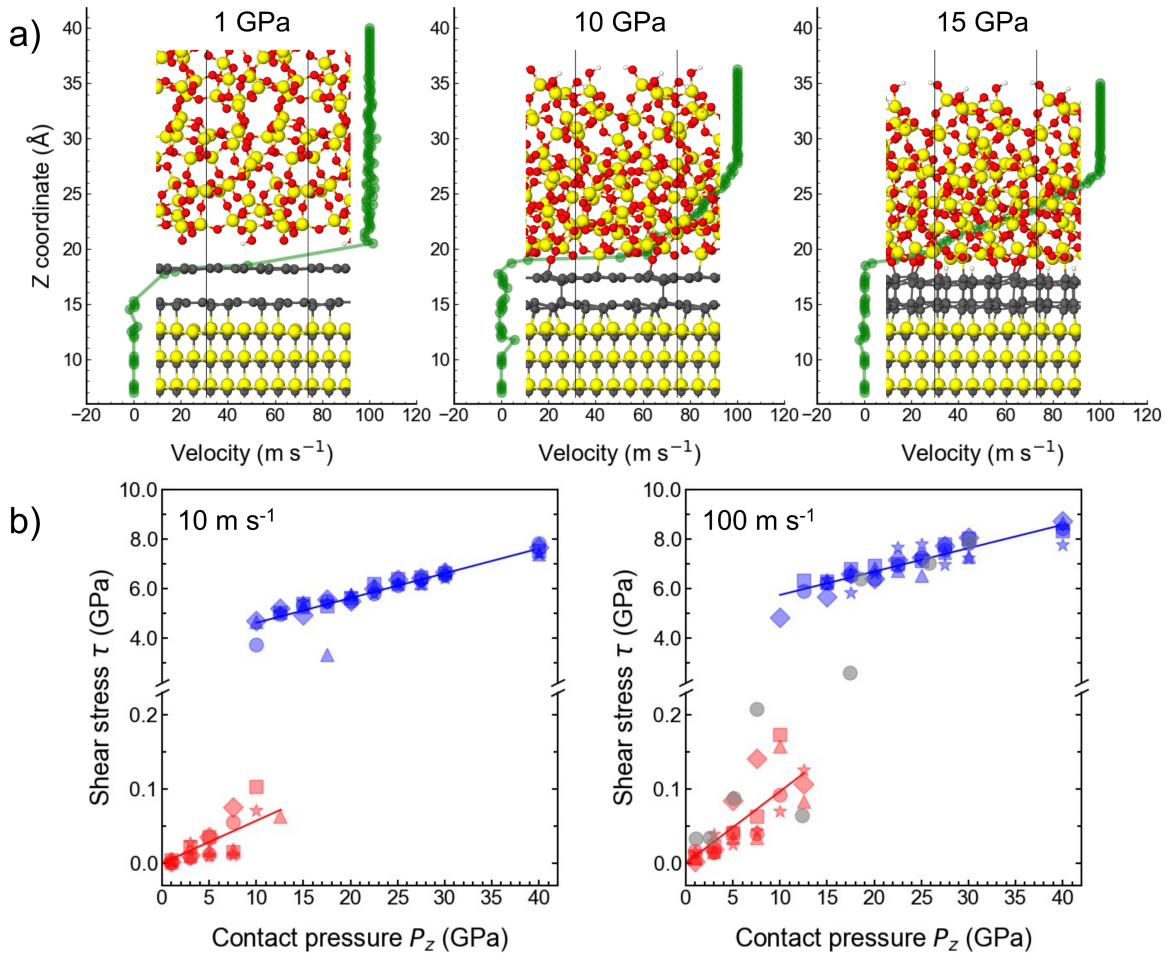

Figure 4.9: Simulation setup and a summary of simulation results: a) Simulation setup of silicon carbide with graphitic interface layer, graphene, and one of five amorphous silicon oxide configurations. Colors signify silicon (yellow), oxygen (red), carbon (gray), and hydrogen (white); sticks between balls indicate a chemical bond. Snapshots are taken from the middle of the 0.3- ns simulation period for a contact pressure of 1, 10, and 15 GPa (temperature T = 300 K and sliding velocity v = 100 m/s). Green data points report the sliding velocity as function of the normal coordinate and indicate the location of the shear plane; b) Simulated shear stress vs contact pressure for five different silicon oxide configurations which are represented by different symbols. Red symbols indicate absence of chemical bonds between graphene and silicon oxide atoms; blues symbols indicate the formation of at least one such chemical bond between a carbon atom and a silicon or oxygen atom (temperature T = 300 K). Shear stress is calculated for the last 10% of 3- ns simulated sliding time at 10 m/s and of 0.3- ns sliding time at 100 m/s. The figure is adopted from Ref.[1].

layer bind to the carbon interface layer below and to silicon or oxygen above, respectively. Singular C-Si bonds without corresponding C-C bonds of nearest neighbors are observed only for undercoordinated, reactive Si atoms at the oxide surface (see figure A3 in Appendix II).

Figure 4.9a) also shows the velocity profile of atoms across the simulation cell and thus indicates the shear plane. For a pressure of 1 GPa, the graphene layer slides on the supporting SiC with roughly 20% of the silicon oxide velocity. When C-C bonds between graphene and SiC have formed at 10- GPa pressure, the graphene completely rests with the SiC substrate and the shear plane is entirely between graphene and silicon oxide. At a pressure of 15 GPa, the shear is accommodated by deformation of the silicon oxide into a depth of 1 nm.

Values for the shear stress are summarized in figure 4.9b) for simulations of all five silicon oxide configurations and for two different sliding velocities. For contact pressures up to 10 GPa,

a very low shear stress is observed with an average coefficient of shear stress divided by normal stress of 0.01. A steplike increase in shear stress by a factor of 50 is observed at a critical contact pressure between 10 and 13 GPa. All silicon oxide configurations are in the high-friction state for contact pressure of 15 GPa and higher. The transition occurs at 10.1 GPa for the lower simulated sliding speed of 10 m/s, compared to 12.7 GPa the higher sliding speed of 100 m/s (see figure A5 in Appendix II). Simulations at the sliding speed of 100 m/s for higher temperatures were also performed and the transition pressure shifts from 12.7 to 10 GPa at higher temperature was found (see figures A6 and A7 in Appendix II). Overall, the simulation results let us expect a transition pressure of about 10 GPa for lower velocities. Please note that the system may show fluctuations between the low-friction and the high-friction state at the transition. For both sliding velocities one silicon oxide configuration in the low-friction state can be found in figure 4.9b) at a contact pressure of 12.5 GPa after having exhibited high friction at 10 GPa.

The steplike increase in shear stress is directly related to the formation of chemical bonds between the graphene layer and oxygen or silicon atoms of the silicon oxide, as analyzed in the figure 4.10. The shear stress increases with the number of chemical bonds between graphene and silicon oxide. Please note that the shear stress remains close to zero, although, the bonds between graphene and SiC are observed, while it increases significantly as soon as bonds between graphene and silicon oxide are formed. A strong correlation between shear stress and the number of bonds across the graphene-silicon oxide interface is also found in their respective fluctuations within simulated trajectories, while there is no correlation between the fluctuations in the number of graphene-SiC bonds and the shear stress.

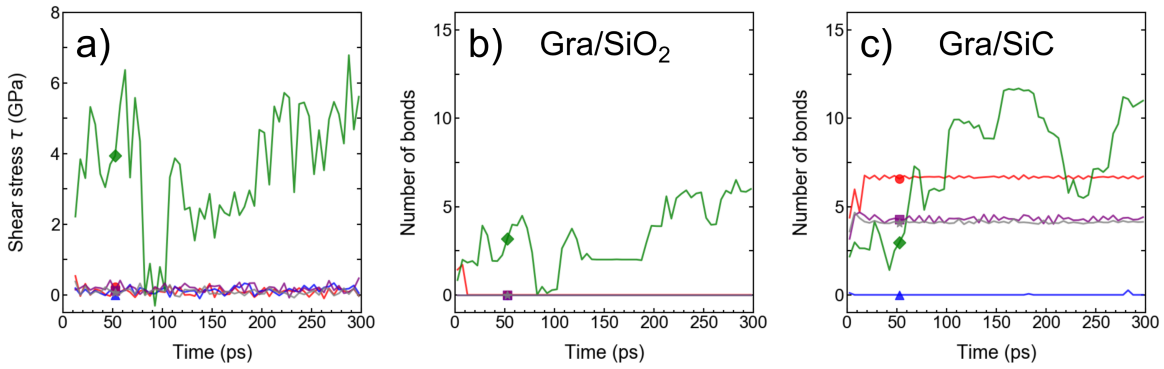

Figure 4.10: Correlation of shear stress with number of C-Si and C-O bonds: a) Shear stress as function of simulated time for five different silicon oxide configurations (300 K, 100 m/s, 10 GPa); b) Number of bonds between graphene and silicon oxide for the same simulations; c) Number of C-C bonds between graphene and carbon interface layer on a SiC(0001) surface for the same simulation; Note the strong correlation between shear stress and number of carbon-silicon oxide bonds, and the weak correlation with the C-C bonds. The symbols are the same as in figure 4.9. The figure is adopted from Ref.[1].

The compression of the system under increasing pressure reduces the distance between graphene and SiC and between graphene and silicon oxide and thus is the origin of bond formation. Starting from a pressure of 7.5 GPa, also an increase of bonds within the silicon oxide is observed and, consequently, an increase in the number of overcoordinated silicon and oxygen atoms. For the contacting surface, the plastic events in the silicon oxide result in a densification and in an overcoordination of silicon and oxygen atoms, but not in the formation of reactive species at the surface. With increasing pressure, transfer of passivating hydrogen or of oxygen to the graphene or along the surface can open bonds for reaction with the graphene. At contact

pressures above 12.5 GPa, the formation of a high density of chemical bonds with graphene leads to a shift of the shear plane into the silicon oxide, when the amorphous structure becomes the weakest part of the system.

4.3 Discussion

4.3.1 Comparison of experiments and simulations

Experimental results and tight-binding simulations reveal that the outstanding lubrication by epitaxial graphene is limited by a threshold load, above which the formation and rupture of covalent out-of-plane bonds between graphene and the sliding oxide tip causes strong friction. Experimental observations will be related to simulation findings to reveal the mechanisms underlying the transition to the high friction regime.

The most prominent observation is a steplike increase of friction force by a factor of 10 in AFM experiments and of shear stress by a factor of 50 in simulations. The threshold normal force in AFM experiments for entering the high-friction regime is about F_N = 100 nN. The corresponding maximum contact pressure in the Hertz model can be estimated as

$$p_0 = \frac{1}{\pi}\left(\frac{6F_N E_{eff}^2}{r^2}\right)^{\frac{1}{3}} with \frac{1}{E_{eff}^2} = \frac{1-\nu_{6H-SiC}^2}{E_{6H-SiC}} + \frac{1-\nu_{SiO_2}^2}{E_{SiO_2}} \tag{4.1}$$

With E_{SiO_2}= 75 GPa, E_{6H-SiC} = 400 GPa [87], ν_{SiO_2} = 0.18, ν_{6H-SiC} = 0.16, and thus E_{eff} = 65.2 GPa, the threshold contact pressure is p_0 = 14.9 GPa for a tip radius of r = 5 nm and is p_0 = 9.4 GPa for a tip radius of r = 10 nm. With these tip radii, estimated from the TEM images in figures 4.1 and 4.3, the range of transition pressures includes the threshold predicted by the simulations of p = 10 GPa.

On atomic scale, the contact pressure is expected to exhibit large fluctuations for an amorphous tip pressing against a flat surface [111]. The transition may thus occur even at lower normal forces than expected for a given tip radius. On the other hand, a contact pressure of 12.5 GPa reaches the expected yield strength of silicon oxide, even in nanometer-scale structures [112, 113]. The increase in transition force in repeated experiments indicates that sharp asperities at the tip apex, which produce the pressure necessary for bonding, are flattened by plastic deformation. This picture is supported by the simulations, which register plastic events and a densification of silicon oxide for pressures exceeding 7.5 GPa. Covalent bond formation at sharp asperities and plastic deformation of these asperities contribute to the irregularity in the evolution of the high-friction regime in simulations and in the experiments. Details of the evolution in the transition regime depend critically on the atomic configuration of the amorphous tip, as reflected in experiments with different tips and in the simulations for different silicon oxide configurations. Only when the contact pressure exceeds 15 GPa, the simulated shear stress becomes comparable for all silicon oxide configurations. In this high-pressure regime, the shear plane shifts from the graphene-silicon oxide interface into the silicon oxide. It is suggested that this regime is not accessible in AFM experiments due to expected plastic yield of the sharp tip.

4.3.2 Mechanism of nanoscale high-friction regime for SiO_x tips

The simulations reveal the atomistic mechanics underlying the high-friction regime. Friction is caused by the formation of out-of-plane bonds between the graphene on the surface and silicon or oxygen atoms of the tip, the buildup of elastic energy when stretching the bonds and deforming their environment, and the fast release of the energy when the bonds rupture. The formation of these friction-related bonds is supported by additional mechanisms which are activated by the increasing contact pressure. Elastic and plastic deformation of the silicon oxide leads to a densification at the interface and thus to an increase in available binding partners. High contact pressure also initiates out-of-plane bonds between carbon atoms in the graphene layer and the carbon termination of the SiC(0001) substrate. Carbon-oxygen and carbon-silicon bonds form next to these carbon-carbon bonds and thus establish a local sp^3 configuration. The rehybridization of bilayer graphene under compression and its implications have previously been studied by simulation and in experiments. Barboza *et al.* predicted the formation of a hydroxylated diamond layer under compression and complemented this simulation results with experiments indicating the inhibition of electrical charge injection into the diamondlike materials [53]. Gao *et al.* reported a diamondlike hardness and reduced electrical conductivity for bilayer graphene on SiC(0001) under pressure, with corresponding findings in density-functional theory calculations [87]. An atomic-scale manifestation of pressure induced hybridization in graphene-SiC(0001) was detected by high-resolution force microscopy with a single-molecule tip [89]. These reports and presented in this work results describe a mutual stabilization of C-C bonds between the graphene layers and bonds out of the bilayer involving nearest neighbors of C-C bonded carbon. It is however important to note that neither the densification of the silicon oxide nor the formation of carbon-carbon bonds alone leads to increased friction. The high-friction regime is directly related to the formation of carbon-silicon and carbon-oxygen bonds.

A quantitative comparison of simulated shear stress and measured friction force requires a contact mechanics and a friction model. The simplest approach is to integrate the simulated shear stress over the contact area using the contact pressure distribution predicted by the Hertz model. The calculated friction force is by a factor of 3–4 higher than measured in the low-friction regime and by orders of magnitude higher in the high friction regime, reaching values of F_L = 50 nN for normal forces of F_N = 200 nN (see figure A10 in Appendix II). Such discrepancies can be expected because of three differences between experiment and simulation (see Appendix II for detailed discussion). First, the sliding velocity is orders of magnitude lower in the experiment, impeding direct comparison of molecular dynamics and friction-force microscopy [114]. Second, the AFM tips experience flattening due to plastic deformation lowering the contact pressure and thus friction. Third, the predicted shear stress in the high-friction regime depends critically on the yield stress of the tip-apex material, which decreases with decreasing silica density and increasing hydrogen contents [115], parameters which are not know for the microfabricated AFM tip.

4.3.3 Contact pressure modulation of electric conductivity

The electric current measured in this study is a tunneling current. It is strongly dependent on the configuration of the insulating silicon oxide surface of the tip, which modulates the barrier potential. The tunneling current measured in this study for the tip with the 5.7 nm thick silicon oxide surface increases with increasing normal load. This increase is attributed not only to a variation of the contact area but also to a decrease of the barrier potential as a result of the densification of silicon oxide. When the contact pressure reaches a certain critical value, the tunneling current drops. At this pressure, three mechanisms, which cause a decrease in the current, are observed: the reconfiguration of the silicon oxide tip, the rehybridization of graphene from sp^2 to sp^3, and plastic deformations of the tip. Depending on contact pressure, these three mechanisms may occur and influence the current simultaneously or separately, which is difficult to determine. The reconfiguration of the silicon oxide tip results in atomic configurations, which increase or decrease electric conductivity. The rehybridization of graphene from sp^2 to sp^3 leads to the formation of diamene and the reduction of electric conductivity [87]. The graphene rehybridization occurs locally and spontaneously due to constant reconfiguration of the silicon oxide, which can cause sudden changes in conductivity for each line if not each point of the scans. These fluctuations lead to large scatter of current value during each scan as well as jumps and drops in average current value per scan. Plastic deformations of the silicon oxide tip cause drastic changes in the atomic configuration and the contact area with the sample.

The last drop in current registered in figure 4.3b) occurs while friction force increases before reaching the maximum. The drop in friction is caused by plastic deformation of the tip at critical normal load and a drop in the contact pressure. Although the plastic deformation occurs, the already decreased current does not change significantly. As it was explained before, the friction force is influenced by the amount of covalent C-C bonds, which depends on the contact pressure. The order at which current and friction dropped indicates the possibility that the amount of covalent C-C bonds per contact area reached a critical value for the tunneling current to drop before the plastic deformation occurs. The drop in contact pressure caused by the plastic deformation was not large enough for the amount of covalent C-C bonds to decrease below the critical value, and no significant increase in the tunneling current was observed. The friction force after the plastic deformation did not decrease below its value from before the final current drop, which supports this explanation. An alternative explanation of this final drop in the current is the continues tip surface deformations. As it is difficult to determine experimentally, which mechanism dominates, a further investigation of this aspect is required.

The tunneling current is not decreased to 0 A, because not entire contact area between the tip and the sample experiences the same contact pressure. The periphery of the contact area induces contact pressure low enough so that rehybridization does not occur and conductivity is not lowered.

4.3.4 Comparison of nanoscale friction results for SiO_x and diamond tips

Findings for friction between diamond tips and graphene layer are in very good correspondence with experiments conducted with SiO_x tips on the same sample. The overall friction force is lower and starts with the coefficient of friction as low as $\mu = 0.000\,013$. Similarly, to

observations for SiO_x tips, the nanoscale friction transits to the high friction force regime when the contact pressure threshold is reached, and drops because of the deformation of the tip. It is suggested that the contact pressure needed to initiate the deformation of the crystalline diamond is not reached during these experiments. It is rather suggested that the surface structure of the diamond tips requires lower pressure to deform. It is expected that diamond tips are covered with a thin layer of amorphous and hydrogenated carbon, which may also contain some aromatic groups [116]. Such a passivated surface would have weak interactions with graphene and explain the lowered friction observed in experiments. Constant changes in the configuration of the surface of diamond tips during experiments are then responsible for the scatter of friction forces as function of normal load, similarly to SiO_x tips.

The influence of the atomic configuration of the tip on friction can be analyzed by the evolution of the stick-slip pattern with increasing normal load. The stick-slip pattern measured with SiO_x tips has a lower amplitude-to-noise ratio, than this measured with diamond tips. It is suggested that the amorphous character of SiO_x results in a more irregular atomic configuration and easier reconfiguration than the diamond's surface. The proportion of elastic deformations of the tip's surface to stick-slip motion on epitaxial graphene as a mechanism of energy dissipation is higher for the irregular SiO_x than diamond tips. This proportion results in a lower amplitude-to-noise ratio for SiO_x tips. The amplitude-to-noise ratio increases with increasing normal load as the result of the densification of silicon oxide and change in the proportion of energy dissipation mechanisms toward stick-slip motion. The energy dissipation for crystalline and stiffer diamond tips is based more heavily on stick-slip motion on epitaxial graphene. Therefore, the high amplitude-to-noise ratio is registered. The atomic reconfiguration of the tip may cause a change in the stick-slip pattern and result in: a decrease/increase in the amplitude-to-noise ratio (figure 4.5f) and g)), the appearance of additional stick-slip periodicity (figure 4.5h)) or distortion of the pattern (figure 4.6e)). The appearance of addition stick-slip periodicity can be explained by the formation of aromatic groups, which have a small rotation with respect to the graphene lattice, on a part of the diamond tip surface. Not every atomic reconfiguration of the tip's surface results in changes in the stick-slip pattern (figure 4.6c) and d)).

Based on the results listed in table 4.1, the transition normal load threshold varies between each series of all experiments, which can be explained by different starting atomic configurations of the tip. The transition normal load threshold of the last series of each experiment is higher than that of the first series, which proves the permanent deformation of both silicon oxide and diamond tips during experiments. The coefficient of friction in the ultra-low friction regime measured for silicon oxide tips is 0.002 4 or lower. The statistically lowest coefficient of friction was recorded for monocrystalline diamond tips with a range from 0.000 013 to 0.000 36.

4.3.5 Rupture of the graphene layer by the diamond tip

The shear plane moves to SiO_x as the softest material in the already rehybridized system of SiO_x/diamene/SiC(0001) at high contact pressure. After the formation of diamene between the diamond tip and the SiC(0001), the SiC becomes the softest part of the system [87]. At the critical contact pressure, the diamene can be picked up by the diamond tip due to affinity and similarity of structure and directly lead to rupture of the graphene layer. This results in the

penetration of the SiC(0001) substrate and the significant increase in friction. Such an increase in friction was observed experimentally in figures 4.7 and 4.8. The simulations of the sliding contact between the diamond tip and the epitaxial graphene layer on SiC(0001) are still being conducted by the group of Prof. Michael Moseler from the Fraunhofer Institute for Mechanics of Materials IWM in Freiburg. The epitaxial graphene on SiC(0001) was ruptured before in a macroscale study with a ruby sphere inside a tribometer [75, 76]. Although experiments were performed in a macroscale with a much higher normal load, the mechanism behind rupture might be similar to those considered in this work and related to the hardness of the tip. The ruby/corundum has a hardness of 9 in the Mohs scale, which is very close to the hardness of the diamond and allows to rupture the graphene. This is not the case for SiO_x, which has a hardness of 7 in the Mohs scale. The minimal hardness of the material is required to allow rupture of the monolayer epitaxial graphene on SiC(0001). Based on this study, the hardness should be above 7 in the Mohs scale. Determination of an exact value of that minimal hardness requires further investigation.

4.4 Conclusions

Limits of superlow friction, often classified as superlubricity, have been described before. In the framework of the Prandtl-Tomlinson model, elastic instabilities lead to friction on two-dimensional sheets where local deformations have to be considered [66]. In macroscale contacts, the high pressure under asperities leads to wear of graphene and concurrent increase in friction [117, 75]. In technological application, contacting surfaces have a finite roughness and the contact pressure at the apex of roughness asperities can be orders of magnitude higher than the nominal applied pressure. The results presented in this work results demonstrate that the intermittent formation of covalent bonds must be considered as an additional mechanism limiting the extraordinary lubrication by graphene at high contact pressure. On the other hand, the reversible switching between superlow and high-friction regimes opens opportunities to design micromechanical applications which require both low-friction sliding in contact and wearless slowdown functionality. Another possible application of the presented findings is tuning of the electric conductivity by contact pressure. The choice of silicon oxide counter face to monolayer graphene/SiC(0001) surface would increase the longevity of moving elements due to the deformation of silicon oxide in high contact pressure and preservation of the graphene layer. Diamond counter faces could be applied when lower friction is required but with the risk of damaging the graphene layer at critical contact pressure.

5 Nanoscale friction on van der Waals heterostructures of MoS_2 and graphene on SiC

This chapter covers research on van der Waals heterostructures of MoS_2 and graphene on SiC(0001) and contains material from the publication of Liu et al.[2] with additional unpublished material. The friction force and electric current as a function of normal load, electric bias and number of layers were determined for SiO_2 (PPP-ContR and PPP-FMR) probes. A diamond (ADAMA AS-2.8) probe was used to investigate the atomic lattice and appearance of the moiré pattern.

5.1 Experimental results

5.1.1 Atomic lattice of graphene and MoS_2

The CVD growth of MoS_2 on graphene/SiC(0001) resulted in a distribution of islands of varying height, ranging from single layers to four or more layers. Typical triangular monolayer MoS_2 islands are shown in figure 5.1. The edge of the triangle can have a length of up to 600 nm. The measured height of the island is 0.5 nm, a little less than expected based on

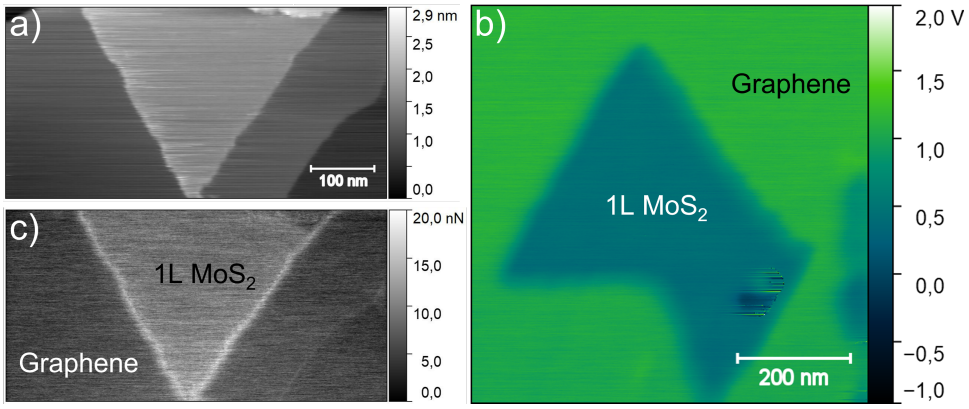

Figure 5.1: Characteristics of MoS_2 flake: a) topographic contact-mode AFM image of a monolayer triangular MoS_2 island grown on monolayer graphene/SiC(0001); b) friction force map recorded simultaneously with the data presented in a) at a load of 2.73 nN (scale is the same as in a)); c) CPD map recorded using the KPFM mode. The figure is adopted from Ref.[2].

chemical structure and reported previously [80, 118]. The simultaneously recorded friction force map shows higher friction on the MoS_2 island compared to the graphene/SiC(0001) substrate. The contact potential difference [CPD] between the tip and sample was determined as the bias voltage U_{CPD} at which the electrostatic tip-sample attraction is minimized. This measurement is performed in non-contact mode by Kelvin Probe Force Microscopy [KPFM] [77]. Based on the CPD map in figure 5.1c), the MoS_2 island has a lower work function than the graphene/SiC(0001). The shape of the flake in figure 5.1c) indicates that some flakes can connect to each other during growth and appear as a combination of multiple triangles.

Each flake has a cluster of unreacted material on top. It is expected that these clusters consist of a precursor material MoO_3 or MoS_2, which was not converted into MoS_2 island. It was not possible to establish a predictive model of growth. Different parameters used during preparations of samples of the MoS_2/graphene/SiC(0001) heterostructures cause differences in

the amount of MoS_2 islands, number of layers in each MoS_2 island, amount and size of clusters of unreacted MoO_3/MoS_2.

Friction maps with atomic stick-slip pattern (figure 5.2) reveal that the MoS_2 islands are aligned with the graphene substrate lattice. The periodicity of the stick-slip pattern for both surfaces (graphene: 276 pm; MoS_2: 348 pm; in figures 5.2a) and 5.2d)) is slightly larger than the theoretical value of the crystallographic lattice constant for both materials (graphene: 246 pm; MoS_2: 316 pm). This systematic error of around 10% is related to the inaccuracy of the piezoscanner. The difference in the stick-slip periodicity allows to distinguish both materials. The moiré pattern of the complex interface between reconstructed SiC(0001) and graphene (figure 5.2b))(see more in [79]) obscures any moiré pattern on monolayer MoS_2 (figure 5.2e)). The moiré pattern, which could be expected from the lattice mismatch between graphene and MoS_2, should have a periodicity of 1.1 nm. While the spatial frequency of the moiré pattern for the epitaxial graphene/SiC(0001) is well distinguished (figure 5.2c)), a broad distribution of shorter wave vectors is found for the MoS_2/graphene/SiC(0001) island (figure 5.2f)).

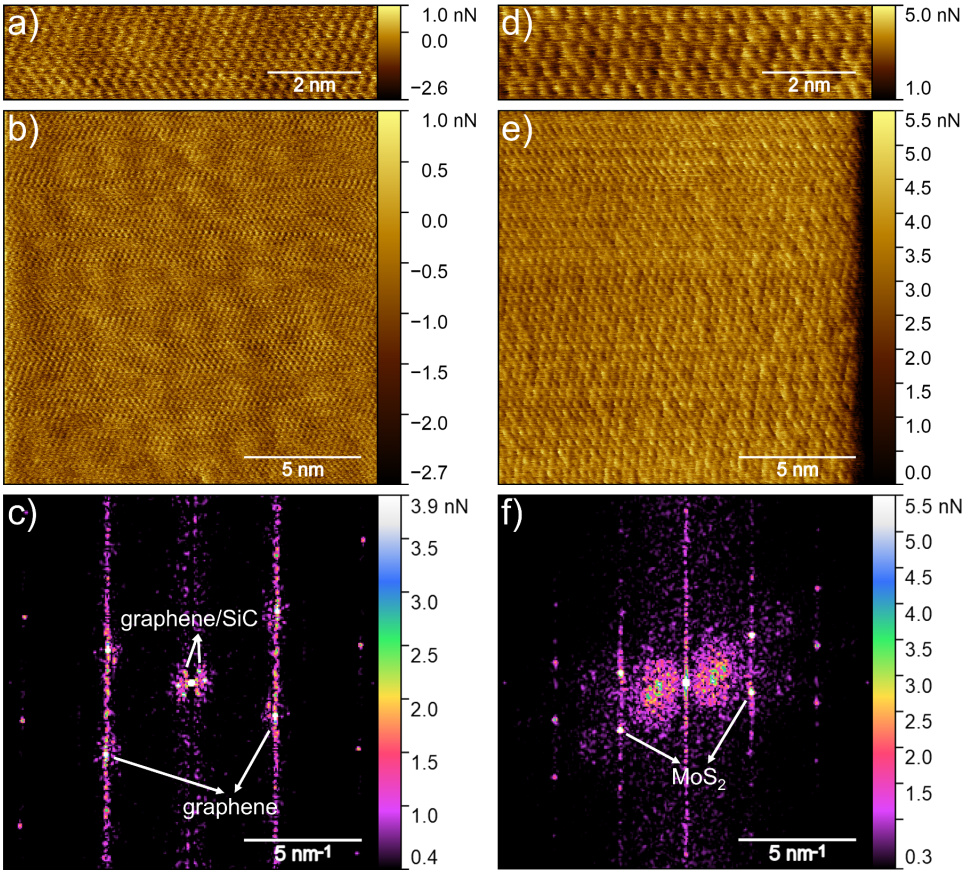

Figure 5.2: Friction force maps recorded on an area of epitaxial graphene/SiC(0001) (left) without and (right) with coverage of monolayer MoS_2: a) and d) high-resolution friction maps showing the atomic stick-slip pattern and the aligned orientation of MoS_2 and graphene; b) and e) Overview friction maps revealing the well-known moiré pattern on the epitaxial graphene/SiC(0001) surface and the weak and irregular moiré structure which originates from the overlay of the underlying moiré pattern and the lattice mismatch between graphene and MoS_2; c) and f) Fourier transformation of the friction maps in b) and e) with indicated spatial frequencies of graphene and MoS_2 lattices and graphene/SiC(0001) moiré pattern. The figure is adopted from Ref.[2].

5.1.2 Manipulation of MoS_2 flakes

If needed, the clusters of unreacted material can be removed from the MoS_2 islands by means of the AFM tip in contact mode at very low applied forces. The MoS_2 islands can be also easily displaced with the same method [119] unless they are firmly attached to substrate features such as steps of the SiC(0001) substrate [84].

Liao *et al.* [86] described two strategies for the manipulation of islands of 2D materials. The first strategy is to push the island with the AFM tip from the side. The second strategy is to drag the island with the AFM tip pressed on top of it. Both strategies were applied for the MoS_2 island manipulation presented in figure 5.3. Figure 5.3a) demonstrates the positions to which the MoS_2 island was relocated including the return to the initial position. In the beginning, the MoS_2 island has a cluster of unreacted material on top (figure 5.3b)). By performing the scanning in contact mode at a normal load close to 0 nN, the cluster was pushed out from the island. In the following scans, a tip-induced shear displacement of the uppermost MoS_2 layer with respect to the underlying layers of the MoS_2 was not possible, even after multiple repetitions and at an increased normal load. Finally, during those attempts to remove the second layer of MoS_2, the entire MoS_2 island was displaced (figure 5.3c) step 2)).

In order to bring the island back to the starting position, the MoS_2 island was dislocated to multiple locations (figure 5.3c) from 3) to 5)) by using the same pushing strategy, while scanning. The results demonstrate that this pushing strategy is unreliable. The moment at which the MoS_2 island is being moved is hard to predict during the scan. Similarly, the direction of the displacement is difficult to predict. In the last two steps (figure 5.3c) step 6) and 7)), the strategy of manipulation was changed to the dragging. The AFM tip was moved on top of the MoS_2 island and a normal load of 1 μN was applied. In such conditions, the tip was then moved manually to the starting position, dragging the island below. Figure 5.3c) step 6) shows that in the first approach, the MoS_2 island slipped and lost contact with the tip. In the second approach, the island was moved almost to the starting position (figure 5.3c) step 7)). The large islands (a few μm in edge length) can be rotated to various angles by manipulation [85], while smaller islands rotated this way (hundreds of nm in edge length, like the one presented in this chapter) realign themselves to the substrate lattice [84]. Figure 5.3c) steps from 4) to 7) indicate that both displacement strategies may cause rotation of the MoS_2 island.

Because the MoS_2 island can be easily displaced, there is no certainty whether the MoS_2 island is immobile during friction measurements and how potential MoS_2 island mobility affects recorded friction. The island can be also damaged during manipulation [119]. For that reason, the following results reported in this chapter are only for islands which are firmly attached to the substrate features from the beginning. The immobility of the islands during the experiments is assumed.

5.1.3 Number of layers dependance

The load dependence of friction on MoS_2 islands with a thickness between 1 and 4 layers is summarized in figure 5.4. The load dependence exhibits the sub-linear characteristic of single-asperity friction with significant adhesion [80, 120]. Friction decreases from 1 to 4 layers of MoS_2, primarily due to a decrease in adhesion. Figure 5.4 also shows the relatively small

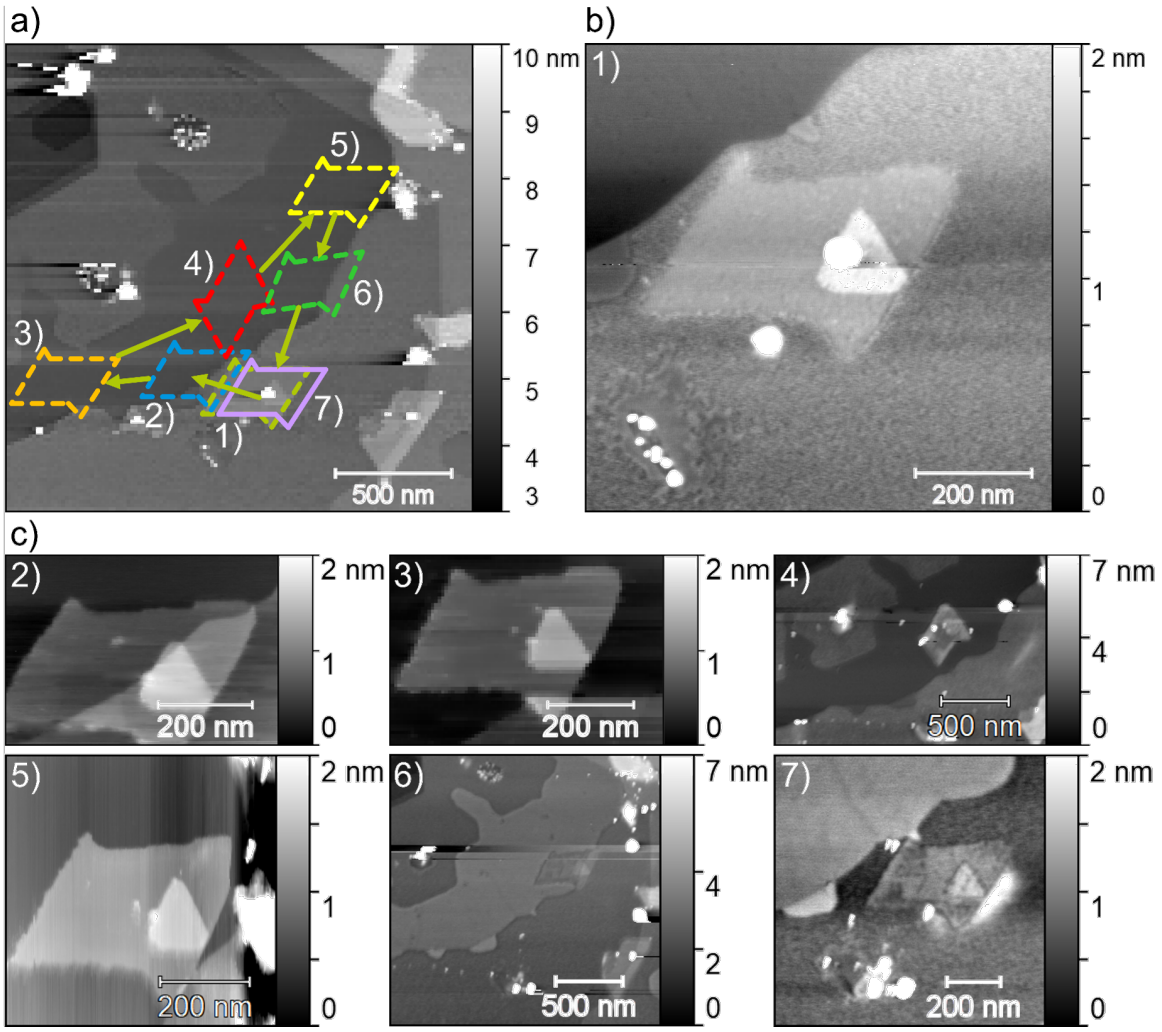

Figure 5.3: Manipulation of MoS_2 flakes: a) topography image with positions of MoS_2 island at each step; b) image of initial position 1) of MoS_2 island; c) images of MoS_2 island at positions for steps from 2 to 7. At steps 2) to 6) the MoS_2 flake is on the bilayer graphene. At position 1) and 7) the MoS_2 flake is on the monolayer graphene. In this case, the monolayer graphene is elevated by additional atomic layers of SiC and is higher than the bilayer. Images of steps 6) and 7) were taken in the non-contact mode without compensating CPD, which resulted in the bilayer graphene area being higher than on the rest of the images. Difference in CPD between mono- and bilayer graphene causes the latter to be recorded as higher.

changes in friction when a bias voltage is applied to the sample. Friction data was recorded at compensated contact potential difference and for selected voltages above and below U_{CPD}.

To describe the dependence of the friction force F_L on the normal force F_N by relevant parameters, we have modeled it as $F_L = \tau \cdot A$, where τ is the shear strength and A is the contact area which is described by the Derjaguin-Muller-Toporov (DMT) contact mechanics model [121]:

$$F_L = \pi \left(\frac{3r}{4}\right)^{\frac{2}{3}} \cdot \frac{\tau}{E_{eff}^{\frac{2}{3}}} \cdot (F_N + 2\pi r\gamma)^{\frac{2}{3}} = \mu_{DMT} \cdot (F_N + 2\pi r\gamma)^{\frac{2}{3}} \tag{5.1}$$

where r is the tip radius, E_{eff} is the effective elastic modulus of the combined system of tip and sample, and γ is the adhesion energy. For simplicity, we define a normalized shear stress $\mu_{DMT} = \pi(3r/4)^{\frac{2}{3}} \cdot \tau / E_{eff}^{\frac{2}{3}}$. The DMT fits describe the non-linear load dependence of friction

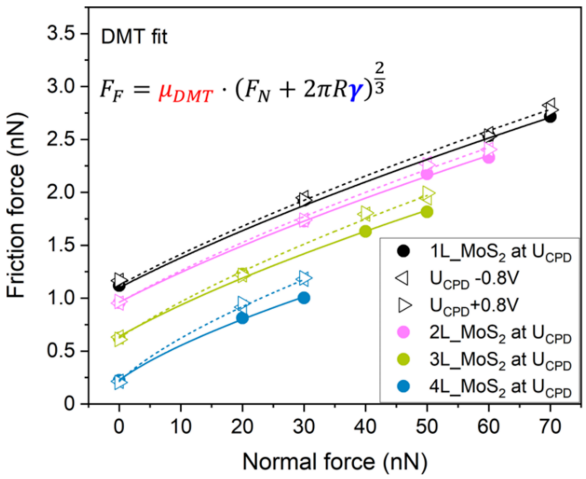

Figure 5.4: Friction force as a function of normal force on MoS_2 on graphene/SiC(0001). Results are presented for 1–4 layers of MoS_2 at compensated contact potential difference (●) and 0.8 V above (▷) or below (◁) using a conductive tip. The data are fitted with the DMT model indicated. The figure is adopted from Ref.[2].

by two parameters, the tip-specific friction coefficient μ_{DMT} for single-asperity friction and the adhesion energy γ, which is defined by an adhesive contribution to friction at zero applied load. We will discuss below in how far the deformation of layered materials limits the applicability of the DMT contact mechanics model [66].

All experimental results presented in figure 5.4 were recorded with one electrically conductive AFM tip. The conductivity of each tip depends on the thickness of the oxide layer at the tip apex, which is easily worn off in contact-mode experiments. Since we have found differences in bias-dependent friction between conductive and insulating tips, we characterize their properties in comparison. The electrical current vs. applied voltage for a conductive tip in contact with 1 to 4 layers of MoS_2 is plotted in figure 5.5a). The current depends strongly on the applied normal load, increasing from 20 to 370 pA when increasing the normal load from 0 nN to 70 nN on a monolayer MoS_2 at a bias of -1.2 V. On 4 layers of MoS_2, the current increases only from 6 to 12 pA in the same range of normal forces. While we cannot offer a predictive model for the current-voltage characteristics of the interface comprising doped silicon, silicon oxide, MoS_2 layers, graphene, and SiC(0001), we noticed that the conductivity was reduced to zero for an insulating tip (figure 5.5a)).

A bias voltage applied between sample and tip is expected to increase their electrostatic attraction. We have combined friction force microscopy with non-contact KPFM using the same AFM tip to determine the bias voltage at which the electrostatic attraction is minimized. The minimum indicates that the contact potential difference is compensated and reveals the work function difference between tip and sample. Figure 5.5b) compares the contact potential difference U_{CPD} between tip and sample for the conductive and the insulating tip. There is constant offset of 0.81 V between the two tips for all surface layers, which confirms a constant difference in the work function between tips. The relative shift of the work function for different numbers of MoS_2 layers with respect to the graphene/SiC(0001) is the same for both tips, the values are provided in table 5.1. Performing these experiments in ultrahigh vacuum ensures that the values are not affected by water as the most critical adsorbent [122].

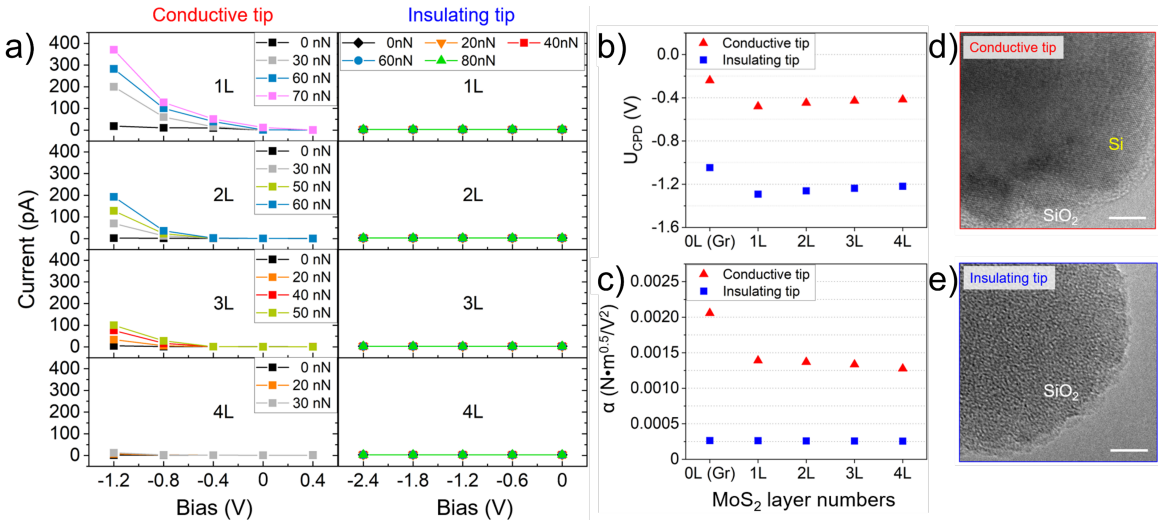

Figure 5.5: Comparison of a conductive and an insulating tip: a) electrical current as function of applied bias and applied load for the tips in contact with 1–4 layers MoS_2 on graphene/SiC(0001); b) layer-dependence of the contact potential difference U_{CPD} for conductive and insulating tip, determined by non-contact KPFM; c) strength of bias-dependent electrostatic tip–sample interaction α for 1–4 layers of MoS_2 and the underlying graphene/SiC(0001), determined by non-contact KPFM; d) TEM image of a conductive tip with crystalline structure of the Si(100) plane close to the apex; e) TEM image of the insulating tip with amorphous structure of the apex (scale bars: 5 nm). The figure is adopted from Ref. [2].

Table 5.1: Work function shift of 1 to 4 layers of MoS_2 with respect to the graphene/SiC(0001) substrate. The table is adopted from Ref.[2].

1 layer of MoS_2	2 layers of MoS_2	3 layers of MoS_2	4 layers of MoS_2
-242 mV	-210 mV	-188 mV	-174 mV

In KPFM, the bias dependence of the electrostatic tip-sample attraction is measured as negative frequency shift of the cantilever's resonance. The normalized frequency shift [123] has a parabolic dependence on the applied bias $\Delta f / f_0 k^{3/2} = -\alpha(U_{bias} - U_{CPD})^2$. Figure 5.5c) shows that the strength of the electrostatic tip-sample attraction is at least a factor of three smaller for the insulating tip and does not vary when measured on graphene or 1 to 4 layers of MoS_2. In contrast, the conductive tip has a significantly stronger interaction with graphene and shows a slight decrease in interaction with increasing number of MoS_2 layers.

Transmission electron microscopy [TEM] delivers insights into the structure of the AFM tip apex. While the conductive tip exhibits the regular atomic lattice of the Si(001) plane up to 2 nm below the tip end (figure 5.5d)), the insulating tip exhibits the amorphous oxide structure for at least ten nanometers from the tip end (figure 5.5e)). Such a thick oxide at the apex is result of the micro-fabrication process and typical for un-used tips, but is easily lost in the process of imaging larger areas to find MoS_2 islands of different height. Tips were imaged by TEM immediately after the friction experiments on different MoS_2 islands.

The dependence of the DMT parameters on the applied bias voltage and on the number of MoS_2 layers is summarized in figure 5.6 for one conductive and one insulating tip. For the conductive tip, the DMT friction coefficient μ_{DMT} shows a minimum around the compensated contact potential U_{CPD}, with a decrease of about 5% with respect to $\pm$0.8 V bias. The adhesion parameter γ exhibits a weak maximum at U_{CPD}. We note that these bias dependencies do not take the parabolic form which is always observed for the electrostatic attraction in non-contact

mode. While μ_{DMT} decreases by about 15% from 1 to 4 layers of MoS_2, the adhesion γ drops linearly to almost zero.

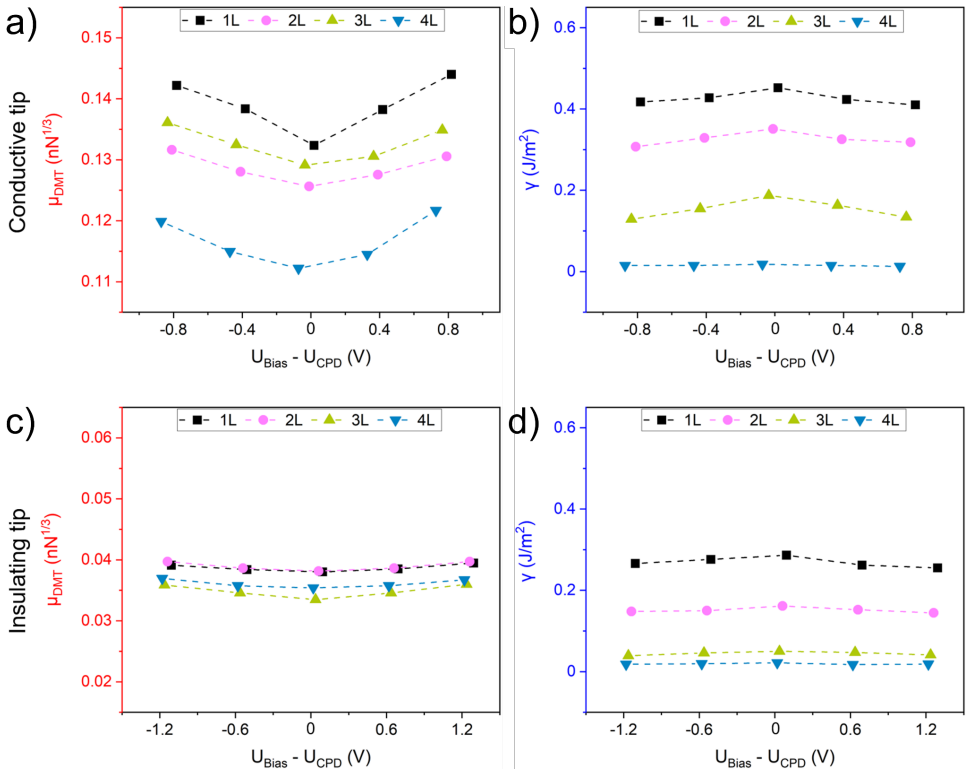

Figure 5.6: Graphical summary of parameters describing the load dependence of friction in the DMT model for 1–4 layers of MoS_2 on graphene/SiC(0001): a) and b) a conductive tip, c) and d) an insulating tip; a) and c) bias-dependence of the DMT friction coefficient μ_{DMT}; b) and d) bias-dependence of the adhesion parameter γ. The figure is adopted from Ref.[2].

For the insulating tip, μ_{DMT} exhibits a much weaker minimum at the compensated contact potential U_{CPD} and also a much weaker dependence on the number of MoS_2 layers (figure 5.6c)). The bias dependence of the adhesion is also weaker, but a strong dependence on the number of MoS_2 layers lets γ decays towards zero for 1 to 4 layers.

The dependence of friction on the number of MoS_2 layers is compared with that for the graphene/SiC(0001) substrate in figure 5.7 for three different conductive tips and one insulating tip. The DMT friction coefficient μ_{DMT} is more than six times higher on 1 layer of MoS_2 than on the underlying graphene/SiC(0001), it is also more than three times higher for the conducting tips than for the insulating tip on graphene/SiC(0001) and on 1 layer of MoS_2. For all conductive tips, μ_{DMT} takes a reduced value on 4 layers of MoS_2. The adhesion parameter γ is close to zero on graphene/SiC(0001) for all tips. On MoS_2, it takes values of up to 500 mJ m^{-2}, or 300 mJ m^{-2} for the insulating tip, and decays strongly from 1 to 4 layers.

5.2 Discussion

The experimental results for the SiO_x tip sliding on MoS_2/graphene/SiC(0001) can be summarized in three key observations: the decrease of friction on an increasing number of MoS_2 layers is caused mostly by a decrease of adhesion and less by a decrease of shear stress, an applied bias voltage affects the shear stress but not the adhesion, and the effect of the bias

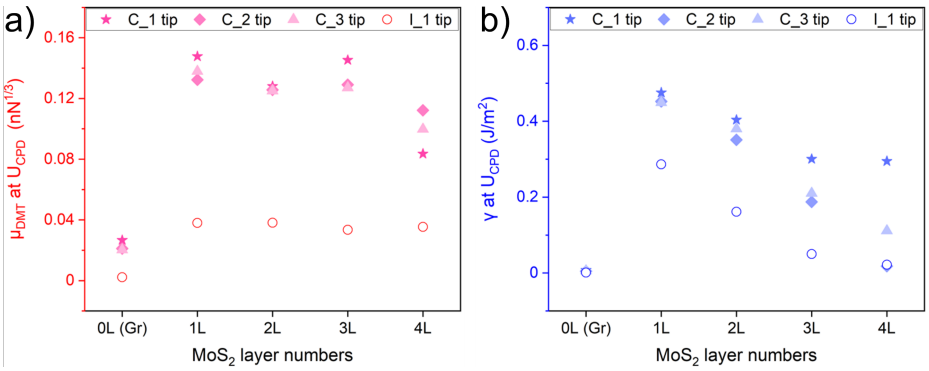

Figure 5.7: Layer-dependence of the parameters describing the load dependence of friction in the DMT model at U_{CPD}: for three conductive tips (full symbols) and one insulating tip (hollow symbol). The figure is adopted from Ref.[2].

voltage depends strongly on the thickness of the oxide layer on the tip.

The dominance of adhesion in the layer-dependence of friction on MoS_2 is revealed by the offset between friction vs. load curves for different layer number, where the curves have a similar slope (figure 5.4b)). Similar characteristics have been reported before for experiments on MoS_2 of varying thickness in ambient conditions [60, 80, 64, 124] and are confirmed here for measurements in ultrahigh vacuum on CVD-grown MoS_2. The strong decrease of adhesion from 1 to 4 layers of MoS_2, almost to zero for most tips (figure 5.7b)), cannot be attributed to the screening of electrostatic adhesion, since there is almost no bias dependence of adhesion (figure 5.6b) and 5.6d)). We rather suggest that out-of-plane deformation of the MoS_2 layers leads to a conformation of the layers to the tip apex shape, thus to a larger contact area, and consequently to higher friction. This so-called 'puckering' effect is reduced with increasing number of MoS_2 layers due to the increasing bending stiffness [61, 64] (figure 5.8). The interaction of MoS_2 with the graphene is expected to be weak (0.15 mJ m^{-2}) [125] compared to the interaction between MoS_2 layers (0.55 mJ m^{-2}) [126]. Fang *et al.* have suggested that the layer-dependence of friction depends on the tip shape, when friction depends on both shear stress and effects of out-of-plane deformation [127]. In terms of their arguments, the layer dependence of friction on MoS_2 in our experiments is dominated by the out-of-plane deformation caused by a sharp AFM tip. A contribution of out-of-plane deformation to friction is not expected for the epitaxial graphene layer, which is more strongly bound to the graphitic termination of the SiC(0001) substrate [62]. This expectation is confirmed by the absence of any significant adhesion on graphene/SiC(0001) for all tips (figure 5.7b)).

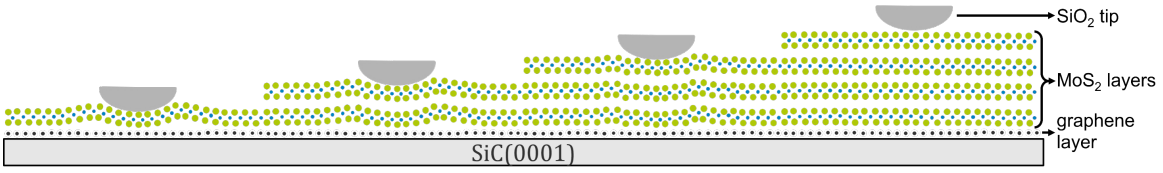

Figure 5.8: Scheme of the puckering effect. Interactions between the SiO_2 tip and MoS_2 are stronger than MoS_2 and graphene, which leads to out-of-plane deformation of the MoS_2 layers and a conformation of the layers to the tip apex shape. With increasing number of layer, the MoS_2 islands become more rigid and less susceptible to deformation.

The tip-specific friction coefficient μ_{DMT} exhibits only a weak decrease with increasing

number of MoS_2 layers (figure 5.7a)). This weaker dependence of μ_{DMT} on the number of layers confirms that the variation in friction can mostly be attributed to a variation of the effective adhesion γ, and not to a variation of the effective compliance $1/E_{eff}^{2/3}$. The weak dependence of μ_{DMT} also indicates that there is no strong variation of E_{eff} with the number of layers. The parameter μ_{DMT} reports the load dependence of friction and we conclude with Vaziriserehk *et al.* [80] that the dominating physical property is the load dependent atomic potential corrugation which impedes the lateral sliding. In agreement with their atomistic simulations, the coefficient μ_{DMT} is significantly smaller for graphene than for MoS_2. Lavini *et al.* have noted that the in-plane polarization of each MoS_2 layer may cause a difference in friction between odd numbers of MoS_2 layers and even-numbered ones with no net polarization [60]. The coefficient of load dependence μ_{DMT} indeed shows such an odd/even contrast for all conductive tips (figure 5.7a)). For our system of large single-crystal islands of MoS_2, the odd/even contrast does not reflect charges at the edges of MoS_2 islands but rather contrasts in the load-dependence of the potential corrugation.

Friction is lower when the applied bias voltage compensates contact potential difference between tip and sample (figure 5.6), which was determined as U_{CPD} in the non-contact KPFM mode. This bias dependence of friction is observed only at higher load, while friction at zero applied normal force does not show the bias dependence (figure 5.4b)). Although our KPFM experiments reveal that there must be an electrostatic contribution to adhesion, is appears to be a negligible contribution for bias voltages ± 1.2 V around U_{CPD}. We suggest that the bias dependence of friction originates in an increase of the potential corrugation when the in-plane polarization of the MoS_2 layers is distorted in the external normal electric field.

The shift in work function between graphene/SiC(0001) and MoS_2/graphene/SiC(0001) of -242 mV is of the same order as the one reported by Forti *et al.* for WSe_2 on the same substrate, who explained the overall electronic structure in terms of pinning by the n-doping in the graphene layer on SiC(0001) [128]. The shift in work function of 30 mV between 1L and 2L and then between subsequent layers is smaller than reported for MoS_2 flakes on SiO_x [129] and smaller than for MoS_2/graphene/SiC(0001) recorded in ambient conditions, where charged adsorbates influence the work functions [60].

Contact potential difference U_{CPD}, conductivity of the contact with the MoS_2 layers, and the bias-dependence of electrostatic tip-sample attraction depend critically on the oxide thickness at the tip apex (figure 5.5). While no current was detected through contacts with the 10 nm oxide tip, a tunneling current was measured for the 2 nm oxide tip where the current increased super-linearly with applied bias. This characteristic has been explained by Liao *et al.* for a metal tip in contact with MoS_2/graphite as thermally emitted current across a Schottky barrier [130]. The authors attributed the load dependence of the current (figure 5.5a)) not only to a variation of the contact area but also to a decrease of the Schottky barrier with increasing pressure. We find that the current is greatly reduced for thicker MoS_2 layers and suggest that the tunneling probability across multi-layer MoS_2 may be further reduced by the band gap expected for negative sample bias [118, 131].

The oxide at the tip also has a strong influence on friction and its bias dependence. While the adhesion γ is of similar magnitude and shows the same dependence on the number of MoS_2 layers (figure 5.7b)) for insulating and conductive tips, the tip-specific coefficient μ_{DMT}

is by a factor of three lower and does not show any layer dependence for the insulating tip. Furthermore, the bias dependence of μ_{DMT} (figure 5.6a)) is flat for the insulating tip (figure 5.6b)). Please note that compensation of the work function minimizes the electrostatic attraction but does not cancel electric fields across the contact. This is manifest by the observation of significant electrical current through the conductive tip at an applied bias of -0.4 V (figure 5.5a)), which is the compensating bias for this tip (figure 5.5b)). However, no current is measured through the insulating tip at the higher bias of -1.2 V, which is the compensating bias for this tip.

These observations support our picture of the underlying mechanisms. The adhesion is dominated not by electrical tip properties but by out-of-plane deformations of MoS_2 layers towards the shape of the tip apex, with a smaller resulting contact area for the tip whose sharp oxide is not worn off. The friction coefficient μ_{DMT} is sensitive to an enhancement of the atomic potential corrugation in the applied electric field, which is rather weak when the potential is applied across an tip oxide as thick as 10 nm.

Due to different lattice constants, there is significant incommensurability between MoS_2 islands and the graphene layer. By necessity, it causes reconfiguration into the superstructure and leads to the formation of the moiré pattern. Such a pattern was predicted theoretically multiple times for this pair of materials and observed e.g. by STM [132]. However, no modulation of friction forces following the moiré pattern was observed between MoS_2 and graphene in this work. To the best of the author of this work knowledge, up to this date such observations were reported only for 2D materials on bulk materials [79, 82, 70, 133] but not for two incommensurate 2D materials. It can be explained by the structure of TMDC materials. One molecular layer of MoS_2 has three atomic sub-layers. While the immediate atomic sub-layer is contacting the material with different lattice constant, it deforms out-of-plane and forms the moiré pattern. However, this out-of-plane deformation is reduced with next atomic sub-layers, that it is not detectable for AFM techniques. Another effect of incommensurability between MoS_2 islands and the graphene layer is the structural superlubricity [35]. This and weak normal-to-plane van der Waals interactions between 2D materials allow easy manipulation of MoS_2 island on graphene. The remaining extremely low friction between these two materials is dominated by the edge-pinning effect, rather than interface friction [86].

5.3 Conclusions

In conclusion, the combination of non-contact Kelvin Probe Force Microscopy with contact-mode friction force microscopy in ultra-high vacuum has revealed the mechanisms of nanoscale friction on ultra-thin layers of MoS_2 grown on graphene/SiC(0001). The overall strength of friction is dominated by adhesion which is mediated by a deformation of MoS_2 to adapt the tip shape. Friction decreases with the increasing number of MoS_2 layers as the bending rigidity leads to less deformation. The dependence of friction on applied load and bias voltage can be attributed to variations in the atomic potential corrugation of the MoS_2/SiO_x interface, which is enhanced by both load and bias. The results enrich our understanding of the mechanical properties of heterostructures of 2D materials and thus contribute to a rational design of lubricating interfaces built from this new class of materials.

6 Nanoscale friction on graphene/hBN and $MoSe_2$/hBN van der Waals heterostructures

Nanotribological investigations of two van der Waals heterostructures of $MoSe_2$/hBN and graphene/hBN on SiO_2 are the topic of this chapter. This material is still not published and is exclusive only to this work. The dependence of normal load on friction force was measured with SiO_2 probes (PPP-ContR and PPP-FMR). Localization and examination of the same areas with different cantilevers were possible because of the presence of a navigational microstructure. Before experiments, an undissolved residue left by the transfer technique was removed from experimental areas on both heterostructures by means of the scanning AFM tip, which was not used for subsequent experiments.

6.1 Experimental results

The graphene/hBN and $MoSe_2$/hBN heterostructures were fabricated to extend previously described studies and compare different preparation methods. The goal of this study is to explore new combinations of heterostructures and their tribological properties. However, the exfoliation method used for the preparation of graphene/hBN and $MoSe_2$/hBN heterostructures has disadvantages that cause problems in surface science studies. The exfoliated flakes are difficult to locate because they are tens of μm large and are distributed with hundreds of μm of the radius range but only locally on the sample. To address this problem, the navigational microstructure was designed and implemented before the fabrication of the heterostructures.

6.1.1 Topography and identification of heterostructures

The assembly of graphene/hBN heterostructure was performed in two steps. In the first step, an hBN flake [hBN*] was placed on the SiO_x substrate. In the second step, a graphene [graphene/hBN] was stacked on top of the hBN flake. Based on height measurements, the hBN* is 8 layers thick, and the graphene has areas with 1–3 layers. The coordinates of the navigational microstructure ("3CW") are still readable from the AFM image after their coverage with graphene/hBN heterostructures (figure 6.1a)). The graphene flake forms local blisters typical for exfoliated 2D materials. Areas with mono- and bilayer graphene on hBN were identified based on differences in height and the work function [77]. In contrast to the epitaxial graphene on SiC(0001), the layers of exfoliated graphene are folding (figure 6.1b)). Although rough surface and folding make height measurements more challenging, it was possible to find unfolded graphene and directly confirm that it is a monolayer with a height of around 300 pm, close to the literature value [77]. The monolayer graphene has a lower work function than hBN flake, which remains the same, whether graphene covers hBN or SiO_2 (figure 6.1c)). The SiO_2 surface remains still covered with the undissolved residue, which is also observed in graphene/SiO_2 topography. The residue distorts the CDP map over the SiO_2 area. The hBN surface was cleared from the remaining residue. An elevation with an irregular shape next to the edge of the hBN flake is caused by the material intercalated below the hBN flake. Higher work function in the vicinity of the coordinates of the navigational microstructure can be caused by gallium ions used for the preparation of the microstructure.

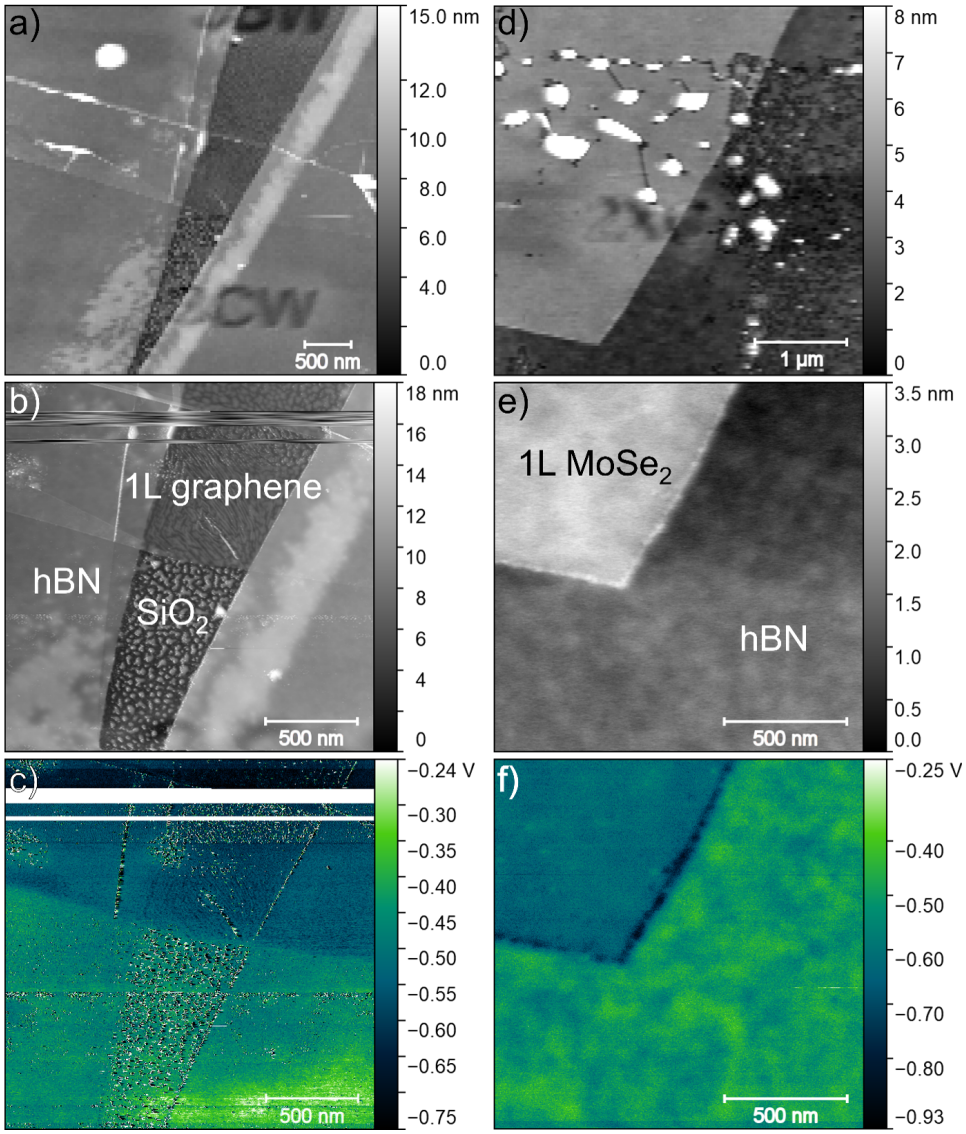

Figure 6.1: Topography of graphene/hBN (left) and $MoSe_2$/hBN heterostructures (right): a) and d) non-contact mode topography image with coordinates of navigational microstructure in range; b) and e) topography recorded with non-contact mode assisted with KPFM method; c) and f) CPD maps recorded with KPFM simultaneously with the data presented in b) and e) respectively.

A monolayer of $MoSe_2$ [$MoSe_2$/hBN] was stacked on a second hBN flake [hBN**], which was around 60 layers thick. Figure 6.1d) shows that the coordinates of the navigational microstructure are readable ("2XC"), even after being covered with the thicker flake of hBN. The clearing of the sample surface from residue was focused only on areas of interest, therefore residue still remains in the vicinity around (figure 6.1d)). The $MoSe_2$ flake forms local blisters, similarly to the exfoliated graphene. The monolayer $MoSe_2$ was recognized by its height of around 650 pm (figure 6.1e)), which is in agreement with the literature [57], and a lower value of work function with respect to hBN (figure 6.1f)).

The areas prepared for friction experiments are presented in figure 6.2. The surface of hBN* is not atomically flat and has a roughness parameter $RMS = 179.7$ pm (figure 6.2a)). The graphene/hBN surface roughness parameter RMS is 138 pm (figure 6.2b)). The surface of 60 layers thick hBN** flake has a roughness $RMS = 92.71$ pm in the experimental area

(figure 6.2c)). The roughness parameter *RMS* measured on the $MoSe_2$/hBN heterostructure is 136.8 pm (figure 6.2d)). While these values of roughness measured on exfoliated 2D materials are only local and may vary when the scan frame is moved, they are always higher than the roughness of atomically flat epitaxial graphene on SiC(0001) (figure 6.2e)), which was investigated in chapter 4. The measured roughness suggests that exfoliated 2D materials comply with the roughness of the SiO_2 substrate, which is much higher than the roughness of SiC(0001). The friction measurements were conducted on much smaller 8 nm $\times$ 2 nm friction maps.

The topography of exfoliated graphene/hBN and $MoSe_2$/hBN demonstrate van der Waals heterostructures with considerably larger areas than the MoS_2 flakes obtained by the CVD method on epitaxial graphene on SiC(0001) and discussed in chapter 5. Readable coordinates of navigational microstructure allow easy location and selection of experimental areas. The influence of the roughness of exfoliated 2D materials on measured friction will be discussed in section 6.2.

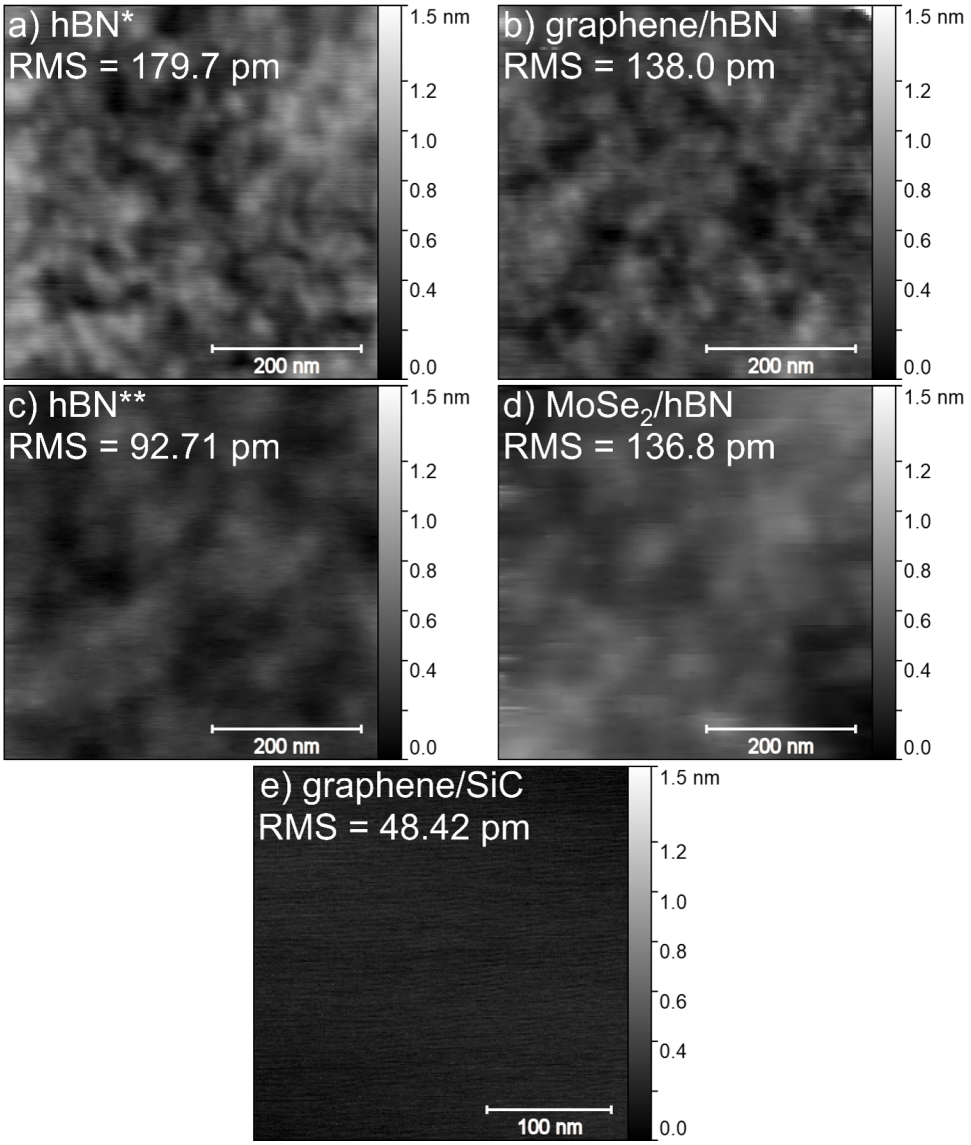

Figure 6.2: Comparison of roughness in experimental areas on a), c) pristine hBN, heterostructures of b) graphene/hBN, d) $MoSe_2$/hBN and e) epitaxial graphene on SiC(0001)(from experiments in chapter 4).

6.1.2 Orientation of atomic lattices

High-resolution friction maps allow to record periodicity and orientation of atomic lattice. Figure 6.3 shows examples of such friction maps with friction loops demonstrated in their profiles. The graphene/hBN heterostructure is rotated 15.4° with respect to fast scan direction (figure 6.3a)), whereas the hBN flake beneath is rotated 25.4° (figure 6.3b)). This 10° difference is caused by the exfoliation technique, during which it is difficult to exactly determine the orientation of the flake. A reorientation of the flake might not occur, due to partial direct anchoring of the flake on the SiO_2 substrate. Figures 6.3c,d) show that lattice orientations of $MoSe_2$ and hBN** are aligned and rotated 8.9° with respect to the fast scan direction. In this case, the $MoSe_2$ flake is small and entirely on top of the hBN flake. If the $MoSe_2$ flake was not initially aligned to the hBN during exfoliation, the reorientation phenomenon may have rotated the $MoSe_2$ flake. No moiré pattern was recorded in lateral signal on both heterostructures of graphene/hBN and $MoSe_2$/hBN, also in larger range friction maps. Reasons for the lack of observation of the moiré superstructure will be addressed in the discussion (section 6.2).

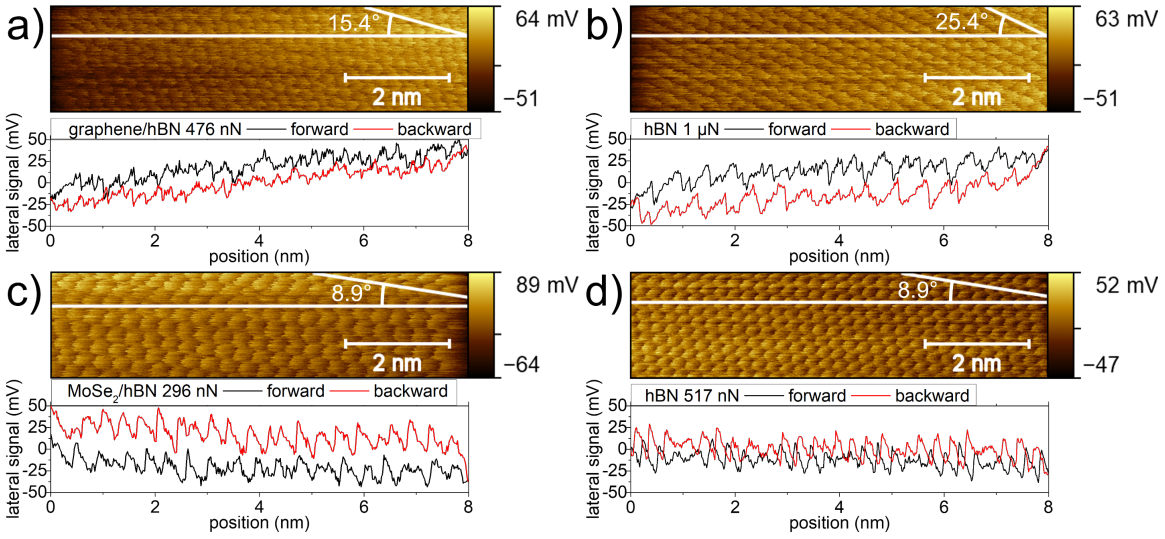

Figure 6.3: High resolution friction maps recorded with SiO_x tip on exfoliated 2D materials: a) graphene/hBN heterostructure, b) hBN*, c) $MoSe_2$/hBN heterostructure, d) hBN**.

The stick-slip pattern periodicity is equal to lattice constants of hexagonal crystallographic lattice if a "zigzag" orientation is aligned to the fast scan direction. This is not the case for the hBN* and the graphene/hBN heterostructure, because their rotation is closer to an "armchair" orientation along the fast scan direction. Because of the small rotation angle of hBN** and $MoSe_2$ lattices with respect to the fast scan direction, the periodicity of the stick-slip is close in value to the lattice constants of both hBN and $MoSe_2$. The stick-slip periodicity recorded on hBN** is 258 pm, which is 3% higher than the literature value of 250.4 pm [134]. The stick-slip periodicity recorded on $MoSe_2$ is 348 pm, which is 4.8% higher than the literature value of 332 pm [135]. The significant difference in periodicity of the stick-slip is another parameter to distinguish surfaces during an experiment.

Friction loops recorded during friction experiments on all four surfaces exhibit a characteristic tilt. The tilt is an optical effect. The deflection of the laser beam from the cantilever is affected by the cantilever position. It is suggested that the tilt of the tube scanner results in a slightly

Table 6.1: Coefficient of friction of exfoliated hBN and van der Waals heterostructures of graphene/hBN.

surface	hBN**		hBN*	1L graphene/hBN	2L graphene/hBN
cantilever	PPP-FMR	PPP-ContR			
μ [10^{-3}]	0.82 ± 0.06	2.8 ± 0.3	3.3 ± 0.5	3.2 ± 0.6	3.8 ± 0.4

different deflection angle for the laser beam. The friction loops are tilted in a different direction due to reversed directions of forward and backward scan. The experiments on hBN** and $MoSe_2$/hBN heterostructure were performed with the standard fast scan direction. However, the position of the graphene/hBN heterostructure on the sample was not available for AFM, unless the entire sample was rotated 180° inside the sample holder. To unify the experiments, the measurements on hBN* and graphene/hBN heterostructure were performed with the reversed fast scan direction. Therefore, for friction measurements on hBN* and graphene/hBN, the values of the forward lateral signal and the backward lateral signal are reversed.

6.1.3 Friction force measurements

Friction experiments were conducted with the oxidized silicon tips on two types of silicon cantilevers: soft PPP-ContR and stiffer PPP-FMR (details in section 3.4.3). Results of the friction force as a function of normal load are presented in figure 6.4. The friction force increases linearly in experiments with the soft PPP-ContR cantilever for both hBN and graphene/hBN heterostructures (figure 6.4a)). The scatter of data increases significantly above 100 nN of normal load. The coefficient of friction is defined here as a slope of the curve. In general, values of friction on both hBN and graphene/hBN heterostructure are almost overlapping and both materials have very similar coefficient of friction. The values are listed in table 6.1. For hBN, the coefficient of friction is equal to $0.003\,3 \pm 0.000\,5$. On monolayer graphene on hBN, the friction increases with the coefficient $0.002\,4 \pm 0.000\,3$, but after omitting the outlying result at 310 nN of normal load, the coefficient of friction is $0.003\,2 \pm 0.000\,6$. On bilayer graphene, the friction coefficient is $0.003\,8 \pm 0.000\,4$. At the low normal load range, the friction on graphene is slightly higher than on hBN, due to the adhesion force.

In the extended plot in figure 6.4b) more results measured with the PPP-FMR cantilever are shown. In this range up to 1500 nN, the load dependence exhibits sub-linear characteristic of single-asperity friction. To analyze this type of sub-linear characteristic, the DMT contact mechanics model [121] was fitted based on equation A1 from chapter 5[2]. The tip-specific friction coefficient μ_{DMT} and the adhesion energy γ were calculated and summarized in table 6.2 for all relevant curves. The μ_{DMT} parameters for hBN* and graphene/hBN are similar to each other and slightly higher than that for epitaxial graphene on SiC(0001) (chapter 5 figure 5.7 [2]). Higher μ_{DMT} of exfoliated 2D materials might be related to increased roughness. In comparison to epitaxial graphene on SiC(0001), the adhesion energy γ for hBN* is similarly close to 0, while it is much higher for graphene/hBN heterostructure. This indicates that potential energy surface corrugations for both hBN and graphene/hBN heterostructure are similar, but the weak connection between hBN and graphene results in an increased influence of adhesion on the friction force. The adhesion force leads to the puckering effect and slightly higher friction force for the low normal load.

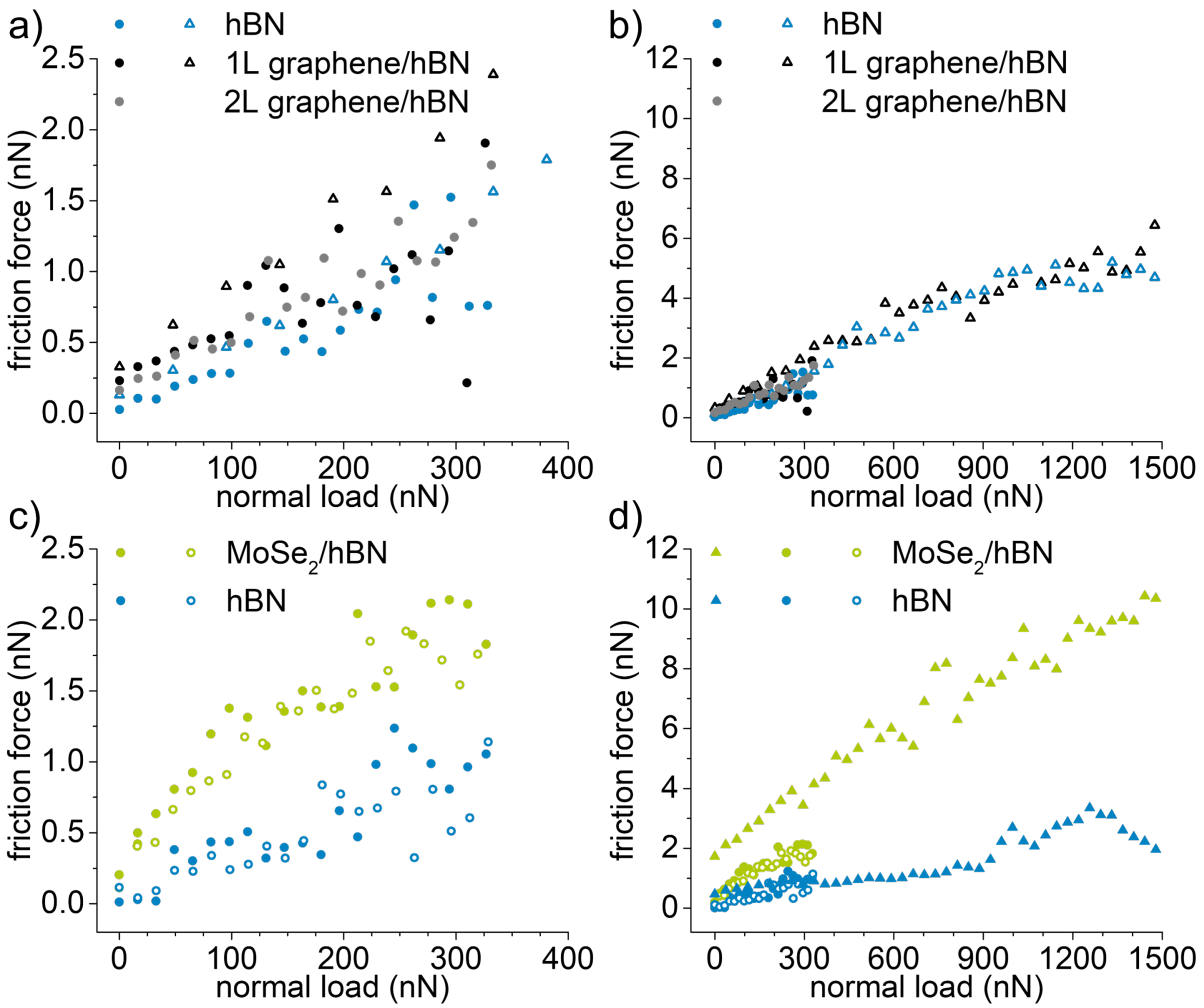

Figure 6.4: Friction force as a function of increasing normal load between SiO_x tips and graphene/hBN heterostructure: a) results of friction experiments conducted with soft silicon PPP-ContR cantilever (circles) and stiffer PPP-FMR cantilever (triangles); b) zoom out of plot a).

The friction force measured on hBN** with the soft PPP-ContR cantilever exhibits linear increase (figure 6.4c)). The coefficient of friction calculated from both friction measurements series on hBN** combined is 0.0028 ± 0.0003. The value of the coefficient of friction and scatter in the results of the friction force is similar to the results obtained on hBN* with the same type of cantilever. Experiments conducted with the stiffer PPP-FMR cantilever also demonstrated the linear increase in friction force with the coefficient 0.00082 ± 0.00006 until 900 nN of normal load (figure 6.4d)). Above 900 nN of normal load, the friction force started increasing faster, similarly to epitaxial graphene on SiC(0001) after its transition to the high-friction regime (chapter 4). The difference in coefficient of friction on hBN** measured with two different cantilevers can be a result of the stiffness of each cantilever. The stiffer PPP-FMR cantilever can exhibit lower sensitivity to lateral forces with respect to that of the soft PPP-ContR cantilever.

A sub-linear characteristic was found for the friction force on $MoSe_2$/hBN heterostructure as a function of normal load measured with both types of cantilevers (PPP-ContR, PPP-FMR)(figure 6.4c) and d)). The DMT model was fitted to the combined results obtained with PPP-ContR and separately to results measured with PPP-FMR. The fitting parameters are listed in the table 6.2. Overall friction is higher on $MoSe_2$/hBN than pristine hBN** when measured with the same

Table 6.2: Parameters describing the load dependence of friction in the DMT model for exfoliated van der Waals heterostructures of graphene/hBN and $MoSe_2$/hBN.

surface	hBN*	1L graphene/hBN	1L $MoSe_2$/hBN	
cantilever	PPP-FMR			PPP-ContR
estimated r	20 nm		40 nm	5 nm
μ_{DMT} [nN$^{1/3}$]	0.041 ± 0.001	0.041 ± 0.001	0.076 ± 0.002	0.042 ± 0.002
γ [mJ/m^2]	0.4 ± 66.2	400 ± 240	400 ± 90	670 ± 250

cantilever. Because of the similarity of MoS_2 to $MoSe_2$ as the TMDC 2D material, the results for friction on MoS_2 presented in chapter 5 can be compared with those for $MoSe_2$ presented in this chapter. Both μ_{DMT} values calculated for monolayer $MoSe_2$ on hBN are lower than those for monolayer MoS_2 on epitaxial graphene (figure 5.7a)). This difference indicates a lower shear stress on $MoSe_2$/hBN than on MoS_2/graphene. The γ parameter is similar for both monolayer $MoSe_2$ on hBN and monolayer MoS_2 on epitaxial graphene (figure 5.7a)). The calculation of the γ parameter might be subject to systematic error because its value is directly related to the radius of the tip r. In the case of friction investigations on exfoliated materials, the radius of the tip was not measured directly from SEM images but estimated based on adhesion force, which was measured with force spectroscopy.

The experimental results demonstrate that the friction on pristine hBN and graphene/hBN heterostructure is almost identical, while on $MoSe_2$/hBN is significantly higher. The friction results might also indicate a hBN transition from a sp^2 to sp^3 hybridization, similarly to epitaxial graphene on SiC(0001). Results on the $MoSe_2$ show similarity to other TMDC 2D material, MoS_2.

6.2 Discussion

The experimental results on heterostructures of graphene/hBN and $MoSe_2$/hBN stacked on SiO_x by the exfoliation technique demonstrate how the choice of the preparation method and of the substrate influence nanoscale friction. The similarities of hBN to graphene and $MoSe_2$ to MoS_2 were revealed. The experimental observations will be compared with previous studies.

In perfect alignment, graphene and hBN form a superstructure with a period of ≈14 nm [136]. This moire pattern is a result of the small lattice mismatch of ≈1.8% between graphene and hBN. The strain caused by the lattices mismatch leads to out-of-plane corrugation of the graphene layer with 18.3 pm amplitude [136]. The graphene/hBN moiré pattern causes additional stick-slip with the period of the superstructure, which is attributed to the accumulation of strain in in-plane and out-of-plane deformations of graphene and its sudden release [82, 136]. For the graphene/hBN heterostructure with the 10° orientation with respect to each other, the moiré pattern should exhibit a periodicity of ≈1.42 nm (value calculated based on the work of Zeller and Günther [137]). In this work, however, no moiré pattern was observed on either graphene/hBN or $MoSe_2$/hBN heterostructures.

The crucial difference between this work and the studies of Huang *et al.* [136] and Zhang *et al.* [82] is the method of fabrication of graphene/hBN heterostructures. In both studies, the graphene was grown directly on the hBN flake by a CVD method, which resulted in the perfect alignment of two lattices and much lower roughness. In this work, both graphene/hBN

and $MoSe_2$/hBN heterostructures were stacked on rough SiO_x from exfoliated materials. This stacking method resulted in misaligned lattices with roughness (RMS = 138 pm, figure 6.2) much larger than the amplitude of the expected moiré pattern, which is not the case for epitaxial graphene on SiC(0001). In the case of $MoSe_2$/hBN heterostructure, the triple sub-layer character of $MoSe_2$ molecular structure may prevent detection of the moiré pattern even at exact alignment, similarly to MoS_2 on epitaxial graphene on SiC(0001) (chapter 5).

The parameter γ for both graphene/hBN and $MoSe_2$/hBN heterostructures is comparable to that of MoS_2 on epitaxial graphene on SiC(0001). It reflects the influence of adhesion on the friction force. The influence of adhesion indicates the occurrence of the 'puckering' effect [61]. A poor alignment between two incommensurate 2D materials on a rough SiO_x substrate decreases the interactions between two heterolayers, which further enhances the 'puckering' effect.

The experimental results demonstrated very similar friction on hBN and the graphene/hBN heterostructure. Graphene and hBN have almost identical lattices and are isoelectronic. An important difference is that graphene is a semimetal, while hBN is dielectric. The potential energy surface corrugation is expected to be higher on hBN than on graphene/hBN due to local dipoles. The parameter μ_{DMT} describing the shear strength is almost equal on hBN and graphene/hBN. On one side, it might be speculated that the shear strength on hBN and graphene/hBN heterostructure is simply comparable, which will make the hBN an alternative to graphene for nanotribological applications. On another side, the experimental results might be explained by the enhancement of the graphene potential energy surface corrugation by the local dipoles in hBN beneath.

Barboza *et al.* [54] have observed experimentally the transition of few-layer hBN into a conductive sp^3 phase called bonitrol in the presence of hydroxy ions provided by water in a humid atmosphere under an AFM tip and a pressure of around 6.7 GPa. In dry conditions, the pressure-induced rehybridization of hBN from sp^2 to sp^3 and the formation of metastable cBN was demonstrated by Cellini *et al.* [90], in a process similar to the one for monolayer epitaxial graphene on SiC(0001) reported by Gao *et al.* [87]. Significant differences in comparison to epitaxial graphene on SiC(0001) are that the rehybridization of hBN on SiO_x requires only 2–4 GPa and occurs also for a larger amount of layers, and may last even 1 hour after release of pressure [90]. Based on the results for epitaxial graphene on SiC(0001) described in chapter 4[1] and the assumption that the hBN rehybridization causes the formation of covalent bonds between the SiO_x and cBN, the friction force increases faster after the threshold contact pressure is reached. This situation was experimentally illustrated in figure 6.4d). Simultaneous rehybridization and covalent binding of both graphene and hBN within graphene/hBN heterostructures was indicated as possible by Barboza *et al.* [91]. However, such phenomenon was not detected in this work. Roughness, incommensurate orientation and lack of compliance of graphene to hBN may be the reasons.

The friction force results for the $MoSe_2$/hBN heterostructure are very similar to that of MoS_2 on epitaxial graphene on SiC(0001). Both $MoSe_2$ and MoS_2 are TMDC materials with comparable potential energy surfaces [138] and are incommensurate on hBN or graphene due to the large mismatch in lattice. The DMT model fitting revealed that in both cases the friction force is dominated by adhesion, which is enhanced by out-of-plane deformations. The shear strength is lower on $MoSe_2$ than on MoS_2, which according to Vazirisereshk *et al.* [138] is caused

by the tip's specific trajectory on tip-sample energy landscape.

The application of the navigational microstructure proved to be successful. Markers and crosshair around the target grid allowed interoperability of the sample between optical microscopes and different AFM microscopes. The FIB microlithography produced an engraving of coordinates with the size of 1.5 μm$\times$0.5 μm, which were readable in AFM. A special design dedicated to the available piezoscanner and optical images recorded after the stacking process resulted in quick and precise localization of experimental areas. For investigation of poorly defined sample surfaces such as exfoliated 2D materials, where precise location is needed, the navigation system is highly recommended. Different navigational systems are being employed by various researchers. However, the navigational systems are very often not interoperable, because their designs are usually dedicated to work with specific instruments or have different requirements.

The navigational microstructure presented in this work can be successfully applied in future nanotribological studies of 2D materials. After proper adjustment of FIB microlithography settings, the navigational microstructure can be implemented to investigate different substrates for 2D materials. The flat surface of SiC(0001) might be an alternative to rough SiO_x substrates.

6.3 Conclusions

The strong resemblance of tribological properties was demonstrated for similar pairs of materials. Both graphene and hBN exhibit ultra-low friction which is limited by pressure-induced rehybridization from sp^2 to sp^3 and transition to a higher friction regime. The load dependence of friction force on $MoSe_2$/hBN heterostructure is weaker but comparable to that of MoS_2 on epitaxial graphene on SiC(0001). Both TMDC materials have stronger interactions with the SiO_x tip than graphene or hBN, which leads to the puckering effect and increased friction. Stacks of exfoliated 2D materials exhibit a roughness directly related to the SiO_x substrate, which prevents the observation of superstructures on graphene/hBN and $MoSe_2$/hBN van der Waals heterostructures. Efficient tribological investigations on transferred exfoliated 2D materials were possible only due to the presence of the navigational microstructure, which was engraved before the sample preparation. Application of the navigational microstructure opens possibilities to prepare numerous combinations of exfoliated 2D materials on various substrates with the quality demanded by surface science and to research their frictional properties.

7 Summary and conclusions

This dissertation is focused on fundamental nanotribological studies on 2D materials and their van der Waals heterostructures. Friction force measurements were conducted with FFM in UHV on epitaxial graphene on SiC(0001) and on heterostructures of MoS_2 on epitaxial graphene on SiC(0001), graphene on hBN, and $MoSe_2$ on hBN. The application of multiple AFM techniques and a novel navigational microstructure allowed for precise localization and identification of each material. The influence of contact pressure, bias voltage, number of molecular layers and roughness on frictional properties of 2D materials was investigated. The experiments and simulations performed in this work expanded the understanding of nanoscale friction phenomena on 2D materials.

7.1 Friction transition by pressure-induced covalent bonds on graphene

Preliminary experimental observations of superlinear increase of friction force as a function of normal load exhibited by monolayer epitaxial graphene on SiC(0001) [79] were systematically replicated and extended in this work. Simulations based on the DFTB method confirmed a corresponding contact pressure dependence of shear stress and elucidated the physical mechanism behind this phenomenon. The calculations demonstrated that, above a contact pressure threshold between 10 to 12.5 GPa, the graphene layer undergoes change from sp^2 to sp^3 hybridization. The so-called diamene forms covalent bonds with the carbon buffer layer below and the SiO_x counter surface. The bond formation results in a significant, more than one order, increase in shear stress and in a shift of the shear plane from the graphene interface into SiO_x. This explanation is supported by other findings. First, the calculation based on the Hertz contact mechanic model proves that the AFM tip is sharp enough to induce sufficiently high contact pressure. Second, the contact pressure threshold of 12.5 GPa reaches the expected yield strength of silicon oxide [112, 113]. Reaching the contact pressure threshold leads to plastic deformation and flattening of the SiO_x tip, which were demonstrated experimentally as the increase in the transition normal load threshold and as fluctuations in friction force results. Third, the decrease of conductivity, caused by the increasing number of sp^3 bonds and by tip deformations, was also observed in AFM experiments. A similar friction force trend was measured both for SiO_x and diamond AFM tips. The SiO_x tips are too soft to wear the ultra-hard diamene, while this is possible with diamond tips. Next to dissipation in elastic instabilities and in wear processes, the simultaneous formation of covalent bonds with the SiO_x tip surface and the underlying SiC interface layer establishes a third mechanism limiting the ultra-low friction on epitaxial graphene.

7.2 Flexural compliance and friction in van der Waals heterostructures

The modification of epitaxial graphene on SiC(0001) by deposition of MoS_2 layers via CVD method results in the growth of triangular flakes of MoS_2 and, effectively, the formation of MoS_2/graphene van der Waals heterostructures. Substrate and heterostructure surfaces were identified by a combination of topography and work function results. The work function of a single layer of MoS_2 is -242 mV with respect to graphene/SiC(0001) and is increasing with

increasing number of MoS_2 layers. Incommensurability and weak van der Waals interactions between MoS_2 flakes and the graphene layer allow for an easy manipulation of the flakes' position and orientation in the superlubric regime, by the means of the AFM tip. The AFM experiments on MoS_2 flakes, which were locked to topographic features, show that friction decreases with an increasing number of layers of MoS_2. The load dependence of the friction force on MoS_2/graphene heterostructures is sublinear. The DMT contact mechanic model was fitted to parametrize the experimental observations. The tip-layer adhesion decreases strongly with the increasing number of MoS_2 layers, which leads to the decrease in friction force. Due to a stronger interaction between MoS_2 and SiO_x tip compared to MoS_2 and graphene, the MoS_2 flake deforms out of plane to conform to the AFM tip shape. This deformation leads to an increased real contact area, which results in the increased adhesion. An increasing number of MoS_2 layers causes an increase in bending rigidity of the flake, which reduces out-of-plane deformations. A bias voltage which compensates the work function difference at U_{CPD} reduces friction. Deviations in bias from U_{CPD} increase the shear stress and slightly decrease adhesion. It is important to note, that the bias voltage does not increase electrostatic adhesion but, enhances the atomic potential corrugation of the MoS_2/SiO_x interface by polarization. The electric conductivity of the MoS_2/graphene heterostructures is based on the tunneling current and decreases with the increasing number of layers. The tunneling current increases with increasing normal load probably due to a variation of the contact area and modulation of the Schottky barrier with increasing pressure. Comparison between experiments with conducting and insulating tips demonstrates that the influence of bias voltage strongly depends on the conductivity of both contacting surfaces and can become negligible when the tip carries an oxide layer of several nanometers of thickness.

7.3 Advancing the investigation of stacked van der Waals heterostructures

The stacking of exfoliated 2D materials opens new possibilities to form heterostructures in an easy way for a large variety of combinations. Current stacking techniques result in poorly defined sample surfaces, which, depending on the measurement technique, renders heterostructures inaccessible. A navigational microstructure was designed and fabricated on SiO_x substrates to mitigate this disadvantage of exfoliated heterostructures and to make studies on them interoperable between various scientific devices. Heterostructures of graphene/hBN and $MoSe_2$/hBN were stacked on the SiO_x substrate with navigational microstructure from exfoliated 2D materials. Operationality of the navigational microstructure was demonstrated by the localization of heterostructures in UHV-AFM. AFM imaging assisted by KPFM allowed the identification of all respective surfaces. Measurements of the friction force as a function of normal load show very similar numbers for the graphene/hBN heterostructure and for the pristine hBN beneath. The similarity can be explained by an enhancement of the atomic potential corrugation between graphene and the tip by the local dipoles of the hBN beneath. Friction force measurements on bare hBN indicate that hBN exhibits rehybridization under high pressure similarly to monolayer epitaxial graphene on SiC(0001). The heterostructure of $MoSe_2$/hBN shows higher friction than the pristine hBN beneath, comparable to the difference between MoS_2/graphene heterostructures and epitaxial graphene. The fitting of the DMT

contact mechanic model reveals that adhesion on both heterostructures is increased, while it is negligible on pristine hBN. This finding resembles those for the MoS_2/graphene heterostructure and indicates the role of out-of-plane deformations for thin graphene and $MoSe_2$ layers, which increase friction. In comparison to atomically flat SiC(0001), the SiO_x substrate roughness limits the atomic smoothness of stacked 2D materials. This in turn prevents observation of the expected formation of the moiré superstructure. The increased surface roughness disturbed the compliance between graphene and hBN, which increased the transition normal load threshold and prevented observation of the contact pressure-induced rehybridization of graphene/hBN heterostructure.

7.4 Conclusions for application

With the progressing miniaturization of devices, the impact of nanotechnology on everyday life will continue to increase. The longevity and reliability of MEMS and NEMS are of increasing importance. This dissertation demonstrates that the nanotribological properties of 2D materials are suitable for application as solid lubricants in nanodevices. The ultra-low friction of monolayer epitaxial graphene on SiC(0001) is guaranteed in a vacuum until the contact pressure reaches the rehybridization threshold. Even this limitation can be an advantage because it still allows wearless moderation of the friction. The ultra-hard diamene, formed from the graphene above the threshold contact pressure, prevents the wear of the 2D material unless the counter interface is of similar hardness. Connecting surfaces with two incommensurate coatings such as graphene and MoS_2 allow virtually frictionless movement based on structural superlubricity. The friction on a van der Waals heterostructure of MoS_2 and graphene can be designed based on the number of layers and then tuned by the application of a bias voltage. Exfoliated 2D materials exhibit similar properties as their counterparts produced with epitaxy methods, but give freedom of choice in substrate, combination and orientation of each layer within the van der Waals heterostructures. The navigational microstructures introduced in this work can mitigate some disadvantages related to the exfoliation techniques and facilitate the fabrication and further research on new 2D materials. This dissertation expands the understanding of nanoscale friction phenomena on 2D materials.

Appendices

Appendix I MatLAB script to calculate friction

Analysis of measured data was automatized by scripts written in MatLAB. The MatLAB environment was chosen due to the already existing library for .sxm files produced by AFM software nanonis [139]. This library was made by Quentin Peter as a part of his master thesis and was distributed under the GNU General Public License, Version 3.0. The script prepared by the author of this work was used for all friction and current experiments presented in this dissertation. The script is included below.

```
clear all;
close all;
clc;
disp('STARTED');
disp('Loading setup parameters');
%Setup
%Direction of background file - loading only .sxm files
backgdir = dir('...\AFM\LFM\background\*.sxm');
%Direction of data file folder - loading only .sxm files
datafolder = dir('...\AFM\LFM\*.sxm');
%Name of Excel Sheet
filenamexls = 'sampleID_CantileverID_Date_ExperimentTyp_SeriesNo_SlidingVelocity_...
...ElectricBias_ScriptVersion.xlsx'; %Experiment parameters - Calibration of cantilever
   f=15530.3513;                %resonance frequency [Hz]
   l=450E-6;                    %length [m]
   t=7.23*0.0001*f*l*l;         %thickness [m]
   w=50E-6;                     %mean width [m]
   ht=15E-6;                    %tip height [m]
   h=ht+t/2;                    %effective height [m]
   SiPoisson=0.278;             %Si Poisson ratio
   E=1.69E+11;                  %Si Young modulus
   G=E/(2*(1+SiPoisson));       %Si Shear modulus
   Kn=E*w*t*t*t/(4*l*l*l);      %normal stiffness
   Sn=107.4;                    %normal sensitivity
   Cn=Kn*Sn;                    %normal calibration coefficient (can be used to calculate a normal
load if the vertical signal was recorded in V)
   Kt=G*w*(t^3)/(3*h*h*l);      %torsional stiffness
   St=(Sn*3*h)/(2*l);           %torsional sensitivity
   gain=64/20;                  %lateral signal gain
   Ct=St*Kt/gain;               %torsional calibration coefficient
   startoffset=-4.11;           %value of vertical(normal force) offset just before the beginning
of experimental series [V(nN)]
```

```
   endoffset=-4.075;                %value of vertical(normal force) offset just after the end of
experimental series [V(nN)]
   withbackground=0;                %background measurements were done after (0) or before
(1) FS test
   additional=0;                %number of additional scans done during experimental series
   %Load Data:
%background:
if withbackground==1
   disp('Loading background data');
   backgname = backgdir.name;                %load background file name
   Tbackg= sxm.load.loadProcessedSxM(backgname);                %load background data
   backgtrace=Tbackg.channels(5).rawData;                %load friction trace signal
   backgretrace=Tbackg.channels(6).rawData;                %load friction retrace signal
   %calculation of background friction force for each point
   backg=(((backgtrace-backgretrace)/2)*Ct);
   meanbackg=mean(backg,'all','omitnan');
else
   meanbackg=0;
end
%data files
%chronological sorting of data files
[~,index] = sortrows({datafolder.date}.'); datafolder = datafolder(index); clear index;
numfiles = length(datafolder);                %number of files (measurements)
%average change in vertical offset between each measurements
offsetstep=(startoffset-endoffset)/(numfiles+withbackground+additional);
NOinc=0;                %declaration number of measurements with increasing normal load
NOdec=0;                %declaration number of measurements with decreasing normal load
NOstab=0;                %declaration number of measurements with stabilising the position or
others.
disp('Analysing Data');
for i = 1:numfiles
   filename = datafolder(i).name;                %Load Data file name
   T1= sxm.load.loadProcessedSxM(filename);                %Load Data file
   FTtrace=T1.channels(5).rawData;                %Load Friction Trace signal
   FTretrace=T1.channels(6).rawData;                %Load Friction Retrace signal
   Itrace=T1.channels(9).rawData;                %Load Current Trace signal
   Iretrace=T1.channels(10).rawData;                %Load Current Retrace signal
   %calculation of friction force value for each point
   FT=(((FTretrace-FTtrace)/2))*Ct-meanbackg;
   %calculation of average current value for each point
   I=((Iretrace+Itrace)/2);
   %reading data from file name
%changing '_' to space
```

```
for j=1:length(filename)
   if filename(j)=='_'
   filename(j)=' ';
   end
end
stringname=string(filename);
stringname=split(stringname);                %cuting name into seperate parts
load=char(stringname(5));                    %reading normal load from the name
direction=stringname(6);                     %reading monotonicity from the name (need to be checked
before activation of the script)
dirNo=0;                  %declaration of direction:,(0) stabilising, (1) increasing, (2) decresing,
if direction=="inc"                  %determination of direction
   dirNo=1;
   NOinc=NOinc+1;
elseif direction=="dec"
   dirNo=2;
   NOdec=NOdec+1;
else
   NOstab=NOstab+1;
end
numload=load(1:length(load)-2);                  %normal load from the name
%creating an array of results for both directions of load change
NO=i;                  %chronological number of measurement in experiment
if dirNo==1                  %array for results with increasing load
   resultsInc(i,1) = NO;
   %calculated normal load
   resultsInc(i,2) = str2double(string(numload))*Cn/1000+(offsetstep*(i-1))*Cn/1000;
   resultsInc(i,3) = mean(FT,'all','omitnan');                  %mean friction force column
   resultsInc(i,4) = (std(FT,1,'all','omitnan'));                  %error of friction force column
   resultsInc(i,5) = mean(I,'all','omitnan');                  %mean current column
   resultsInc(i,6) = (std(I,1,'all','omitnan'));                  %error of current column
%array for results with decreasing load;all parameters analogical as above
elseif dirNo==2
   resultsDec(1+NOstab+NOinc-NOdec,1) = NO;
   resultsDec(1+NOstab+NOinc-NOdec,2) = str2double(string(numload))*Cn/1000+(offsetstep*(i-
   1)*Cn/1000);
   resultsDec(1+NOstab+NOinc-NOdec,3) = mean(FT,'all','omitnan');
   resultsDec(1+NOstab+NOinc-NOdec,4) = (std(FT,1,'all','omitnan'));
   resultsDec(1+NOstab+NOinc-NOdec,5) = mean(I,'all','omitnan');
   resultsDec(1+NOstab+NOinc-NOdec,6) = (std(I,1,'all','omitnan'));
end
end
disp('Data Analysis Complete');
```

```
%Write all data to Excel File
disp('Writing Excel File');
%type of data in column
variabletypes = 'double','double','double','double','double','double';
%name of column
variablenames = 'No.','normal load','friction force','friction force error','current','current error';
%create table for results with increasing load
TabInc = array2table(resultsInc,'VariableNames',variablenames);
%create table for results with decreasing load
TabDec = array2table(resultsDec,'VariableNames',variablenames);
%write table for results with increasing load
writetable(TabInc,filenamexls,'Sheet','Fl(Fn)','Range','A1');
%write table for results with decreasing load
writetable(TabDec,filenamexls,'Sheet','Fl(Fn)','Range','G1');
disp('DONE');
```

Appendix II Supplementary Informations to chapter 4

Analysis of changes in stick-slip pattern for diamond tip

The rupture of graphene can be recognized by the significant change in the friction loop (figures A1). For both instances when the graphene was ruptured with a diamond tip, the stick-slip pattern registered before the rupture changed into a loop with large amplitude (figures A1b) and A1d)). In both cases, the rupture occurred during the scan. This required to calculate friction separately for areas before and after the rupture because the overall average value will not show exact information.

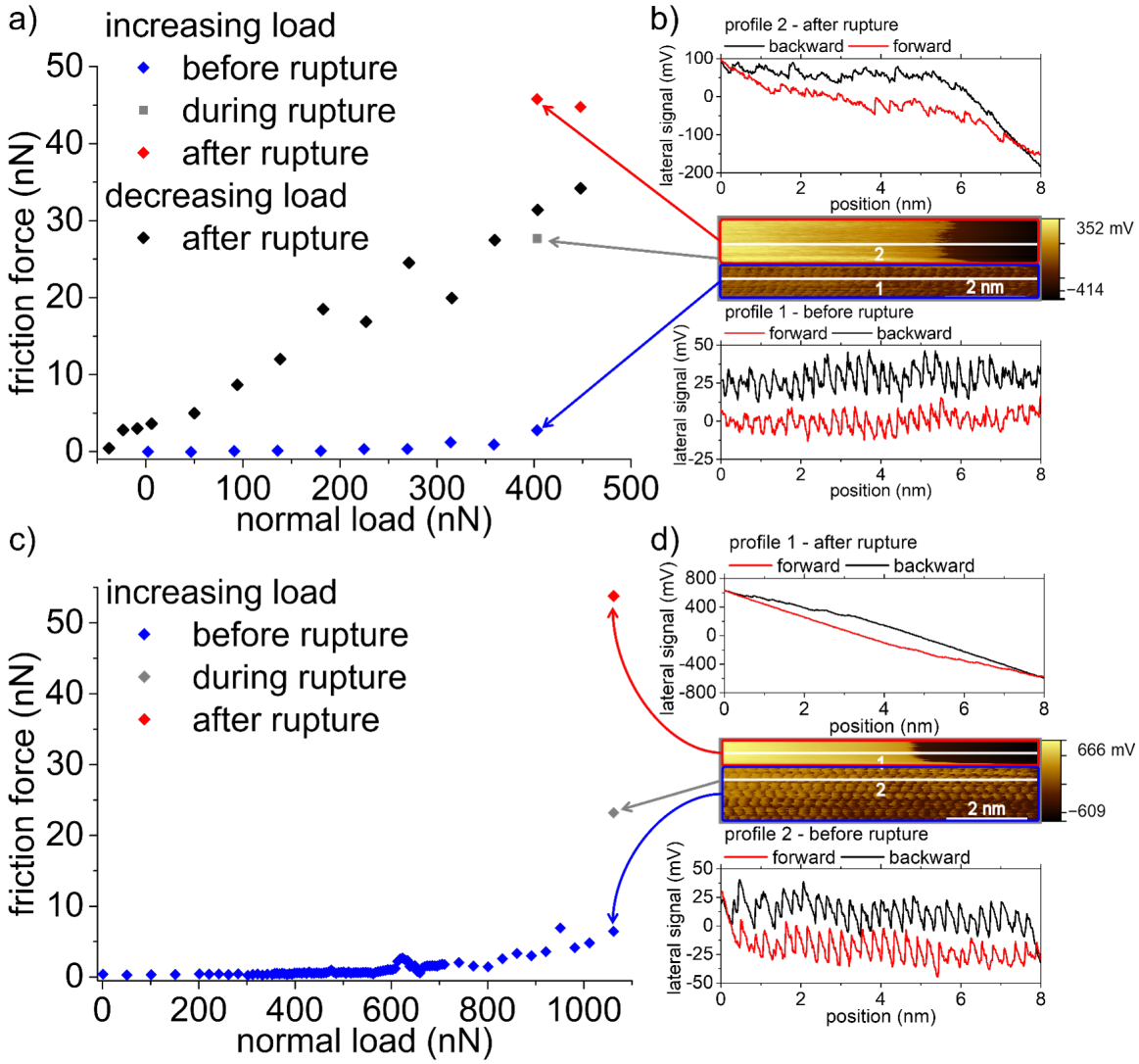

Figure A1: Changes in lateral force signal during ruptures of graphene: a) the plot of first rupture from figure 4.7b); b) lateral force signal before and after the first rupture of graphene; c) the plot of the second rupture from figure 4.8b); d) lateral force signal before and after the second rupture of graphene.

DFTB versus DFT

Although previous simulations of similar tribological systems show the robustness and efficiency of the density-functional tight-binding method, the transferability of parameters need to be tested with relevant structures and reactions. Here we show results of DFTB and

first-principles DFT MD simulations of an amorphous silicon oxide (a-SiO_2) surface sliding against a graphene layer on a SiC(0001) surface and compare shear stresses and transition pressure from low- to high-friction regime.

First-principles DFT calculations were performed using the CP2K code [140, 141], where the mixed Gaussian Plane Wave (GPW) method was employed [142]. A plane wave cutoff of 500 Ry was chosen to define the grid spacing. The mapping of Gaussian basis set functions onto the CP2K reference grid was determined by a cutoff of 45 Ry. All calculations were performed within the Perdew-Burke-Enzerhof (PBE) approximation [143] to the exact exchange correlation functional. Gaussian double-zeta basis sets with polarization functions were used to expand the Kohn-Sham wave functions of the valence electrons [144] and Goedecker-Teter-Hutter pseudopotentials [145] were applied to effectively treat the core electrons. Periodic boundary conditions were imposed along all spatial directions. Due to high computational costs of the DFT MD simulations, their time scale was limited to 0.12 ns (shorter than those of the DFTB MD simulations). The shear stresses were averaged over the last 0.06 ns. Other details of the simulation, such as pressure coupling and Langevin thermostat, were the same as in the DFTB MD simulations (see Simulation Methods 3.5). For a fair comparison, we used the same a-SiO_2 configuration for both DFT and DFTB. Before simulations, the structure was optimized with each method.

Figures A2a) and A2b) show a final configuration after the 0.3- ns DFTB MD simulation at p = 5 GPa and a comparison of the shear stresses as a function of the contact pressure between DFT and DFTB, respectively. The DFTB results are in good agreement with the DFT results regarding both the shear stress at each contact pressure and the transition pressure. The a-SiO2 surface configuration which was uses in this comparison had a higher density of OH groups on the surface and thus a lower reactivity. It therefore exhibits a higher transition pressure (17.5 GPa) than those reported in the main text (figure 4.9) for more reactive surface configurations. This comparison confirms the transferability of DFTB results to the systems considered in this study.

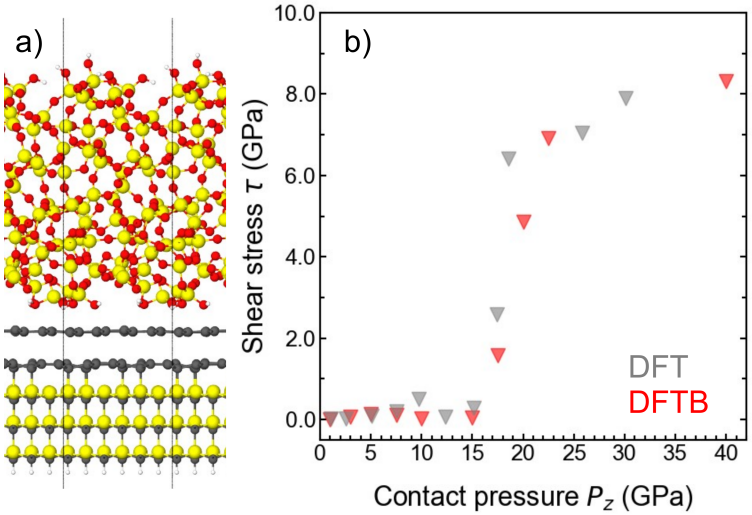

Figure A2: Comparison of shear stresses obtained from DFT and DFTB MD sliding simulations with varying contact pressures: a) final configuration of the 0.3-ns DFTB MD simulation at P = 5 GPa; b) shear stresses as a function of the contact pressure for DFT (gray) and DFTB (red). The figure is adopted from Ref. [1].

Coordination of C-C and C-O or C-Si bonds

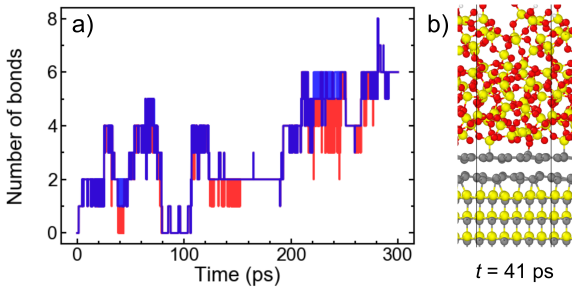

Figure A3: a) Number of bonds between Si or O and a C-atom of the graphene layer versus simulated time. Blue color indicates the total number of Si-C and O-C bonds, red color indicates the number of Si-C and O-C bonds where the C atom is in a nearest-neighbor position to a sp^3-bonded C atom of the graphene. Most bonds are formed as pairs in the sp^3 hybridization; b) Two examples for exceptional isolated bonds. The Si-C bond is formed with an undercoordinated, reactive silicon atom. The C-O bond appears isolated because the ongoing shear has stretched the C-C distance for the nearest neighbor beyond the limit considered as C-C bond. The figure is adopted from Ref.[1].

Plastic events in a SiO_2 matrix during sliding

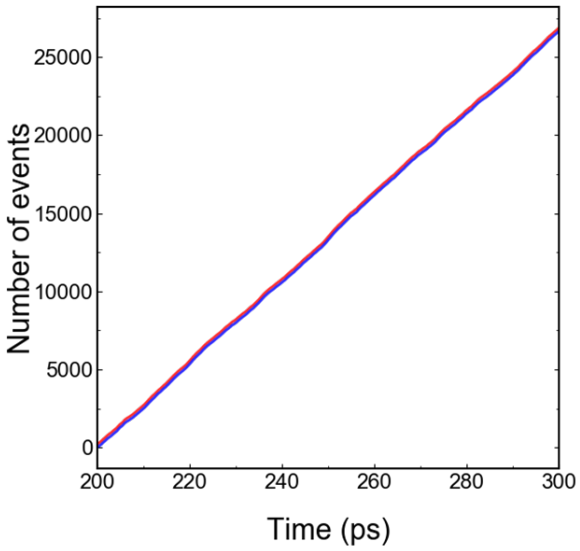

Figure A4: Number of bond-formation (blue) and -breaking events (red) in a SiO_2 matrix under sliding at τ = 300 K and P_Z = 20 GPa. The high friction at high pressures is attributed to these plastic events (breaking and formation of Si-O bonds). The figure is adopted from Ref. [1].

High shear stresses at high normal pressures are attributed to bond-breaking events inside the SiO_2 layer. In this high-friction regime, the SiO_2 matrix deforms plastically. The figure A4 shows the number of bond-formation (blue) and -breaking events (red) under shear at T = 300 K and P_Z = 20 GPa, and that the rate of plastic events is constant. This shear accommodation inside the SiO_2 matrix observed in our simulations is not comparable with plastic deformation of the tip apex in the experiments (resulting in a change of the tip apex). This shear accommodation in SiO_2 would cause damage/wear of the tip or graphene or irreversible sp^2-to-sp^3 transition in graphene. The reduction of the sharpness of the tip mitigates entering the "wear" regime. Thus it is expected that one needs a sharper and harder AFM tip (like a diamond tip) to enter the "wear" regime.

Velocity dependence of transition pressure

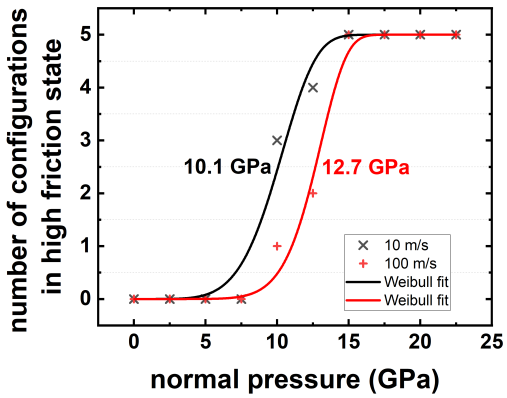

Figure A5: Velocity dependence of the transition from low-friction regime to high-friction regime. The number of configurations in high-friction regime, i.e. with at least one chemical bond between graphene and silicon oxide, is plotted as function of the normal pressure. Weibull sigmoid functions have been fitted to determine the transition pressure at 50% level. Results are presented for simulations at 10 m/s (3 ns) and at 100 m/s (0.3 ns) for a temperature of 300 K. The figure is adopted from Ref. [1].

Temperature dependence

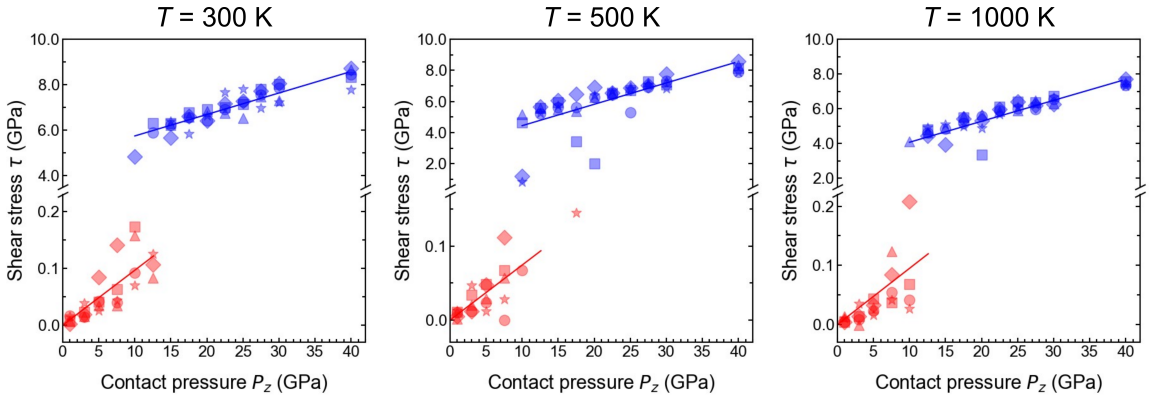

Figure A6: Shear stress versus contact pressure for five different silicon oxide configurations. Red symbols indicate absence of chemical bonds between graphene and silicon oxide atoms, blue symbols indicate the formation of at least one such chemical bond between a carbon atom and a silicon or oxygen atom. Simulations were performed for T = 300 K (left), 500 K (middle), and 1000 K (right). The sliding distance was 30 nm and the sliding speed 100 m/s. Symbols are the same as in Fig. 2. The figure is adopted from Ref.[1].

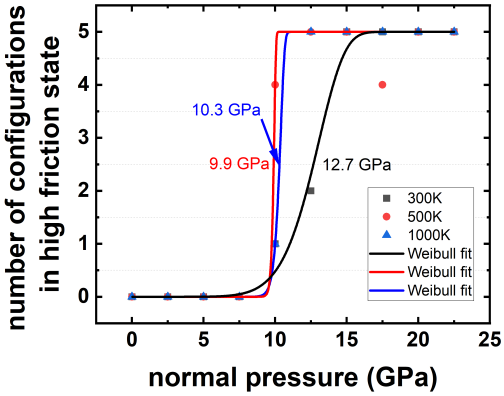

Figure A7: Temperature dependence of the transition from low-friction regime to high-friction regime. The number of configurations in high-friction regime, i.e. with at least one chemical bond between graphene and silicon oxide, is plotted as function of the normal pressure. Weibull sigmoid functions have been fitted to determine the transition pressure at 50% level. Results are presented for simulations at 100 m/s at three different temperatures (0.3 ns). The figure is adopted from Ref. [1].

Correlation of the number of bonds with the contact pressure

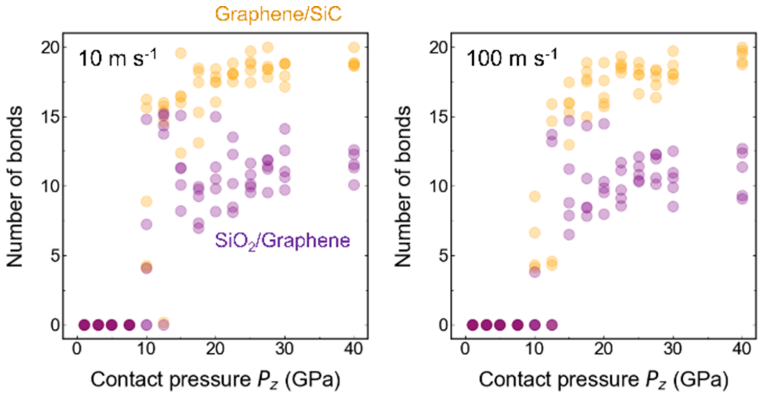

Figure A8: Number of chemical bonds as a function of the contact pressure: at sliding speeds of 10 m/s (left) and 100 m/s (right). Yellow symbols represent C-C bonds between graphene and SiC, purple symbols C-O and C-Si bonds between graphene and silicon oxide. The data represents simulation results for five different silicon oxide configurations at a sliding velocity of 10 (left) and 100 m/s (right) (temperature 300 K). The figure is adopted from Ref.[1].

Shear stress as function of the number of chemical bonds

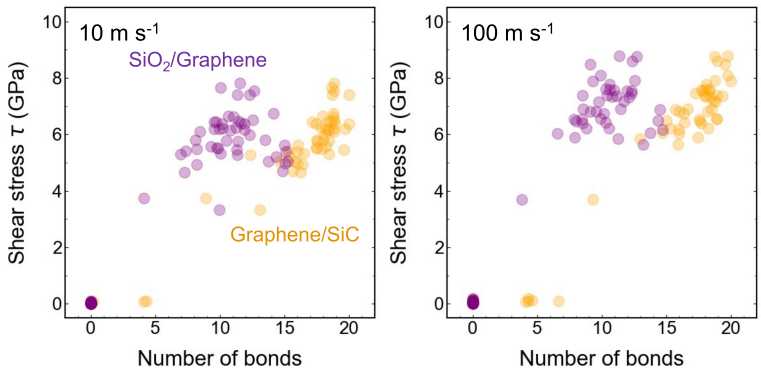

Figure A9: Shear stress as function of the number of chemical bonds. Yellow symbols represent C-C bonds between graphene and SiC, purple symbols C-O and C-Si bonds between graphene and silicon oxide. Data represent simulation results for five different silicon oxide configurations at a sliding velocity of 10 (left) and 100 m/s (right) (temperature 300 K, contact pressures between 1 and 40 GPa as indicated in figure 4.9b)). Note that the formation of C-C bonds alone does not necessarily lead to high shear stress. The figure is adopted from Ref.[1].

Quantitative model to compare simulated shear stress and measured friction force

A quantitative comparison of simulated shear stress and measured friction force requires a contact mechanics and a friction model. The simplest approach is to integrate the simulated shear stress over the contact area using the contact pressure distribution predicted by the Hertz model.

$$F_L = \int_0^a \left(p_0 \sqrt{1 - \frac{r^2}{a^2}} \right) 2\pi r dr \tag{A1}$$

and to approximate the simulated shear stress $\sigma(p)$ by two linear functions below and above the threshold. These linear functions were fitted to the DFTB results for a temperature of 300 K and a sliding velocity of 10 m/s with a transition pressure of 10 GPa. Figure A10 confirms that the friction force microscopy results are in good agreement with this simple contact mechanics and friction model with respect to the transition force.

Interestingly, the experiments exhibit strong scatter while our simple model predicts a smooth $F_L(F_N)$ curve. We attribute this scatter to plastic deformation and atomic rearrangements at the surface of the silica tip. Furthermore, experimental results in the high-friction regime are far lower than the values predicted by the model. Such discrepancies can be expected because of three differences between experiment and simulation. First, the sliding velocity is orders of magnitude lower in the experiment. Reducing the simulation velocity is limited by the computational resources available. We have simulated results for 300 K also at a ten times lower velocity and found that the transition to the high-friction regime proceeds at lower contact pressures of 10 GPa, and that the shear stresses at 15 GPa contact pressure are reduced by 35%. Similarly, the shear stress is reduced when simulating at higher temperatures of 500 K or 1000 K. An extrapolation of shear stresses based on an Arrhenius-type model will create a closer match of friction values and experiment. However, the effective masses of the dynamic system and its elastic coupling differ between simulation and experiment, resulting in an unknown difference in the attempt frequency of the Arrhenius model. This problem typically forecloses

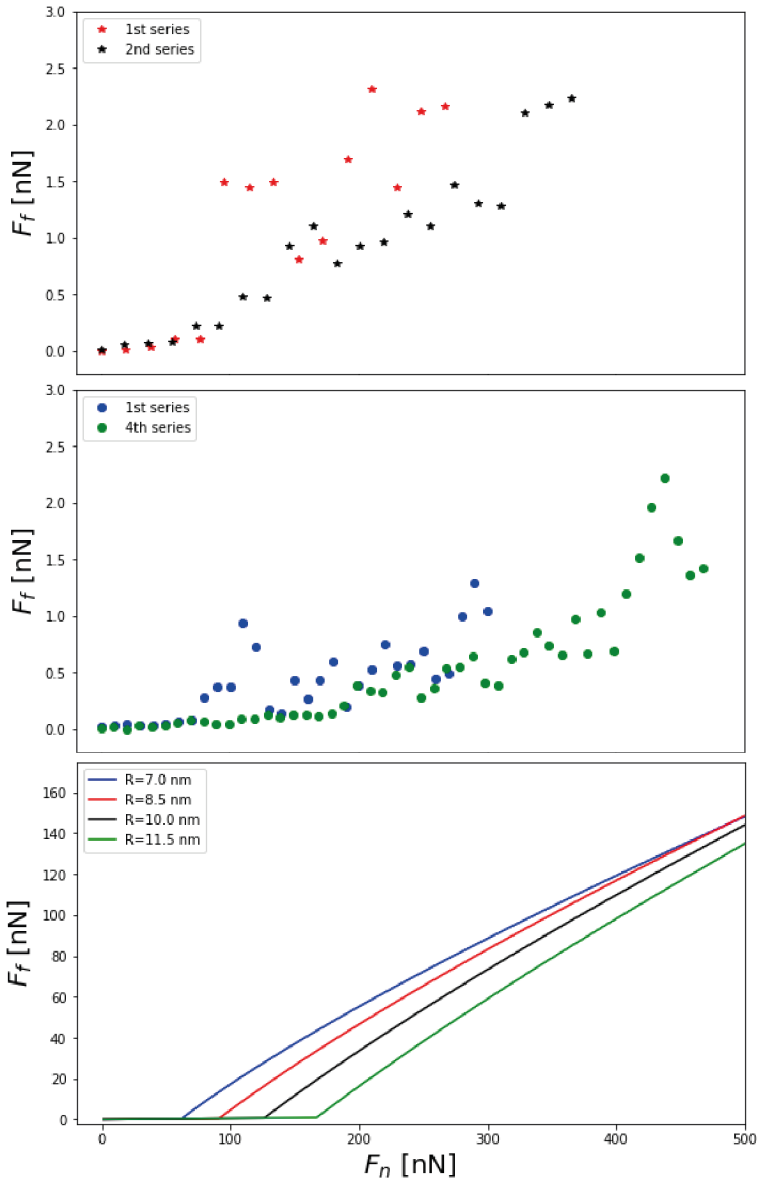

Figure A10: Quantitative model to compare simulated shear stress and measured friction force. Comparison of the experimental friction vs. load data from figures 4.1b) and 4.3 with a simple contact mechanics and friction model based on the DFTB simulation results at 300 K, 10 m/s. See text for details. The figure is adopted from Ref.[1].

direct comparison of molecular dynamics simulations and friction force microscopy results. The second difference between simulation and experiment is the flattening of the AFM tip due to plastic deformation. A flattening of the tip shape results in lower contact pressure at the same loading force. Since the yield strength of silicon oxide is of the same order as the threshold pressure for bond formation on graphene/SiC(0001), the experimental contact will not enter fully into the high-friction regime which is predicted by the simulation of flat contacts with periodic lateral boundary conditions. The third difference results from the predicted shear stress in the high-friction regime which depends critically on the yield stress of the material at the tip apex. This yield stress is expected to decrease with decreasing density of the silica and increasing hydrogen contents, parameters which are not know for our micro-fabricated AFM tip.

References

[1] B. Szczefanowicz, T. Kuwahara, T. Filleter, A. Klemenz, L. Mayrhofer, R. Bennewitz and M. Moseler. Formation of intermittent covalent bonds at high contact pressure limits superlow friction on epitaxial graphene. *Physical Review Research*, 5(1):L012049, 2023.

[2] Z. Liu, B. Szczefanowicz, J. M. J. Lopes, Z. Gan, A. George, A. Turchanin and R. Bennewitz. Nanoscale friction on MoS_2/graphene heterostructures. *Nanoscale*, 15(12):5809–5815, 2023.

[3] K. Holmberg and A. Erdemir. Influence of tribology on global energy consumption, costs and emissions. *Friction*, 5(3):263–284, 2017.

[4] P. Jost. Lubrication (Tribology) - A report on the present position and industry's needs. Report, Department of Education and Science, HM Stationary Office, London, UK, 1966.

[5] B. N. J. Persson and E. Tosatti. Layering transition in confined molecular thin films: Nucleation and growth. *Physical Review B*, 50(8):5590–5599, 1994.

[6] J. Gao, W. D. Luedtke and U. Landman. Layering Transitions and Dynamics of Confined Liquid Films. *Physical Review Letters*, 79(4):705–708, 1997.

[7] B. N. J. Persson and P. Ballone. Squeezing lubrication films: Layering transition for curved solid surfaces with long-range elasticity. *The Journal of Chemical Physics*, 112(21):9524–9542, 2000.

[8] N. Manini, G. Mistura, G. Paolicelli, E. Tosatti and A. Vanossi. Current trends in the physics of nanoscale friction. *Advances in Physics: X*, 2(3):569–590, 2017.

[9] P. C. Uzoma, H. Hu, M. Khadem and O. V. Penkov. Tribology of 2D Nanomaterials: A Review. *Coatings*, 10(9):897, 2020.

[10] B. R. Manu, A. Gupta and A. H. Jayatissa. Tribological Properties of 2D Materials and Composites–A Review of Recent Advances. *Materials*, 14(7):1630, 2021.

[11] U. Beerschwinger, D. Mathieson, R. L. Reuben and S. J. Yang. A study of wear on MEMS contact morphologies. *Journal of Micromechanics and Microengineering*, 4(3):95, 1994.

[12] J. Pu, Y. Mo, S. Wan and L. Wang. Fabrication of novel graphene–fullerene hybrid lubricating films based on self-assembly for MEMS applications. *Chemical Communications*, 50(4):469–471, 2014.

[13] H. A. Zaharin, M. J. Ghazali, N. Thachnatharen, F. Ezzah, R. Walvekar and M. Khalid. Progress in 2D materials based Nanolubricants: A review. *FlatChem*, 38:100485, 2023.

[14] E. Meyer, R. Overney, K. Dransfeld and T. Gyalog. *Nanoscience: Friction And Rheology On The Nanometer Scale*. World Scientific, Singapore, 1998.

[15] G. Steindorff. *Das Grab des Ti. Veröffentlichungen der Ernst-von-Sieglin-Expedition*. JC Hinrichs' sche Buchhandlung Leipzig, 1913.

[16] A. H. Layard. *Chapter V*, in book Discoveries in the ruins of Nineveh and Babylon: with travels in Armenia, Kurdistan, and the Desert: being the result of a second expedition undertaken for the trustees of the British Museum. Harper & Brothers, 80–113, 1859.

[17] J. Li, H. Chen and H. A. Stone. Ice lubrication for moving heavy stones to the Forbidden City in 15th- and 16th-century China. *Proceedings of the National Academy of Sciences*, 110(50):20023–20027, 2013.

[18] L. da Vinci. Codex Arundel. 1478-1518. *MSS British Library, London, UK*.

[19] A. A. Pitenis, D. Dowson and W. Gregory Sawyer. Leonardo da Vinci's Friction Experiments: An Old Story Acknowledged and Repeated. *Tribology Letters*, 56(3):509–515, 2014.

[20] D. Dowson. Men of Tribology: Leonardo da Vinci (1452–1519). *Journal of Lubrication Technology*, 99(4):382–386, 1977.

[21] G. Amontons. De la Résistance Causé dans les Machines. *Mémoires de l'Académie Royale des Sciences A*, pages 206–226, 1699.

[22] D. Dowson. Men of tribology: Guillaume Amontons (1663–1705) and John Theophilus Desaguliers (1683–1744). *Journal of Lubrication Technology*, 100(2):455–7, 1978.

[23] L. Euler. Sur la diminution de la résistance du frottement. *Mémoires de l'académie des sciences de Berlin*, pages 133–148, 1750.

[24] C. A. Coulomb. Théorie des machines simples: en ayant égard au frottement de leurs parties, et à la roideur de cordages. *Mémoires de mathématique et de physique, presentés à l'Académie royale des sciences, par divers sçavans & lûs dans ses assemblées*, 10:161–331, 1785.

[25] D. Dowson. Men of Tribology: Charles Augustin Coulomb (1736–1806) and Arthur-Jules Morin (1795–1880). *Journal of Lubrication Technology*, 100(2):148–155, 1978.

[26] J. T. Desaguliers. *A Course of Experimental Philosophy, 2 Volumes*. London, 1734.

[27] F. Bowden and D. Tabor. *The Friction and Lubrication Oil Solids*. Oxford University Press, London, 1950.

[28] G. Binnig, C. F. Quate and C. Gerber. Atomic Force Microscope. *Physical Review Letters*, 56(9):930–933, 1986.

[29] L. Prandtl. Ein Gedankenmodell zur kinetischen Theorie der festen Körper. *ZAMM - Journal of Applied Mathematics and Mechanics / Zeitschrift für Angewandte Mathematik und Mechanik*, 8(2):85–106, 1928.

[30] V. L. Popov and J. A. T. Gray. Prandtl-Tomlinson model: History and applications in friction, plasticity, and nanotechnologies. *ZAMM - Journal of Applied Mathematics and Mechanics / Zeitschrift für Angewandte Mathematik und Mechanik*, 92(9):683–708, 2012.

[31] G. A. Tomlinson. CVI. A molecular theory of friction. *The London, Edinburgh, and Dublin Philosophical Magazine and Journal of Science*, 7(46):905–939, 1929.

[32] U. D. Schwarz and H. Hölscher. Exploring and Explaining Friction with the Prandtl–Tomlinson Model. *ACS Nano*, 10(1):38–41, 2016.

[33] B. Persson. *Sliding Friction: Physical Principles and Applications*. Springer Science & Business Media, 2000.

[34] C. M. Mate, G. M. McClelland, R. Erlandsson and S. Chiang. Atomic-scale friction of a tungsten tip on a graphite surface. *Physical Review Letters*, 59(17):1942–1945, 1987.

[35] M. Hirano and K. Shinjo. Atomistic locking and friction. *Physical Review B*, 41(17):11837–11851, 1990.

[36] M. Hirano and K. Shinjo. Superlubricity and frictional anisotropy. *Wear*, 168(1):121–125, 1993.

[37] M. Hirano, K. Shinjo, R. Kaneko and Y. Murata. Observation of Superlubricity by Scanning Tunneling Microscopy. *Physical Review Letters*, 78(8):1448–1451, 1997.

[38] M. Dienwiebel, G. S. Verhoeven, N. Pradeep, J. W. M. Frenken, J. A. Heimberg and H. W. Zandbergen. Superlubricity of graphite. *Physical Review Letters*, 92(12), 2004.

[39] K. S. Novoselov, A. K. Geim, S. V. Morozov, D. Jiang, Y. Zhang, S. V. Dubonos, I. V. Grigorieva and A. A. Firsov. Electric Field Effect in Atomically Thin Carbon Films. *Science*, 306(5696):666–669, 2004.

[40] The Nobel Prize in Physics 2010. *NobelPrize.org. Nobel Prize Outreach AB 2023*, (https://www.nobelprize.org/prizes/physics/2010/summary/), [access on: 12 Jun 2023].

[41] A. K. Geim and I. V. Grigorieva. Van der Waals heterostructures. *Nature*, 499(7459):419–425, 2013.

[42] K. S. Novoselov, A. Mishchenko, A. Carvalho and A. H. Castro Neto. 2D materials and van der Waals heterostructures. *Science*, 353(6298):aac9439, 2016.

[43] D. Berman, A. Erdemir and A. V. Sumant. Graphene: a new emerging lubricant. *Materials Today*, 17(1):31–42, 2014.

[44] G.-H. Lee, R. C. Cooper, S. J. An, S. Lee, A. van der Zande, N. Petrone, A. G. Hammerberg, C. Lee, B. Crawford, W. Oliver, J. W. Kysar and J. Hone. High-Strength Chemical-Vapor-Deposited Graphene and Grain Boundaries. *Science*, 340(6136):1073–1076, 2013.

[45] O. Hod, E. Meyer, Q. Zheng and M. Urbakh. Structural superlubricity and ultralow friction across the length scales. *Nature*, 563(7732):485–492, 2018.

[46] Z. Liu, J. Yang, F. Grey, J. Z. Liu, Y. Liu, Y. Wang, Y. Yang, Y. Cheng and Q. Zheng. Observation of Microscale Superlubricity in Graphite. *Physical Review Letters*, 108(20):205503, 2012.

[47] Y. Song, D. Mandelli, O. Hod, M. Urbakh, M. Ma and Q. Zheng. Robust microscale superlubricity in graphite/hexagonal boron nitride layered heterojunctions. *Nature Materials*, 17(10):894–899, 2018.

[48] D. Berman, S. A. Deshmukh, S. K. R. S. Sankaranarayanan, A. Erdemir and A. V. Sumant. Macroscale superlubricity enabled by graphene nanoscroll formation. *Science*, 348(6239):1118–1122, 2015.

[49] J. M. Martin, C. Donnet, T. Le Mogne and T. Epicier. Superlubricity of molybdenum disulphide. *Physical Review B*, 48(14):10583–10586, 1993.

[50] H. P. Mungse and O. P. Khatri. Chemically Functionalized Reduced Graphene Oxide as a Novel Material for Reduction of Friction and Wear. *The Journal of Physical Chemistry C*, 118(26):14394–14402, 2014.

[51] B. Bhushan, T. Kasai, G. Kulik, L. Barbieri and P. Hoffmann. AFM study of perfluoroalkylsilane and alkylsilane self-assembled monolayers for anti-stiction in MEMS/NEMS. *Ultramicroscopy*, 105(1):176–188, 2005.

[52] Q. Li, X.-Z. Liu, S.-P. Kim, V. B. Shenoy, P. E. Sheehan, J. T. Robinson and R. W. Carpick. Fluorination of Graphene Enhances Friction Due to Increased Corrugation. *Nano Letters*, 14(9):5212–5217, 2014.

[53] A. P. M. Barboza, M. H. D. Guimaraes, D. V. P. Massote, L. C. Campos, N. M. Barbosa Neto, L. G. Cancado, R. G. Lacerda, H. Chacham, M. S. C. Mazzoni and B. R. A. Neves. Room-Temperature Compression-Induced Diamondization of Few-Layer Graphene. *Advanced Materials*, 23(27):3014–3017, 2011.

[54] A. P. M. Barboza, M. J. S. Matos, H. Chacham, R. J. C. Batista, A. B. de Oliveira, M. S. C. Mazzoni and B. R. A. Neves. Compression-Induced Modification of Boron Nitride Layers: A Conductive Two-Dimensiona BN Compound. *ACS Nano*, 12(6):5866–5872, 2018.

[55] M. Wolloch, G. Levita, P. Restuccia and M. C. Righi. Interfacial Charge Density and Its Connection to Adhesion and Frictional Forces. *Physical Review Letters*, 121(2):026804, 2018.

[56] A. Song, R. Shi, H. Lu, X. Wang, Y. Hu, H.-J. Gao, J. Luo and T. Ma. Fluctuation of Interfacial Electronic Properties Induces Friction Tuning under an Electric Field. *Nano Letters*, 22(5):1889–1896, 2022.

[57] J. F. Peng, F. P. Yang, K. Huang, H. Dong, S. A. Yan and X. J. Zheng. Friction behavior of monolayer molybdenum diselenide nanosheet under normal electric field. *Physics Letters A*, 384(7), 2020.

[58] H. J. Lang, Y. T. Peng, X. A. Cao and K. Zou. Atomic-Scale Friction Characteristics of Graphene under Conductive AFM with Applied Voltages. *ACS Applied Materials & Interfaces*, 12(22):25503–25511, 2020.

[59] K. Yu, K. Zou, H. Lang and Y. Peng. Nanofriction characteristics of h-BN with electric field induced electrostatic interaction. *Friction*, 9(6):1492–1503, 2021.

[60] F. Lavini, A. Calo, Y. Gao, E. Albisetti, T. D. Li, T. F. Cao, G. Q. Li, L. Y. Cao, C. Aruta and E. Riedo. Friction and work function oscillatory behavior for an even and odd number of layers in polycrystalline MoS_2. *Nanoscale*, 10(17):8304–8312, 2018.

[61] C. Lee, Q. Li, W. Kalb, X.-Z. Liu, H. Berger, R. W. Carpick and J. Hone. Frictional Characteristics of Atomically Thin Sheets. *Science*, 328(5974):76–80, 2010.

[62] Q. Li, C. Lee, R. W. Carpick and J. Hone. Substrate effect on thickness-dependent friction on graphene. *physica status solidi (b)*, 247(11-12):2909–2914, 2010.

[63] S. Li, Q. Li, R. W. Carpick, P. Gumbsch, X. Z. Liu, X. Ding, J. Sun and J. Li. The evolving quality of frictional contact with graphene. *Nature*, 539(7630):541–545, 2016.

[64] P. Huang, A. Castellanos-Gomez, D. Guo, G. Xie and J. Li. Frictional Characteristics of Suspended MoS_2. *The Journal of Physical Chemistry C*, 122(47):26922–26927, 2018.

[65] Z. Ye, A. Balkanci, A. Martini and M. Z. Baykara. Effect of roughness on the layer-dependent friction of few-layer graphene. *Physical Review B*, 96(11):115401, 2017.

[66] D. Andersson and A. S. de Wijn. Understanding the friction of atomically thin layered materials. *Nature Communications*, 11(1):420, 2020.

[67] K.-S. Kim, H.-J. Lee, C. Lee, S.-K. Lee, H. Jang, J.-H. Ahn, J.-H. Kim and H.-J. Lee. Chemical Vapor Deposition-Grown Graphene: The Thinnest Solid Lubricant. *ACS Nano*, 5(6):5107–5114, 2011.

[68] A. Klemenz, L. Pastewka, S. G. Balakrishna, A. Caron, R. Bennewitz and M. Moseler. Atomic Scale Mechanisms of Friction Reduction and Wear Protection by Graphene. *Nano Letters*, 14(12):7145–7152, 2014.

[69] A. Klemenz, A. Gola, M. Moseler and L. Pastewka. Contact mechanics of graphene-covered metal surfaces. *Applied Physics Letters*, 112(6), 2018.

[70] Z. Liu, J. G. Vilhena, A. Hinaut, S. Scherb, F. Luo, J. Zhang, T. Glatzel, E. Gnecco and E. Meyer. Moiré-Tile Manipulation-Induced Friction Switch of Graphene on a Platinum Surface. *Nano Letters*, 23(10):4693–4697, 2023.

[71] C. R. Stoldt, C. Carraro, W. R. Ashurst, D. Gao, R. T. Howe and R. Maboudian. A low-temperature CVD process for silicon carbide MEMS. *Sensors and Actuators A: Physical*, 97-98:410–415, 2002.

[72] K. V. Emtsev, A. Bostwick, K. Horn, J. Jobst, G. L. Kellogg, L. Ley, J. L. McChesney, T. Ohta, S. A. Reshanov, J. Rohrl, E. Rotenberg, A. K. Schmid, D. Waldmann, H. B. Weber and T. Seyller. Towards wafer-size graphene layers by atmospheric pressure graphitization of silicon carbide. *Nature Materials*, 8(3):203–207, 2009.

[73] A. Mattausch and O. Pankratov. Ab initio study of graphene on SiC. *Physical Review Letters*, 99(7):4, 2007.

[74] L. I. Johansson, F. Owman, P. Martensson, C. Persson and U. Lindefelt. Electronic structure of 6H-SiC(0001). *Physical Review B*, 53(20):13803–13807, 1996.

[75] D. Marchetto, C. Held, F. Hausen, F. Wählisch, M. Dienwiebel and R. Bennewitz. Friction and Wear on Single-Layer Epitaxial Graphene in Multi-Asperity Contacts. *Tribology Letters*, 48(1):77–82, 2012.

[76] D. Marchetto, T. Feser and M. Dienwiebel. Microscale study of frictional properties of graphene in ultra high vacuum. *Friction*, 3(2):161–169, 2015.

[77] T. Filleter, K. V. Emtsev, T. Seyller and R. Bennewitz. Local work function measurements of epitaxial graphene. *Applied Physics Letters*, 93(13):3, 2008.

[78] T. Filleter, J. L. McChesney, A. Bostwick, E. Rotenberg, K. V. Emtsev, T. Seyller, K. Horn and R. Bennewitz. Friction and Dissipation in Epitaxial Graphene Films. *Physical Review Letters*, 102(8):086102, 2009.

[79] T. Filleter and R. Bennewitz. Structural and frictional properties of graphene films on SiC(0001) studied by atomic force microscopy. *Physical Review B*, 81(15):155412, 2010.

[80] M. R. Vazirisereshk, H. Ye, Z. J. Ye, A. Otero-de-la-Roza, M. Q. Zhao, Z. L. Gao, A. T. C. Johnson, E. R. Johnson, R. W. Carpick and A. Martini. Origin of Nanoscale Friction Contrast between Supported Graphene, MoS_2, and a Graphene/MoS_2 Heterostructure. *Nano Letters*, 19(8):5496–5505, 2019.

[81] C. R. Woods, F. Withers, M. J. Zhu, Y. Cao, G. Yu, A. Kozikov, M. Ben Shalom, S. V. Morozov, M. M. van Wijk, A. Fasolino, M. I. Katsnelson, K. Watanabe, T. Taniguchi, A. K. Geim, A. Mishchenko and K. S. Novoselov. Macroscopic self-reorientation of interacting two-dimensional crystals. *Nature Communications*, 7(1):10800, 2016.

[82] S. Zhang, Q. Z. Yao, L. X. Chen, C. X. Jiang, T. B. Ma, H. M. Wang, X. Q. Feng and Q. Y. Li. Dual-Scale Stick-Slip Friction on Graphene/h-BN Moiré Superlattice Structure. *Physical Review Letters*, 128(22), 2022.

[83] H. Li, J. Wang, S. Gao, Q. Chen, L. Peng, K. Liu and X. Wei. Superlubricity between MoS_2 Monolayers. *Advanced Materials*, 29(27):1701474, 2017.

[84] H. Büch, A. Rossi, S. Forti, D. Convertino, V. Tozzini and C. Coletti. Superlubricity of epitaxial monolayer WS_2 on graphene. *Nano Research*, 11(11):5946–5956, 2018.

[85] M. Liao, Z.-W. Wu, L. Du, T. Zhang, Z. Wei, J. Zhu, H. Yu, J. Tang, L. Gu, Y. Xing, R. Yang, D. Shi, Y. Yao and G. Zhang. Twist angle-dependent conductivities across MoS_2/graphene heterojunctions. *Nature Communications*, 9(1):4068, 2018.

[86] M. Z. Liao, P. Nicolini, L. J. Du, J. H. Yuan, S. P. Wang, H. Yu, J. Tang, P. Cheng, K. Watanabe, T. Taniguchi, L. Gu, V. E. P. Claerbout, A. Silva, D. Kramer, T. Polcar, R. Yang, D. X. Shi and G. Y. Zhang. UItra-low friction and edge-pinning effect in large-lattice-mismatch van der Waals heterostructures. *Nature Materials*, page 8, 2022.

[87] Y. Gao, T. F. Cao, F. Cellini, C. Berger, W. A. de Heer, E. Tosatti, E. Riedo and A. Bongiorno. Ultrahard carbon film from epitaxial two-layer graphene. *Nature Nanotechnology*, 13(2):133–138, 2018.

[88] F. Cellini, F. Lavini, T. F. Cao, W. de Heer, C. Berger, A. Bongiorno and E. Riedo. Epitaxial two-layer graphene under pressure: Diamene stiffer than Diamond. *FlatChem*, 10:8–13, 2018.

[89] T. Hofmann, X. Ren, A. J. Weymouth, D. Meuer, A. Liebig, A. Donarini and F. J. Giessibl. Evidence for temporary and local transition of sp^2 graphite-type to sp^3 diamond-type bonding induced by the tip of an atomic force microscope. *New Journal of Physics*, 24(8):083018, 2022.

[90] F. Cellini, F. Lavini, E. Chen, A. Bongiorno, F. Popovic, R. L. Hartman, R. Dingreville and E. Riedo. Pressure-Induced Formation and Mechanical Properties of 2D Diamond Boron Nitride. *Advanced Science*, 8(2):2002541, 2021.

[91] A. P. M. Barboza, A. C. R. Souza, M. J. S. Matos, J. C. Brant, T. C. Barbosa, H. Chacham, M. S. C. Mazzoni and B. R. A. Neves. Graphene/h-BN heterostructures under pressure: From van der Waals to covalent. *Carbon*, 155:108–113, 2019.

[92] M. H. Oliveira, Jr., T. Schumann, M. Ramsteiner, J. M. J. Lopes and H. Riechert. Influence of the silicon carbide surface morphology on the epitaxial graphene formation. *Applied Physics Letters*, 99(11):111901, 2011.

[93] A. George, C. Neumann, D. Kaiser, R. Mupparapu, T. Lehnert, U. Hubner, Z. Tang, A. Winter, U. Kaiser, I. Staude and A. Turchanin. Controlled growth of transition metal dichalcogenide monolayers using Knudsen-type effusion cells for the precursors. *Journal of Physics-Materials*, 2(1), 2019.

[94] S. Shree, A. George, T. Lehnert, C. Neumann, M. Benelajla, C. Robert, X. Marie, K. Watanabe, T. Taniguchi, U. Kaiser, B. Urbaszek and A. Turchanin. High optical quality of MoS_2 monolayers grown by chemical vapor deposition. *2D Materials*, 7(1):015011, 2020.

[95] S. Roddaro, P. Pingue, V. Piazza, V. Pellegrini and F. Beltram. The optical visibility of graphene: Interference colors of ultrathin graphite on SiO2. *Nano Letters*, 7(9):2707–2710, 2007.

[96] K. W. Kolasinski. *Surface science: foundations of catalysis and nanoscience*. Wiley, Chichester, Weinheim [u.a.], 2002.

[97] Multiprobe® Surface Science systems User's Guide. *Project 081102 July 10, 2008, Omicron nanotechnology*, (126):236–244, 1983.

[98] G. Binnig, H. Rohrer, C. Gerber and E. Weibel. Surface Studies by Scanning Tunneling Microscopy. *Physical Review Letters*, 49(1):57–61, 1982.

[99] G. Binnig and H. Rohrer. Scanning tunneling microscopy. *Surface science*, 126(1-3):236–244, 1983.

[100] G. Binnig and H. Rohrer. Scanning tunneling microscopy. *Surface Science*, 152-153:17–26, 1985.

[101] The Nobel Prize in Physics 1986. *Nobelprize.org. Nobel Prize Outreach AB 2023*, (https://www.nobelprize.org/prizes/physics/1986/summary/), [access on: 12 Jun 2023].

[102] R. J. Cannara, M. J. Brukman and R. W. Carpick. Cantilever tilt compensation for variable-load atomic force microscopy. *Review of Scientific Instruments*, 76(5), 2005.

[103] E. Meyer, H. J. Hug and R. Bennewitz. *Scanning probe microscopy: the lab on a tip*. Springer Science & Business Media, 2004.

[104] M. L. B. Palacio and B. Bhushan. Normal and Lateral Force Calibration Techniques for AFM Cantilevers. *Critical Reviews in Solid State and Materials Sciences*, 35(2):73–104, 2010.

[105] M. Elstner, D. Porezag, G. Jungnickel, J. Elsner, M. Haugk, T. Frauenheim, S. Suhai and G. Seifert. Self-consistent-charge density-functional tight-binding method for simulations of complex materials properties. *Physical Review B*, 58(11):7260–7268, 1998.

[106] Atomistica Software Suite. (http://www.atomistica.org).

[107] L. Pastewka, S. Moser and M. Moseler. Atomistic Insights into the Running-in, Lubrication, and Failure of Hydrogenated Diamond-Like Carbon Coatings. *Tribology Letters*, 39(1):49–61, 2010.

[108] Frenkel D., Smit B. *Understanding Molecular Simulation 2nd edition*. Academic Press, 2002.

[109] I. Forbeaux, J. M. Themlin and J. M. Debever. Heteroepitaxial graphite on 6H-SiC(0001): Interface formation through conduction-band electronic structure. *Physical Review B*, 58(24):16396–16406, 1998.

[110] A. J. Van Bommel, J. E. Crombeen and A. Van Tooren. LEED and Auger electron observations of the SiC(0001) surface. *Surface Science*, 48(2):463–472, 1975.

[111] B. Luan and M. O. Robbins. The breakdown of continuum models for mechanical contacts. *Nature*, 435(7044):929–932, 2005.

[112] G. Brambilla and D. N. Payne. The Ultimate Strength of Glass Silica Nanowires. *Nano Letters*, 9(2):831–835, 2009.

[113] C. R. Kurkjian, P. K. Gupta and R. K. Brow. The Strength of Silicate Glasses: What Do We Know, What Do We Need to Know? *International Journal of Applied Glass Science*, 1(1):27–37, 2010.

[114] Q. Li, Y. Dong, D. Perez, A. Martini and R. W. Carpick. Speed Dependence of Atomic Stick-Slip Friction in Optimally Matched Experiments and Molecular Dynamics Simulations. *Physical Review Letters*, 106(12):126101, 2011.

[115] D. R. Tadjiev and R. J. Hand. Surface hydration and nanoindentation of silicate glasses. *Journal of Non-Crystalline Solids*, 356(2):102–108, 2010.

[116] T. Kuwahara, G. Moras and M. Moseler. Friction Regimes of Water-Lubricated Diamond (111): Role of Interfacial Ether Groups and Tribo-Induced Aromatic Surface Reconstructions. *Physical Review Letters*, 119(9):6, 2017.

[117] Y. Huang, Q. Yao, Y. Qi, Y. Cheng, H. Wang, Q. Li and Y. Meng. Wear evolution of monolayer graphene at the macroscale. *Carbon*, 115:600–607, 2017.

[118] X. L. Liu, I. Balla, H. Bergeron, G. P. Campbell, M. J. Bedzyk and M. C. Hersam. Rotationally Commensurate Growth of MoS_2 on Epitaxial Graphene. *ACS Nano*, 10(1):1067–1075, 2016.

[119] Y. Kobayashi, T. Taniguchi, K. Watanabe, Y. Maniwa and Y. Miyata. Slidable atomic layers in van der Waals heterostructures. *Applied Physics Express*, 10(4):045201, 2017.

[120] J. Gao, W. D. Luedtke, D. Gourdon, M. Ruths, J. N. Israelachvili and U. Landman. Frictional Forces and Amontons' Law: From the Molecular to the Macroscopic Scale. *The Journal of Physical Chemistry B*, 108(11):3410–3425, 2004.

[121] B. V. Derjaguin, V. M. Muller and Y. P. Toporov. Effect of contact deformations on the adhesion of particles. *Journal of Colloid and Interface Science*, 53(2):314–326, 1975.

[122] S. Y. Lee, U. J. Kim, J. Chung, H. Nam, H. Y. Jeong, G. H. Han, H. Kim, H. M. Oh, H. Lee, H. Kim, Y.-G. Roh, J. Kim, S. W. Hwang, Y. Park and Y. H. Lee. Large Work Function Modulation of Monolayer MoS_2 by Ambient Gases. *ACS Nano*, 10(6):6100–6107, 2016.

[123] F. J. Giessibl. Forces and frequency shifts in atomic-resolution dynamic-force microscopy. *Physical Review B*, 56(24):16010–16015, 1997.

[124] D. L. C. Ky, B.-C. Tran Khac, C. T. Le, Y. S. Kim and K.-H. Chung. Friction characteristics of mechanically exfoliated and CVD-grown single-layer MoS_2. *Friction*, 6(4):395–406, 2018.

[125] M.-Q. Le. Cohesive energy in graphene/MoS_2 heterostructures. *Meccanica*, 52(1):307–315, 2017.

[126] Z. Fang, X. Li, W. Shi, Z. Li, Y. Guo, Q. Chen, L. Peng and X. Wei. Interlayer Binding Energy of Hexagonal MoS_2 as Determined by an In Situ Peeling-to-Fracture Method. *The Journal of Physical Chemistry C*, 124(42):23419–23425, 2020.

[127] L. Fang, D.-M. Liu, Y. Guo, Z.-M. Liao, J.-B. Luo and S.-Z. Wen. Thickness dependent friction on few-layer MoS_2, WS_2, and WSe_2. *Nanotechnology*, 28(24):245703, 2017.

[128] S. Forti, A. Rossi, H. Büch, T. Cavallucci, F. Bisio, A. Sala, T. O. Menteş, A. Locatelli, M. Magnozzi, M. Canepa, K. Müller, S. Link, U. Starke, V. Tozzini and C. Coletti. Electronic properties of single-layer tungsten disulfide on epitaxial graphene on silicon carbide. *Nanoscale*, 9(42):16412–16419, 2017.

[129] O. Ochedowski, K. Marinov, N. Scheuschner, A. Poloczek, B. K. Bussmann, J. Maultzsch and M. Schleberger. Effect of contaminations and surface preparation on the work function of single layer MoS_2. *Beilstein Journal of Nanotechnology*, 5:291–297, 2014.

[130] M. Liao, L. Du, T. Zhang, L. Gu, Y. Yao, R. Yang, D. Shi and G. Zhang. Pressure-mediated contact quality improvement between monolayer MoS_2 and graphite. *Chinese Physics B*, 28(1):017301, 2019.

[131] X. Dong, C. Yan, D. Tomer, C. H. Li and L. Li. Spiral growth of few-layer MoS_2 by chemical vapor deposition. *Applied Physics Letters*, 109(5):051604, 2016.

[132] X. Liu, I. Balla, H. Bergeron and M. C. Hersam. Point Defects and Grain Boundaries in Rotationally Commensurate MoS_2 on Epitaxial Graphene. *The Journal of Physical Chemistry C*, 120(37):20798–20805, 2016.

[133] Z. Liu, A. Hinaut, S. Peeters, S. Scherb, E. Meyer, M. C. Righi and T. Glatzel. 2D KBr/Graphene Heterostructures – Influence on Work Function and Friction. *Nanomaterials*, 12(6), 2022.

[134] V. L. Solozhenko, G. Will and F. Elf. Isothermal compression of hexagonal graphite-like boron nitride up to 12 GPa. *Solid State Communications*, 96(1):1–3, 1995.

[135] J. Kang, S. Tongay, J. Zhou, J. Li and J. Wu. Band offsets and heterostructures of two-dimensional semiconductors. *Applied Physics Letters*, 102(1):012111, 2013.

[136] K. Huang, H. S. Qin, S. Zhang, Q. Y. Li, W. G. Ouyang and Y. L. Liu. The Origin of Moiré-Level Stick-Slip Behavior on Graphene/h-BN Heterostructures. *Advanced Functional Materials*, 32(35), 2022.

[137] P. Zeller and S. Günther. What are the possible moiré patterns of graphene on hexagonally packed surfaces? Universal solution for hexagonal coincidence lattices, derived by a geometric construction. *New Journal of Physics*, 16(8):083028, 2014.

[138] M. R. Vazirisereshk, K. Hasz, M.-Q. Zhao, A. T. C. Johnson, R. W. Carpick and A. Martini. Nanoscale Friction Behavior of Transition-Metal Dichalcogenides: Role of the Chalcogenide. *ACS Nano*, 14(11):16013–16021, 2020.

[139] Q. Peter, L. G. De Pietro and D. A. Zanin. MATLAB Library for Nanonis based files: NanoLib. (version 1.0):2017, January https://doi.org/10.5281/zenodo.263841, [access on: 12 Jun 2023].

[140] J. VandeVondele, M. Krack, F. Mohamed, M. Parrinello, T. Chassaing and J. Hutter. Quickstep: Fast and accurate density functional calculations using a mixed Gaussian and plane waves approach. *Computer Physics Communications*, 167(2):103–128, 2005.

[141] T. D. Kühne, M. Iannuzzi, M. Del Ben, V. V. Rybkin, P. Seewald, F. Stein, T. Laino, R. Z. Khaliullin, O. Schütt, F. Schiffmann, D. Golze, J. Wilhelm, S. Chulkov, M. H. Bani-Hashemian, V. Weber, U. Borštnik, M. Taillefumier, A. S. Jakobovits, A. Lazzaro, H. Pabst, T. Müller, R. Schade, M. Guidon, S. Andermatt, N. Holmberg, G. K. Schenter, A. Hehn, A.

Bussy, F. Belleflamme, G. Tabacchi, A. Glüß, M. Lass, I. Bethune, C. J. Mundy, C. Plessl, M. Watkins, J. VandeVondele, M. Krack and J. Hutter. CP2K: An electronic structure and molecular dynamics software package - Quickstep: Efficient and accurate electronic structure calculations. *The Journal of Chemical Physics*, 152(19), 2020.

[142] B. G. Lippert, J. H. Parrinello and Michele. A hybrid Gaussian and plane wave density functional scheme. *Molecular Physics*, 92(3):477–488, 1997.

[143] J. P. Perdew, K. Burke and M. Ernzerhof. Generalized Gradient Approximation Made Simple. *Physical Review Letters*, 77(18):3865–3868, 1996.

[144] J. VandeVondele and J. Hutter. Gaussian basis sets for accurate calculations on molecular systems in gas and condensed phases. *The Journal of Chemical Physics*, 127(11), 2007.

[145] S. Goedecker, M. Teter and J. Hutter. Separable dual-space Gaussian pseudopotentials. *Physical Review B*, 54(3):1703–1710, 1996.

Publications

In the context of this work at the INM - Leibniz Institute for New Materials, Saarbrücken, Germany the following contributions were published:

Peer reviewed articles

- Z. Liu, **B. Szczefanowicz**, J. M. J. Lopes, Z. Gan, A. George, A. Turchanin and R. Bennewitz, Nanoscale friction on MoS_2/graphene heterostructures, *Nanoscale*, 15, 2023, 5809–5815, DOI: 10.1039/d3nr00138e

- **B. Szczefanowicz**, T. Kuwahara, T. Filleter, A. Klemenz , L. Mayrhofer, R. Bennewitz and M. Moseler, Formation of intermittent covalent bonds at high contact pressure limits superlow friction on epitaxial graphene, *Physical Review Research*, 5, 2023, L012049, DOI: 10.1103/PhysRevResearch.5.L012049

Talks

- Intermittent covalent bonds and kinetic nanoscale friction on graphene/SiC under increasing contact pressure, **B. Szczefanowicz**, L. Mayrhofer, A. Klemenz, M. Moseler and R. Bennewitz, *NanoTech Poland 2021, June 9–11, 2021, virtual meeting*.

- Inception of covalent bonds and nanoscale kinetic friction on graphene/SiC under increasing contact pressure, **B. Szczefanowicz**, L. Mayrhofer, A. Klemenz, M. Moseler, R. Bennewitz, *7^{th} World Tribology Congress, July 10–15, 2022, Lyon*.

- Kinetic nanoscale friction on van der Waals heterostructures of MoS_2 and epitaxial graphene on SiC(0001), **B. Szczefanowicz**, Z. Liu, L. Mayrhofer, T. Kuwahara, A. Klemenz, M. Moseler, J. M. J. Lopes, A. George, Z. Gan, A. Turchanin and R. Bennewitz, *35^{th} European Conference on Surface Science, August 29–September 2, 2022, Luxembourg*.

- Kinetic nanoscale friction on van der Waals heterostructures, **B. Szczefanowicz**, Z. Liu, J. M. J. Lopes, A. George, Z. Gan, A. Turchanin, A. Rothstein, C. Stampfer and R. Bennewitz, *DPG Spring Meeting of the Condensed Matter Section, March 26–31, 2023, Dresden*.

- Nanomechanics of MoS_2/graphene van der Waals heterostructures on SiC(0001), **B. Szczefanowicz**, Z. Liu, J. M. J. Lopes, Z. Gan, A. George, A. Turchanin and R. Bennewitz, *The 8^{th} European Nanomanipulation Workshop, May 15–17, 2023, Kraków*.

- Kinetic nanoscale friction on van der Waals heterostructures, **B. Szczefanowicz**, Z. Liu, J. M. J. Lopes, A. George, Z. Gan, A. Turchanin, A. Rothstein, C. Stampfer and R. Bennewitz, *36^{th} European Conference on Surface Science, August 28–September 1, 2023, Łódź*.

Posters

- Kinetic nanoscale friction and intermittent hybridization in graphene stacks on SiC, **B. Szczefanowicz**, L. Mayrhofer, A. Klemenz, M. Moseler and R. Bennewitz, *DPG Spring Meeting of the Surface Science Division, March 1–4, 2021, virtual meeting*.

- Intermittent covalent bonds and kinetic nanoscale friction on graphene/SiC under increasing contact pressure, **B. Szczefanowicz** and R. Bennewitz, *SPP 2244 Summer School 2021: "vdW assembly – more than playing Lego", June 30–July 02, 2021, virtual meeting*.
- Structure and nanomechanics of MoS_2/graphene/SiC van der Waals heterostructures, **B. Szczefanowicz**, Z. Liu, J. M. J. Lopes, A. George and R. Bennewitz, *SPP 2244 Mid-term report colloquium, March 21–23, 2022, Dresden*.
- Kinetic nanoscale friction and intermittent hybridization in graphene stacks on SiC, **B. Szczefanowicz**, L. Mayrhofer, A. Klemenz, M. Moseler and R. Bennewitz, *PhD Day 2022, April 6, 2022, Saarbrücken*.
- Compressive strain in stacked 2D materials: from proximity to metastable hybridization, **B. Szczefanowicz**, Z. Liu, J. M. J. Lopes, A. George, Z. Gan, A. Turchanin, A. Rothstein, C. Stampfer and R. Bennewitz, *SPP 2244 Final workshop of first funding period, March 15–18, 2023, Bad Honeff* .
- Compressive strain in stacked 2D materials: from proximity to metastable hybridization, **B. Szczefanowicz**, Z. Liu, J. M. J. Lopes, A. George, Z. Gan, A. Turchanin, A. Rothstein, C. Stampfer and R. Bennewitz, *PhD Students' Day 2023, May 10, 2023, Saarbrücken*.

Acknowledgments

First and foremost, I would like to give my thanks to my supervisor Prof. Dr. Roland Bennewitz for allowing me to do my PhD studies in his group. I am very grateful for his supervision and a great amount of things I learned from him about conducting research in all its stages, from experiments in UHV to the proper way to write scientific works, including this one. Under Prof. Roland Bennewitz's supervision, I was able to work on various interesting projects, collaborate with different scientific groups across the globe and travel to various places for either student exchanges or to present my scientific work at international conferences. Thanks to Prof. Roland Bennewitz I became the scientist I always dreamed to be.

I thank my collaborators from various research groups. I am grateful to Prof. Moseler, Dr. Takuya Kuwahara, Dr. Leonhard Mayrhofer and Dr. Andreas Klemenz for their simulations and our discussions regarding our joint project. I would like to thank Dr. Joao Marcelo J. Lopes, Dr. Antony George, Ziyang Gan and Univ.-Prof. Dr. Andrey Turchanin for fruitful work and preparation of samples, without which one of my projects could not even start. I would like to sincerely thank Prof. Tobin Filleter, Peter Serles and the rest of their group for their hospitality, support at work and friendly atmosphere during my visit to Toronto. I thank Prof. Christof Stampfer, Alexander Rothstein and other members of their group in Aachen for their hospitality and the possibility of being at least a little involved in the art of stacking the 2D materials.

I am grateful to the entire INM - Leibniz Institute for New Materials for providing research facilities as well as a supportive and friendly environment, without which such a young researcher like me would not have performed as well as I did during these years. I would like to sincerely thank Dr. Christiane Petzold for teaching me how to prepare experiments in UHV-AFM. Special thanks to Birgit Nothdurft and Dominik Perius for their immense help with work on FIB and the preparation of my navigational microstructures. I thank Dr. Marcus Koch and Aude Haettich for SEM and TEM imaging of my cantilevers. I would also like to thank Sabine Müller, Miriam Badziong and Gabriele Koster for their administrative work, which allowed me to fully focus on my work either in the institute or during my business trips.

I am grateful to the present and the past colleagues from our Nanotribology/Interactive Surfaces group for numerous help as well as a friendly and supportive atmosphere. Special thanks to Dr. Johanna Blass and Dr. Günther Krämer for helping me in setting up in Saarbrücken and in the INM. I am grateful to Dr. Zhao Liu for our joint work in the lab and for teaching me how to use non-contact mode in the AFM. I thank Dr. Inga Melnyk for all the help and support given to me during my work and during writing this dissertation.

I thank all colleagues from the INM with whom I spend time inside and outside the work for kindness and for creating a motivating environment. I am grateful for all our discussions during lunch or tea breaks with a very broad variety of topics and also our every shared cake, which made my work in the INM at least a little bit sweet.

I would like to acknowledge the financial support of Deutsche Forschungsgemeinschaft within the Priority Program SPP 2244 "2DMP".

Finally, I would like to give my heartfelt thanks to my beloved parents Danuta and Henryk Szczefanowicz, who supported me as much as they could, and to whom I dedicate this dissertation. I would also give my sincere thanks to the rest of my family and friends for their

support in this challenging time. Chciałbym z całego serca podziękować moim kochanym rodzicom Danucie i Henrykowi Szczefanowicz, którzy wspierali mnie jak tylko mogli i którym to dedykuję niniejszą rozprawę. Chciałbym również serdecznie podziękować reszcie mojej rodziny i przyjaciołom za ich wsparcie w tym pełnym wyzwań czasie.